Optical Manipulation of Helium Atoms with Application to Neutral Atom Lithography

A Thesis Presented

by

Michael Christoph Keller

to

The Graduate School

in Partial Fulfillment of the Requirements

for the Degree of

Master of Arts

in

Physics

Stony Brook University

August 2006

Stony Brook University

The Graduate School

Michael Christoph Keller

We, the Thesis committee for the above candidate for the Master of Arts degree, hereby recommend acceptance of the Thesis.

Distinguished Teaching Professor Harold J. Metcalf, Thesis Advisor

Department of Physics and Astronomy, Stony Brook University

Research Assistant Professor Ralf Averbeck

Department of Physics and Astronomy, Stony Brook University

Assistant Professor Adam Durst

Department of Physics and Astronomy, Stony Brook University

This Thesis is accepted by the Graduate School.

Dean of the Graduate School

Abstract of the Thesis

Optical Manipulation of Helium Atoms with Application to Neutral Atom Lithography

by

Michael Christoph Keller

Master of Arts

in

Physics

Stony Brook University

2006

Advances within the last decades in the field of atomic, molecular and optical physics made it possible to get a high control over atomic samples. In this thesis the collimation of a beam of metastable helium and its application in the field of neutral atom lithography are presented.

In order to get a high-flux, well-collimated atomic beam we take advantage of the specific strengths of different laser cooling techniques. The bichromatic force with its superiority in magnitude and capture range compared to the radiative force allows for the capturing of atoms from within a cone of 175 mrad and reducing their transverse velocity by a factor of 10 in an interaction region of only 5 cm in length. A second stage of optical molasses further compresses

the phase-space so that we end up with a very bright beam of metastable helium atoms.

Due to the high internal energy of metastable helium of almost 20 eV per atom it is well-suited for the use in the field of atomic nanofabrication. The metastable atoms locally damage a resist layer that covers a gold coated silicon wafer. In a subsequent etching process the underlying gold is removed from where the atoms hit the sample thereby creating structures with a resolution below 100 nm.

By improving the experimental setup in many different ways compared to the initial state, we largely improved the control over the exposure process, made multiple exposures without the need for opening the vacuum chamber possible and moved towards the implementation of an all-optical mask for patterning the atomic beam.

To my family

Contents

List of Figures

List of Tables

Acknowledgements

When I was told that the acknowledgements are the hardest part of a thesis to write I was laughing, but now that everything else is almost finished and I'm trying to find the words to express what I'm feeling, I realize that it is indeed not easy. The reason for that is simple: the last twelve months I spend here at Stony Brook were amazing and so were the people I met here and who made every second of that year so unbelievably special and will make it hard for me to leave.

First of all I want to say thanks to my family. My parents and my two sisters, Susanne und Christiane, gave me every possible support. Without their countless phone calls, e-mails, letters, postcards and packages being away from home would have been a lot harder. I also want to thank all my friends back in Germany and all over the world who kept in touch during the year. Seeing my family and my friends again makes me look forward to going back to Germany.

My advisor Hal is one of the greatest persons I've ever met. He combines the characteristics of an excellent teacher, a brilliant scientist and – most important of all – a friend in his personality. On the one hand he gave me every freedom in doing research and on the other hand he helped me with any

question or problem (if it was science related or not) whenever I asked him. I hope that I'll get the chance to work together with him again at some point.

I want to thank Claire and Jason for working together with me at the experiment and even more for making the time in the lab not feel like work at all. Almost everything concerning techniques that are useful in a lab I learned from Claire and although I know that she is going to kill me when she'll read this, I have to say here that she is the true *AMO princess* ☺. I am so grateful that I could spend so much time with Claire and Jason and without them the work presented here wouldn't have been possible.

The group I worked in was an incredible group of people. I want to thank everyone who was part of Hal's group, especially the *hard core*: Seung-Hyun, Andreas, Esther, Xiyue, Jason and Claire. We seized any opportunity for celebrating, we cried and cursed together (some aloud others more inwardly) when equipment broke, we learned and laughed together, encouraged each other and had a lot of fun together. Unfortunately this group is breaking apart, since most of us already left or are leaving soon. But maybe the right way to look at it is that the group is extending all around the world and what could be a better reason for a visit in South Korea, France, Germany, China or the United States than to meet friends?

When moving to another country you're always a little lost in the beginning. And although that changed much faster than I expected it, I'm very thankful that I had two people to share this feeling with. Andreas and Christian not only shared a house with me during the year but we shared a year

of our lives together. If there's one thing that is true about my time here in Stony Brook, it's this: I couldn't possibly imagine this past year without the two of you! The fact that we can talk for a remarkably long time by just using quotes from situations that occured during that year and that noone else understands it or considers it funny shows best how much fun we had and how intense this experience was.

I found more and better friends during that year here in Stony Brook than I'd ever thought before. If I'd try to mention everyone here by name I would probably forget half of them, so I don't even try. But I hope every single one of them knows how much I enjoyed the time with them, every party, every day at the beach, every game of Kings, every little talk or little smile. Without them, Stony Brook wouldn't have been as wonderful as it was and I want to thank everyone of them.

I am indebted to everyone in Würzburg as well as in Stony Brook who made this exchange possible. I also want to thank everyone in the physics Department who helped me during the year, especially Pete Davis, the guys from the machine shop and the electronics shop, Pat Peiliker and everyone else from the Main Office, Peter Stephens and Linda Dixon. They helped me with various things I otherwise would have had problems dealing with.

My work and my stay in Stony Brook were supported by the *German National Academic Foundation* (*Studienstiftung des Deutschen Volkes*), the State of Bavaria (*Bayerische Begabtenförderung*) and the *Research Foundation of the State University of New York*.

Chapter 1

Introduction

The field of atomic physics developed rapidly over the last decades. Starting with the first experiments in cooling and trapping neutral atoms with laser light [1] a previously unimaginable control over atoms was achieved. It lead to huge improvements in the field of high resolution laser spectroscopy, made the creation of Bose-Einstein condensates possible and had great influence on the field of quantum computing and quantum cryptography.

For many of these fields and applications it is necessary to have atomic sources with a high, well collimated output and to be able to control the velocities of the atoms. In most experiments monochromatic light fields are used to achieve these goals but the arising forces are limited in both their magnitude and the velocity range of the atoms they can be used for. Since the limits of these forces are given by atomic properties, they can't be evaded by changing experimental parameters. To overcome the limitations of monochromatic light fields forces on atoms by polychromatic light have been investigated. Be-

sides forces created by periodic adiabatic rapid passage (ARP) sequences that rely on frequency chirped light pulses [2], also the force arising from light fields containing two frequencies has been studied in our laboratory [3]. This bichromatic force that can be made much larger than the force of a monochromatic light field has been used to create an intense beam of metastable 2^3S_1 helium (He*) [4].

Due to the high internal energy of He* of almost 20 eV it is a excellent candidate for the field of neutral atom lithography (NAL) [5]. First experiments in our laboratory showed the potential of this technique [6], but it became clear that major changes in the experimental setup were necessary to get better control over the procedure and thereby be able to test new ways of creating more complicated structures than the ones that have been produced by other groups.

For a theoretical understanding of forces on atoms in light fields, chapter 2 discusses the basic concepts with a focus on the bichromatic force. In chapter 3 an overview of the vacuum system is given while chapter 4 describes the optical setup in detail. Given all the information about how the He* beam is collimated and can be characterized, chapter 5 starts with a general overview of the field of atomic nanofabrication and the subfield of NAL. It continues with details about the molecules we use as a resist in the lithography process and describes the experimental procedure afterwards. At the end of the chapter the idea of a standing wave light mask is presented and discussed in some detail. Chapter 6 presents the results obtained during last year and the

improvements of the experimental setup while chapter 7 wraps up the thesis briefly by discussing the main achievements and the near future goals.

Chapter 2

Atom Light Interaction

2.1 Radiative Force

In a monochromatic light field atoms are subject to three fundamental processes [7]: absorption, stimulated emission and spontaneous emission of quanta of light, the so-called photons. If the light field has a wave vector $\vec{k}$, then each photon carries momentum $\vec{p}$ and energy E according to

$$\vec{p} = \hbar\vec{k} \tag{2.1}$$

$$E = \hbar\omega = \frac{hc}{\lambda} = \hbar\left|\vec{k}\right| c \tag{2.2}$$

For the case that only one transition within the atom is nearly resonant with the light field, i.e. its energy $\hbar\omega_a$ is comparable to the photon energy, the contributions of the other energy levels are considerably small and can therefore be neglected. That leads to the picture of a two-level system with the ground state $|g\rangle$ and the excited state $|e\rangle$ (see figure 2.1(a)).

Let for now the monochromatic light come only from one direction, i.e. only

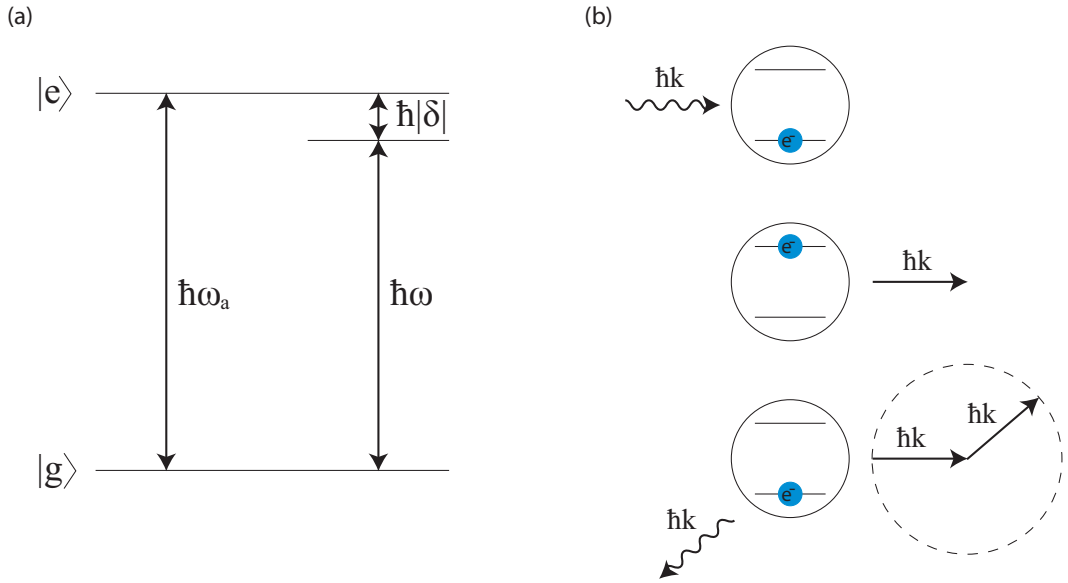

Figure 2.1
(a) Energy level diagram of the two-level atom. The laser is detuned from resonance between ground state $|g\rangle$ and excited state $|e\rangle$ by δ
(b) Momentum transfer by spontaneous emission. The direction of the emitted photon is random and therefore this momentum transfer averages out over many cycles which leads to a net momentum transfer in each absorption - spontaneous emission cycle.

one value for $\vec{k}$ exists. If an atom absorbs a photon the momentum of the atom is changed by the momentum carried by one photon, so $\Delta\vec{p}_{\text{atom}} = \hbar\vec{k}$, and the atom is left in its excited state. The deexcitation of the atom can happen in two different ways: if it happens via stimulated emission the emitted photon carries away the momentum $\hbar\vec{k}$, so the net momentum of an absorption - stimulated emission cycle is 0. If on the other hand the atom is deexcited by spontaneous emission the direction of the $\vec{k}$-vector is random and therefore the contribution of this process for the momentum change averages out over many cycles. The average net momentum transfer of an absorption - spontaneous

emission cycle hence is $\hbar\vec{k}$ (see figure 2.1(b)).

The force that can be exerted on an atom in this way is therefore directly connected to the scattering rate γ_p that is a measure for the rate at which spontaneous emission happens [1]

$$\gamma_p = \frac{s_0\gamma/2}{1 + s_0 + (2\delta/\gamma)^2} \tag{2.3}$$

In this equation $\delta = \omega - \omega_a$ is the detuning of the laser light with respect to the transition frequency, $\gamma = 1/\tau$ is the natural linewidth of the transition (the values for important He* transitions are tabulated in appendix A) and $s_0 = I/I_S$ is the saturation parameter which expresses the intensity of the light field in multiples of the saturation intensity I_S which is only dependent on properties of the atomic transition

$$I_S = \frac{\pi hc}{3\lambda^3\tau} \tag{2.4}$$

The dependence of the scattering rate on the detuning from resonance δ is shown for different saturation parameters in figure 2.2. Since with each spontaneous emission the momentum of the previously absorbed photon is transferred to the atom, the radiative force of the light field on the atom can be calculated to be

$$\vec{F}_{\text{rad}} = \dot{\vec{p}}_{\text{atom}} = \gamma_p\hbar\vec{k} = \frac{s_0\gamma/2}{1 + s_0 + (2\delta/\gamma)^2}\hbar\vec{k} \tag{2.5}$$

The force increases with higher intensities but saturates with a maximum force of

$$F_{\text{rad,max}} = \frac{\gamma}{2}\hbar\vec{k} \tag{2.6}$$

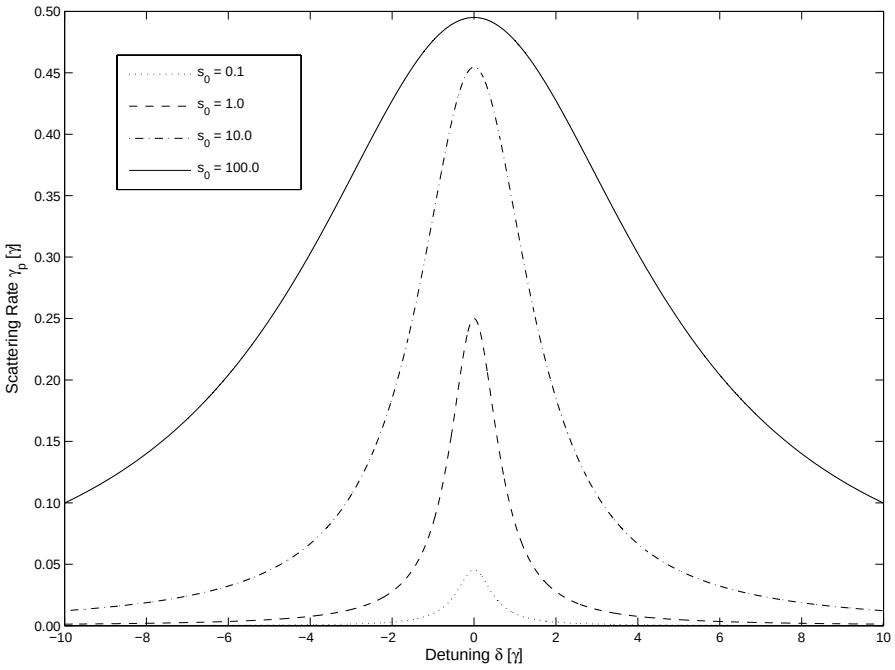

Figure 2.2 Dependence of the scattering rate on the detuning δ of the laser for different saturation parameters s_0.

The explanation for this is simple: in a two-level atom not more than half of the atoms can be transferred to the excited state via absorption since stimulated emission as a competing process has the same Einstein coefficient [7] as absorption. So 50% of the atoms at best are in the excited state and can undergo either spontaneous or stimulated emission. But since only spontaneous emission leads to a net momentum transfer the maximum rate at which that can happen is $\rho_{ee}\gamma_p = \gamma_p/2$ where ρ_{ee} is the population of the excited state.

2.1.1 Velocity Dependence

The radiative force as given in Eq. (2.5) is only valid for atoms at rest. For atoms with small finite velocities v, the frequency ω' as seen seen by the atoms is shifted from the actual frequency of the light ω by the Doppler effect [8] according to

$$\omega' \approx \omega - \vec{k} \cdot \vec{v} \tag{2.7}$$

If the frequency of the light as seen by the atom is below its transition frequency it is often referred to as *red* if it's above resonance it's called *blue*.

The formula for the radiative force (Eq. (2.5)) is then changed to

$$\vec{F}_{\text{rad}} = \frac{s_0 \gamma/2}{1 + s_0 + \left(2\left(\delta - \vec{k} \cdot \vec{v}\right)/\gamma\right)^2} \hbar \vec{k} \tag{2.8}$$

Since the frequency seen by the atom is velocity dependent and the radiative force influences atoms only within a very narrow frequency range (or if the intensity of the light is huge which power-broadens the profile of the scattering rate as can be seen in figure 2.2) only a small velocity group within the atoms can be addressed at the same time. Since velocity distributions of atoms coming from thermal sources are very broad compared to that, and it is often necessary to slow the atoms down from ~ 1000 $^{\text{m}}/_{\text{s}}$ to less than 100 $^{\text{m}}/_{\text{s}}$, it is necessary to either change the detuning of the light or the energy level structure of the atoms. The former has been done by rapidly chirping the frequency of the light [9] the latter one can be done by either taking magnetic fields using the Zeeman effect [10] or electric fields taking advantage of the Stark effect [11] to influence the transition frequency. Especially Zeeman slowers are nowadays

very often used for atomic beam deceleration, for example, to load a magneto-optical trap (MOT). Since the radiative force is comparably weak the length of those Zeeman slowers is often more than one meter.

2.2 Optical Molasses

To collimate an atomic beam in one dimension a red-detuned laser beam is used for sending light towards the atoms from opposite directions. That can either be done by splitting the beam with a 50/50 beamsplitter and sending the two beams in independently from opposite directions or by retroreflecting the beam coming from one side. In the latter case it is important to make sure that only a small fraction of the intensity gets scattered when passing the atomic sample for the first time so that the intensities of the counterpropagating beams are matched.

The resulting force for low light intensities can be derived by just adding up the radiative forces (see Eq. (2.8)) resulting from the two counterpropagating beams

$$\vec{F}_{OM} = \vec{F}_{+} + \vec{F}_{-} \tag{2.9}$$

with

$$\vec{F}_{\pm} = \pm\frac{\hbar\vec{k}\gamma}{2}\frac{s_0}{1 + s_0 + \left[2\left(\delta \mp \vec{k}\cdot\vec{v}\right)/\gamma\right]^2} \tag{2.10}$$

The velocity dependent force profile for some parameters is shown in figure 2.3. In the linear region around $v = 0$ the force can be linearly approxi-

mated

$$\vec{F}_{OM} \cong \frac{8\hbar k^2 \delta s_0 \vec{v}}{\gamma \left[1 + s_0 + (2\delta/\gamma)^2\right]^2} \equiv -\beta \vec{v} \tag{2.11}$$

with the damping coefficient β.

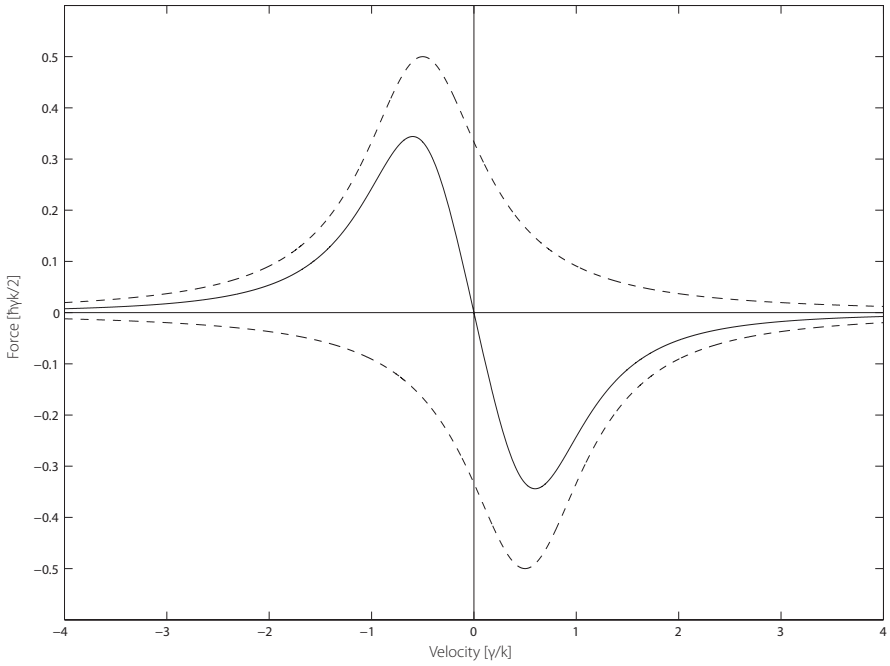

Figure 2.3 Force Profile for Optical Molasses. The parameters are chosen for a minimal final velocity (Doppler molasses): $\delta = -\frac{\gamma}{2}$, $s_0 = 1$. The dashed lines show the contributions of $F_\pm$ to the force profile.

Because of the factor of δ in the numerator of β, the laser has to be red detuned $\delta < 0$ to get $\frac{\partial F_{OM}}{\partial v} < 0$ around $v = 0$ and therefore be able to use the force of optical molasses for cooling an atomic sample. If counterpropagating red detuned beams are applied in all three dimensions, the movement of an atom is inhibited in any direction. The analogy of the resulting cool atomic

cloud with a viscous syrup leads to the name of *optical molasses*.

Two parameter dependent properties of optical molasses are of special interest for our experiment: the final velocity of the captured atoms and the capture range, i.e. the velocity range which can be caught by an optical molasses configuration. The force profile itself doesn't give any clue for a non-zero final velocity. From a classical point of view such a force should cool the atoms down to a final velocity of 0. However, since the cooling process happens with finite momentum kicks, the cooling process due to $\vec{F}_{OM}$ and the recoil from the momentum transfers act as two competing processes. The steady state solution gives an average kinetic energy of the atoms of

$$\bar{E}_{\text{kin}} = \frac{\hbar\gamma}{8}\left(\frac{2\,|\delta|}{\gamma} + \frac{\gamma}{2\,|\delta|}\right) \tag{2.12}$$

The steady state kinetic energy is dependent on the detuning δ and has a minimum for $\delta = -\frac{\gamma}{2}$. Choosing such a detuning and having $s_0 = 1$ is known as ordinary Doppler molasses and gives a final velocity of

$$v_D = \sqrt{\frac{\hbar\gamma}{2M}} \tag{2.13}$$

where M is the atomic mass. The Doppler velocity for the $2^3S_1 - 2^3P_2$ transition in He* is 28.44 $^{\text{cm}}/_{\text{s}}$ (see appendix A).

In the general case the final velocity can be derived from Eq. (2.12) to be

$$v_f = \sqrt{\frac{\hbar\gamma}{4M}\left(\frac{2\,|\delta|}{\gamma} + \frac{\gamma}{2\,|\delta|}\right)} \tag{2.14}$$

The capture velocity of an optical molasses configuration is defined as the velocity where the force has a maximum / minimum. For the configuration of

Doppler molasses ($\delta = -\frac{\gamma}{2}$, $s_0 = 1$), the capture velocity can be calculated to be approximately

$$v_{c,D} \approx \frac{\gamma}{k} \tag{2.15}$$

which is 1.76 $^{\mathrm{m}}/_{\mathrm{s}}$ for the $2^3S_1 - 2^3P_2$ transition.

The capture velocity can be increased by choosing bigger values for δ and / or s_0. Choosing a bigger detuning leads to bigger final velocities according to Eq. (2.14). Increasing s_0 largely on the other hand violates the approximation that was done to derive the force of optical molasses in Eqs. (2.9) & (2.10). The effects that can arise in the case of so-called high intensity optical molasses, for example a reversal of the force around $v = 0$ for certain intensities, has been studied by others [12, 13] and needs a different approach that is not discussed here.

2.3 Dipole Force

In the presence of a light field the energy levels within an atom are shifted due to the changes in the Hamiltonian. The energy shifts of the ground and the excited state in a two-level atom in the presence of a weak light field ($\Omega \ll |\delta|$) are given by [1]

$$\Delta E_g = \frac{\hbar\Omega^2}{4\delta} \tag{2.16a}$$

$$\Delta E_e = -\frac{\hbar\Omega^2}{4\delta} \tag{2.16b}$$

where $\Omega = \gamma\sqrt{\frac{I}{2I_S}}$ is the Rabi frequency, a measure for the field strength (cf. section 2.4.2).

In a spatially modulated light field, for example a standing wave, this intensity dependent light shift creates a spatially varying potential U and therefore a force on the atom $-\nabla U$, called the dipole force. Unlike the radiative force that is limited by the rate at which spontaneous emission occurs, the dipole force can be made arbitrarily large by increasing the intensity of the light field. A common application of the dipole force is the creation of an optical lattice. Optical lattices can be used to trap Bose-Einstein condensates (BECs) or as a mask to pattern atomic beams in ANF (see section 5.4).

It would be, of course, of great value to use the dipole force for laser cooling purposes because of its magnitude that can be adjusted without limits. But since the force is conservative and its effects average out over the distance of an optical wavelength, it cannot be used for phase-space compression (Liouville's theorem) and hence not for laser cooling.

2.4 Bichromatic Force

As we saw in sections 2.1 and 2.2 the dissipative force on atoms that is achievable with monochromatic light is limited in both magnitude and capture range. And although forces arising from monochromatic light were studied and implemented with great success over the last 30 years [14, 10] it wasn't until the late 1980s that people started examining forces on atoms in bichromatic light

fields, i.e. when light of two different frequencies is present [15, 16].

It is necessary to look at the quantum mechanical interaction between atoms and light in more detail to be able to give a qualitative description or to do quantitative calculations on the bichromatic force. A short description is given in the following sections, more details can be found for example in [1].

2.4.1 Schrödinger Equation

The time dependent Schrödinger equation for an atom in a radiation field is

$$\mathcal{H}\left|\Psi\left(\vec{r},t\right)\right\rangle = i\hbar\frac{\partial\left|\Psi\left(\vec{r},t\right)\right\rangle}{\partial t} \tag{2.17}$$

where $\mathcal{H}\left(t\right) = \mathcal{H}_0 + \mathcal{H}'\left(t\right)$ is the total Hamiltonian for the atom in a light field that consists of the time-independent Hamiltonian of the atom without any field $\mathcal{H}_0$ and the interaction part between the atom and the field $\mathcal{H}'\left(t\right)$. Since the eigenfunctions $\left|\phi_n\left(\vec{r}\right)\right\rangle$ of $\mathcal{H}_0$ form a complete set, the wave function can be expressed as

$$\left|\Psi\left(\vec{r},t\right)\right\rangle = \sum_k c_k\left(t\right)\left|\phi_k\left(\vec{r}\right)\right\rangle e^{-i\omega_k t} \tag{2.18}$$

where $E_n = \hbar\omega_n$ are the eigenvalues of $\mathcal{H}_0$ to $\left|\phi_n\left(\vec{r}\right)\right\rangle$. The Schrödinger equation can then be rewritten as

$$\begin{aligned}\mathcal{H}\left|\Psi\left(\vec{r},t\right)\right\rangle &= \left[\mathcal{H}_0 + \mathcal{H}'\left(t\right)\right]\sum_k c_k\left(t\right)\left|\phi_k\left(\vec{r}\right)\right\rangle e^{-i\omega_k t} \\ &= i\hbar\frac{\partial}{\partial t}\sum_k c_k\left(t\right)\left|\phi_k\left(\vec{r}\right)\right\rangle e^{-i\omega_k t}\end{aligned} \tag{2.19}$$

When multiplying that equation with $\left\langle\phi_j^*\left(\vec{r}\right)\right|$ which in Dirac's bra-ket notation also includes an integration over the spatial coordinate of the electron

$\vec{r}$ we obtain

$$i\hbar\frac{\mathrm{d}c_j\left(t\right)}{\mathrm{d}t}=\sum_k c_k\left(t\right)\mathcal{H}'_{jk}\left(t\right)e^{i\omega_{jk}t} \tag{2.20}$$

with $\mathcal{H}'_{jk}\left(t\right)\equiv\langle\phi_j|\mathcal{H}'\left(t\right)|\phi_k\rangle$ and $\omega_{jk}\equiv\left(\omega_j-\omega_k\right)$.

2.4.2 Rabi Oscillations

To derive Eq. (2.20) from the Schrödinger equation no approximation has been done so far. Unfortunately the equation is not solvable in the general case. However, since our light field is supposed to be almost resonant with only one atomic transition we can again make the assumption of a two-level atom thereby truncating the infinite sum from Eq. (2.20). Furthermore, if we absorb all diagonal elements of $\mathcal{H}'\left(t\right)$ into $\mathcal{H}_0$ the only one nonzero element of the interaction Hamiltonian, $\mathcal{H}'_{ge}\left(t\right)=\mathcal{H}'_{eg}{}^{*}\left(t\right)$ is left and Eq. (2.20) turns into

$$i\hbar\frac{\mathrm{d}c_g\left(t\right)}{\mathrm{d}t}=c_e\left(t\right)\mathcal{H}'_{ge}\left(t\right)e^{-i\omega_a t} \tag{2.21a}$$

and

$$i\hbar\frac{\mathrm{d}c_e\left(t\right)}{\mathrm{d}t}=c_g\left(t\right)\mathcal{H}'_{eg}\left(t\right)e^{i\omega_a t} \tag{2.21b}$$

where $\omega_{eg}=\omega_a$ is the transition frequency of the two-level-atom.

The interaction Hamiltonian can be derived for laser fields that are not too strong (i.e. non-linear effects can be neglected) in a consistent way by using the canonical momentum $\vec{p}_c=\vec{p}-\frac{e}{c}\vec{A}\left(\vec{r},t\right)$ instead of the regular momentum $\vec{p}$. This can be found in detail in the literature, for example in [17], and yields

the result

$$\mathcal{H}'(t) = -e\vec{\mathcal{E}}(\vec{r},t)\cdot\vec{r} \tag{2.22}$$

For a plane wave with frequency ω travelling in the positive z-direction we have the electric field operator

$$\vec{\mathcal{E}}(\vec{r},t) = E_0\hat{\varepsilon}\cos(kz-\omega t) \tag{2.23}$$

with the amplitude E_0 and the unit polarization vector $\hat{\varepsilon}$.

If we use the electric dipole approximation (we assume that the electric field is constant over the size of the atom, and take into account that the dipole moment $-e\vec{r}$ of the atom is parallel to the polarization of the field $\hat{\varepsilon}$) the coupling part of the Hamiltonian becomes $\mathcal{H}'_{eg}(t) = \hbar\Omega\cos(kz-\omega t)$ with the Rabi frequency

$$\Omega = -\frac{eE_0}{\hbar}\langle e|r|g\rangle \tag{2.24}$$

By using the rotating wave approximation (RWA), i.e. neglecting terms on the order of $1/\omega$ in comparison with terms on the order of $1/\delta$ (with the laser detuning from resonance $\delta = \omega - \omega_a$) we can separate Eqs. (2.21) and obtain

$$\frac{\mathrm{d}^2c_g(t)}{\mathrm{d}t^2} - i\delta\frac{\mathrm{d}c_g(t)}{\mathrm{d}t} + \frac{\Omega^2}{4}c_g(t) = 0 \tag{2.25a}$$

and

$$\frac{\mathrm{d}^2c_e(t)}{\mathrm{d}t^2} + i\delta\frac{\mathrm{d}c_e(t)}{\mathrm{d}t} + \frac{\Omega^2}{4}c_e(t) = 0 \tag{2.25b}$$

which can be solved for the initial conditions $c_g(0) = 1$ and $c_e(0) = 0$ to get

$$c_g(t) = \left(\cos\frac{\Omega' t}{2} - i\frac{\delta}{\Omega'}\sin\frac{\Omega' t}{2}\right)e^{i\delta t/2} \tag{2.26a}$$

and

$$c_e(t) = -i\frac{\Omega}{\Omega'}\sin\frac{\Omega' t}{2}e^{-i\delta t/2} \tag{2.26b}$$

where

$$\Omega' = \sqrt{\Omega^2 + \delta^2} \tag{2.26c}$$

The observable quantities are the populations of the ground and the excited state

$$|c_g(t)|^2 = 1 - \frac{1}{2}\left(\frac{\Omega}{\Omega'}\right)^2 [1 - \cos(\Omega' t)] \tag{2.27a}$$

$$|c_e(t)|^2 = \frac{1}{2}\left(\frac{\Omega}{\Omega'}\right)^2 [1 - \cos(\Omega' t)] \tag{2.27b}$$

It can easily be seen from those equations that the population oscillates between the ground state and the excited state. The more off-resonant the light is the faster are the oscillations but on the other hand the smaller is their amplitude. Plots of the population of the excited state over time $|c_e(t)|^2$ are shown in figure 2.4. Complete population transfer to the excited state is only possible if the light is resonant with the atomic transition. In this case the population can is completely inverted after a time $t = \frac{2\pi}{2\Omega'} = \frac{2\pi}{2\Omega}$. That means that pulses of that length bring the atoms from the ground state to the excited state or vice versa. Since that time corresponds to a phase of π in Eqs. (2.27) a light pulse of the right length and amplitude to invert the population is called a π-pulse.

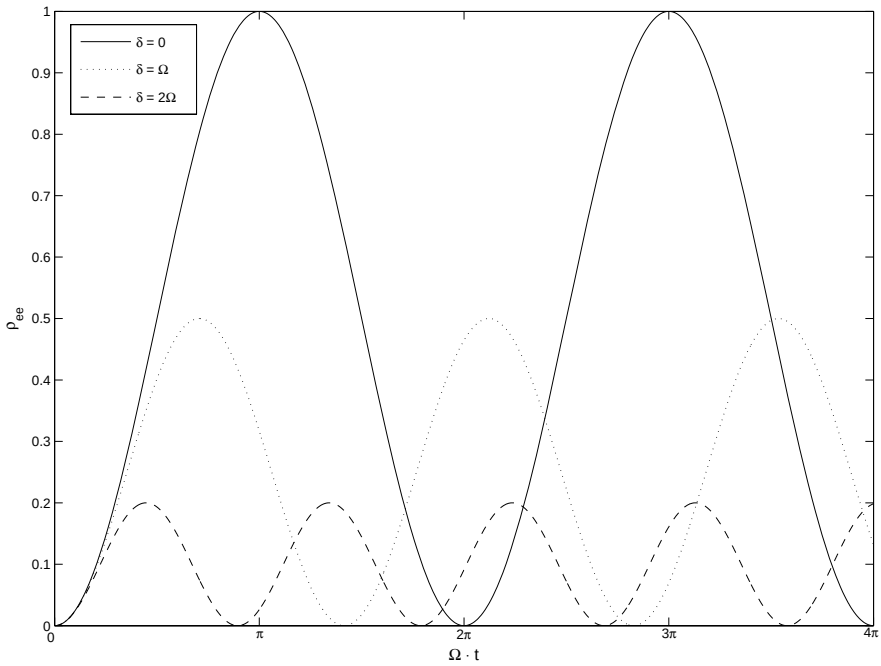

Figure 2.4 Rabi oscillations. Shown is the probability for the atom to be in the excited state for different laser detunings. The oscillation frequency increases with the detuning but the amplitude decreases.

2.4.3 Pi-Pulse Model

The bichromatic force arises from two counterpropagating beams that both contain two frequencies. If both frequency components have the same amplitude E_0 and are symmetrically detuned from the center frequency ω by $\pm\delta$ the electric field within the beam travelling in the positive z-direction is

$$\begin{aligned} E_+ &= E_0 \cos\left((\omega+\delta)\,t - kz\right) + E_0 \cos\left((\omega-\delta)\,t - kz\right) \\ &= 2E_0 \cos\left(\omega t - kz\right) \cos\left(\delta t\right) \end{aligned} \tag{2.28}$$

That shows that it can also be seen as a amplitude modulated light beam

with frequency ω. If now that frequency is brought to atomic resonance, i.e. $\omega = \omega_a$, and the intensity of the beams is adjusted such that each beat of length $\frac{\pi}{\delta}$ forms a π-pulse, the bichromatic light forms a train of π-pulses that efficiently excite or deexcite the atoms.

The π-pulse condition for the Rabi frequency $\Omega_+ = 2\Omega\cos(\delta t)$ is

$$\int_{-\pi/2\delta}^{\pi/2\delta} 2\Omega\cos(\delta t)\,\mathrm{d}t = \pi \tag{2.29a}$$

$$\rightarrow\ \Omega = \frac{\pi\delta}{4} \tag{2.29b}$$

To get an effective force it is necessary to have two counterpropagating beams. In the general case there will be a phase delay of ϕ between two pulses of the different beams (note: a relative phase of $\phi = \pi$ means that the pulses from the two beams are alternating, the relative phase between the two beat envelopes is always $\frac{\phi}{2}$) so we can write for the total electric field

$$\begin{aligned} E &= E_+ + E_- \\ &= 2E_0\left[\cos(\omega t - kz)\cos\left(\delta t - \frac{\phi}{4}\right) + \cos(\omega t + kz)\cos\left(\delta t + \frac{\phi}{4}\right)\right] \end{aligned} \tag{2.30}$$

If the first beam excites the atom it transfers $\hbar\vec{k}$ of momentum to the atom. The next π-pulse from the second beam causes stimulated emission of a photon and causes another change in momentum by $\hbar\vec{k}$ (in the same direction since beam is travelling in opposite direction, see figure 2.5(b)). Since the duration for such an excitation - deexcitation process depends on the length of one π-pulse and therefore is $\frac{\pi}{\delta}$, the first rough estimate of the magnitude of

the bichromatic force is given by

$$F_{\text{bichro}} = \frac{2\hbar k\delta}{\pi} \tag{2.31}$$

For the direction of the force it is important which pulse excites the atoms and which one causes stimulated emission. Therefore it has to be possible to adjust the relative phase between the two π-pulse trains (cf. figure 2.5(a)). It is not desirable to have the two pulses overlap but on the other hand it is important to take spontaneous emission into account. If spontaneous emission happens the next arriving pulse that was supposed to deexcite the atom is now exciting the atom, therefore changing the sign of the resulting force. In a symmetric situation with a phase delay of π the resulting force would average out to 0. It is therefore important to have the deexcitation process not to long after the excitation. Numerically it was determined that the maximum force arises with a relative phase of $\sim \frac{\pi}{2}$ (see section 2.4.5).

In that case the time the atom spends in the excited state is 1/4 of the total time as long as the correct pulse is exciting the atom. As soon as spontaneous emission happens the force changes sign but at the same time the atom now spends 3/4 of the time in the excited state which makes another spontaneous emission much more likely thereby self-correcting the direction of the resulting force. Since the force is going in the wrong direction for 1/4 of the time, the magnitude of the resulting force is only half as big as the first guess in Eq. (2.31)

$$F_{\text{bichro}} = \frac{\hbar k\delta}{\pi} \tag{2.32}$$

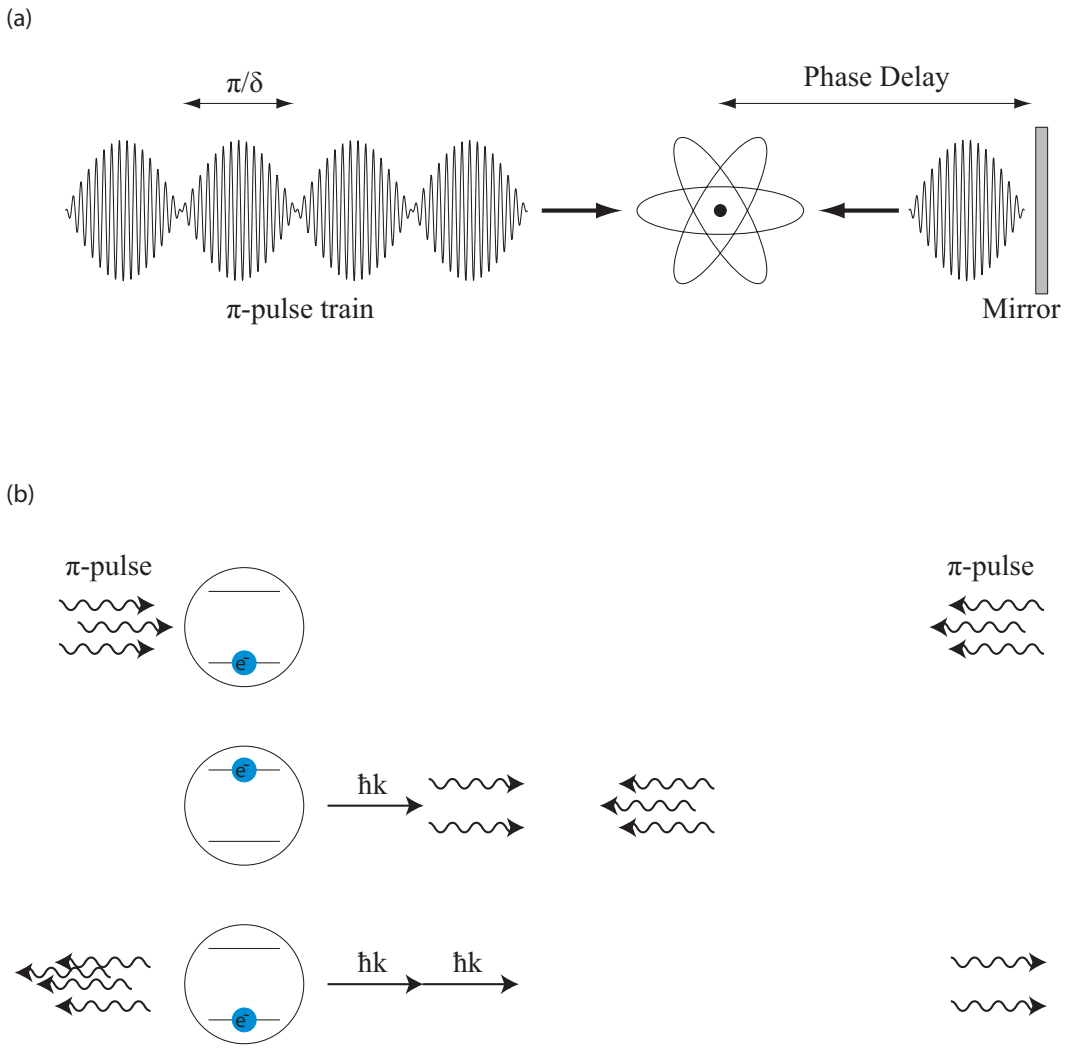

Figure 2.5
(a) To control the magnitude and the direction of the force it is necessary to have control over the relative phase between the two counterpropagating π-pulse trains.
(b) Schematic of the excitation - deexcitation process. Since the exciting pulse comes from a different beam than the deexciting one the net force doesn't vanish.

Although the π-pulse model is only able to show the functional principle of the bichromatic force qualitatively and doesn't give any velocity dependence of the force, it still gives an estimate of the magnitude of the arising force showing that it scales with the difference between the two frequency components in the beams. This can be chosen and therefore made much larger than the force of optical molasses $F_{OM} \approx \frac{\hbar k \gamma}{2}$ which is limited by the natural linewidth of the atomic transition in use.

2.4.4 Optical Bloch Equations

To get a more detailed description of the bichromatic force it is important to include spontaneous emission, an arbitrary intensity and relative phase between the two counterpropagating beams, and the velocity of the atoms in the description. This can be done using the density matrix for a pure state

$$\rho = \begin{pmatrix} \rho_{ee} & \rho_{eg} \\ \rho_{ge} & \rho_{gg} \end{pmatrix} = \begin{pmatrix} c_e c_e^* & c_e c_g^* \\ c_g c_e^* & c_g c_g^* \end{pmatrix} \tag{2.33}$$

with ρ_{gg} and ρ_{ee} being the populations of the ground state and the excited state respectively and ρ_{ge} and ρ_{eg} being the so-called coherences. For the time-evolution of the density matrix we can derive from Eq. (2.20)

$$i\hbar \frac{\mathrm{d}\rho}{\mathrm{d}t} = [\mathcal{H}, \rho] \tag{2.34}$$

By including spontaneous emission and without doing the RWA yet, we

get for the components of the density matrix [15]

$$\dot{\rho}_{gg} = \frac{i}{\hbar}\left(\rho_{eg} - \rho_{ge}\right) dE + \gamma\rho_{ee} \tag{2.35a}$$

$$\dot{\rho}_{ge} = \frac{i}{\hbar}\left(\rho_{ee} - \rho_{gg}\right) dE + \left(i\omega_a - \frac{\gamma}{2}\right)\rho_{ge} \tag{2.35b}$$

$$\rho_{ge} = \rho^*_{eg} \tag{2.35c}$$

$$\rho_{gg} + \rho_{ee} = 1 \tag{2.35d}$$

where $d = -e\left\langle e|r|g\right\rangle$ is the dipole matrix element of the atom, E is the electric field and γ is the inverse of the lifetime τ of the excited state.

Since the overall phase doesn't matter for the description, we have only three independent variables (both real and imaginary parts of $\rho_{ge} = \rho^*_{eg}$ and $\rho_{gg} = 1 - \rho_{ee}$) that can be expressed in terms of three real variables called the Bloch variables [18]

$$r_1 = \rho_{ge}e^{-i\omega t} + \rho_{eg}e^{i\omega t} \tag{2.36a}$$

$$r_2 = i\left(\rho_{ge}e^{-i\omega t} - \rho_{eg}e^{i\omega t}\right) \tag{2.36b}$$

$$r_3 = \rho_{gg} - \rho_{ee} \tag{2.36c}$$

Expressing the components of the density matrix using these variables we get

$$\rho_{gg} = \frac{1}{2}\left(1 + r_3\right) \tag{2.37a}$$

$$\rho_{ee} = \frac{1}{2}\left(1 - r_3\right) \tag{2.37b}$$

$$\rho_{ge} = \frac{1}{2}\left(r_1 - ir_2\right)e^{i\omega t} \tag{2.37c}$$

$$\rho_{eg} = \frac{1}{2}\left(r_1 + ir_2\right)e^{-i\omega t} \tag{2.37d}$$

Those definitions can now be used in Eqs. (2.35). Then the electric field for our bichromatic beam configuration from Eq. (2.30) can be plugged in and the RWA leads to a replacement of the rapidly varying terms by their time-average ($\sin(2\omega t) \to 0$, $\sin^2(\omega t) \to \frac{1}{2}$ and $\cos^2(\omega t) \to \frac{1}{2}$). If as a second approximation the constant velocity approximation is made which expresses the time-dependent position of an atom in terms of its velocity $z = vt$ we get

$$\dot{r}_1 = (\omega_a - \omega) r_2 - \frac{\gamma}{2} r_1 - 4\Omega r_3 \sin(kvt) \sin\left(\frac{\phi}{4}\right) \sin(\delta t) \tag{2.38a}$$

$$\dot{r}_2 = (\omega_a - \omega) r_1 - \frac{\gamma}{2} r_2 + 4\Omega r_3 \cos(kvt) \cos\left(\frac{\phi}{4}\right) \cos(\delta t) \tag{2.38b}$$

$$\begin{aligned}\dot{r}_3 =& 4\Omega \left[r_1 \sin(kvt) \sin\left(\frac{\phi}{4}\right) \sin(\delta t) - r_2 \cos(kvt) \cos\left(\frac{\phi}{4}\right) \cos(\delta t) \right] \\ &+ \gamma (1 - r_3)\end{aligned} \tag{2.38c}$$

The force on an atom in a light field $\vec{\mathcal{E}}(\vec{r}, t)$ in the electric dipole approximation is given by [1]

$$F = e \frac{\partial}{\partial z} \left(\left\langle \vec{\mathcal{E}}(\vec{r}, t) \cdot \vec{r} \right\rangle \right) \tag{2.39}$$

Using the electric field in the bichromatic configuration (Eq. (2.30)) and the definition for the Rabi frequency (Eq. (2.24)) we obtain

$$F = \frac{\hbar}{E_0} \frac{\partial E}{\partial z} (\Omega \rho_{ge} + \Omega^* \rho_{eg}) \tag{2.40}$$

By expressing the components of the density matrix in terms of the real Bloch variables (Eqs. (2.37)) and applying the RWA, we get a rather short expression for the force on an atom in a bichromatic field

$$F = 2\hbar k \Omega \left(-r_1 \cos(\delta t) \cos\left(\frac{\phi}{4}\right) \sin(kvt) + r_2 \sin(\delta t) \sin\left(\frac{\phi}{4}\right) \cos(kvt) \right) \tag{2.41}$$

2.4.5 Numerical Calculations

The optical Bloch equations (Eqs. (2.38)) can't be solved analytically. A numerical approach, however, yields force profiles that show the velocity dependence and the magnitude of the arising force. A Fortran program was developed by J. Söding et al. [19] that numerically solves the OBEs and after the Bloch variables reached a steady state the force is calculated in each time step according to Eq. (2.41) and averaged over time to get an effective value for the force. To use a more adaptive method for solving the ordinary differential equations (ODEs) numerically, I modified the program to use the code BiM [20] that offers a variable order - variable stepsize method for initial value problems for ODEs. The order of the method used for the calculation process varies from 4 to 12 and is adjusted automatically during the computation process. The code of the modified Fortran program is given in appendix B.

For the given parameters δ, Ω (both in multiples of γ) and ϕ, the program calculates the force on atoms with velocities between $v_{\min}$ and $v_{\max}$. Depending on the settings within the program, such a calculation for several hundred different velocities can take hours on a current PC. Figure 2.6 shows a simulation of the dependence of the force on the relative phase between the exciting and the deexciting pulse. As expected the force reverses sign when going from a phase of ϕ to a phase of $2\pi - \phi$.

When looking at some force profiles for different phase delays in more detail (see figure 2.7), it is obvious that a phase delay of $\phi = \frac{\pi}{2}$ gives the force profile with the desired properties: high magnitude and big capture range and

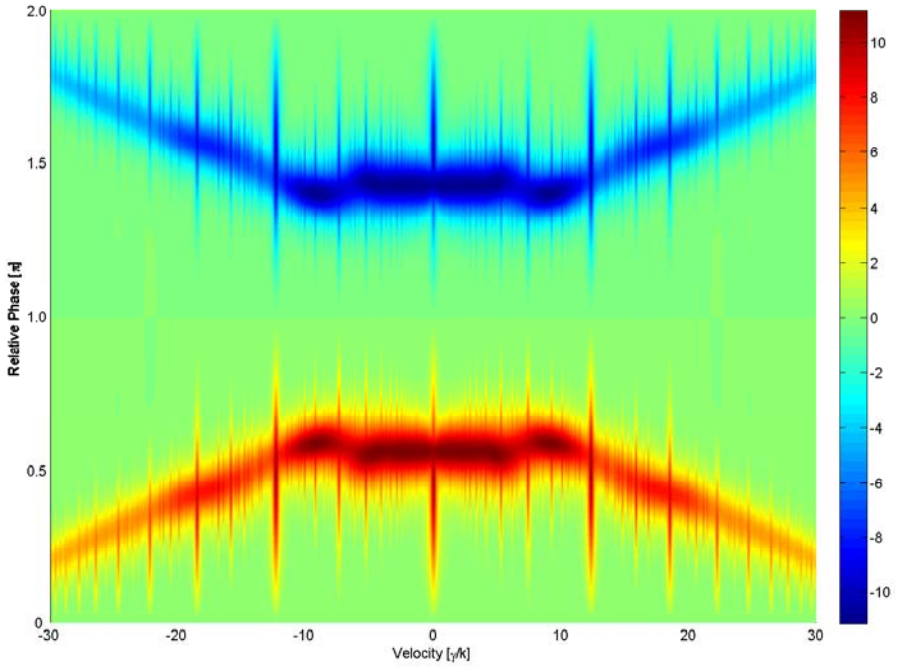

Figure 2.6 Dependence of the bichromatic force on the relative phase between the exciting and the deexciting pulse. The parameters for the detuning and the Rabi frequency are $\delta = 37\gamma$, $\Omega = 41\gamma$ as in the experiment. The magnitude of the force is shown by different colors in units of $\hbar k\gamma$.

a pretty much flat profile with steep edges. The spikes that can be seen in all the force profiles are partly numerical artifacts (although in the shown results they are mainly suppressed by using a high accuracy for solving the OBEs) and partly effects of multiphoton processes (Dopplerons) [12].

Another dependence to look at is the dependence of the force profile on the light intensity (Rabi frequency Ω). A contour plot of the results of such an analysis is shown in figure 2.8. In the region where the pi-pulse condition is fulfilled ($\Omega = 29\gamma$) the force starts to become big over a wide velocity range.

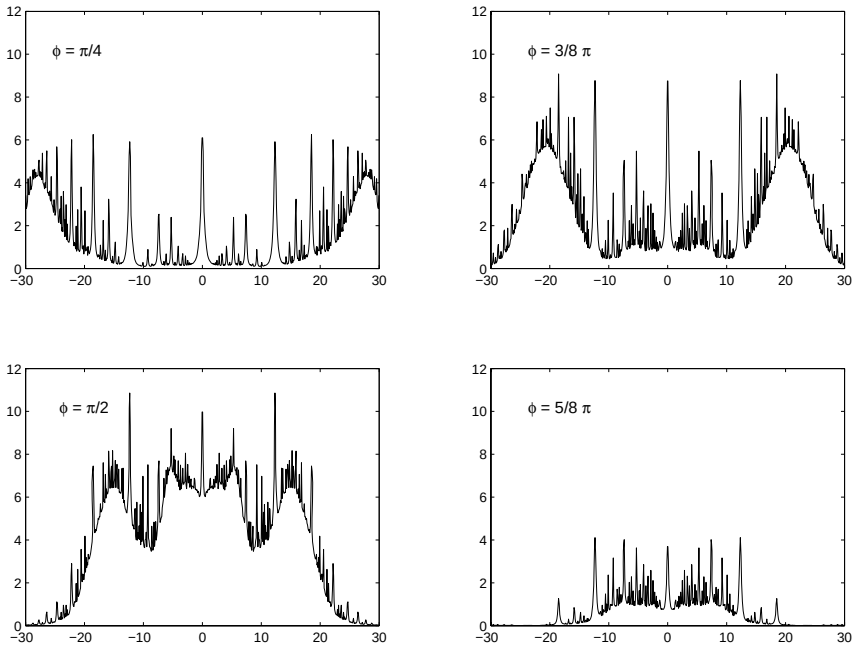

Figure 2.7 Force profiles for different relative phases. The force is given in multiples of $\hbar k\gamma$, the velocity in multiples of γ/k. The detuning $\delta = 37\gamma$ and the Rabi frequency $\Omega = 41\gamma$ have the same values as in the experiment. The relative phase used in the experiment is $\phi = \frac{\pi}{2}$.

The region where the light intensity is such that we get 2π-pulses ($\Omega = 58\gamma$) is zero as expected. In the case of 3π-pulses the force is getting bigger again, but this time the capture range is much smaller than in the case of π-pulses.

For a more detailed look at the region where the capture range becomes large, some force profiles are shown in figure 2.9. It can be seen that a trade-off between a large capture range and a large force was made when choosing the parameters for the experimental setup. It is also clear from all the numerical force simulations that the magnitude of the force gets much larger than with

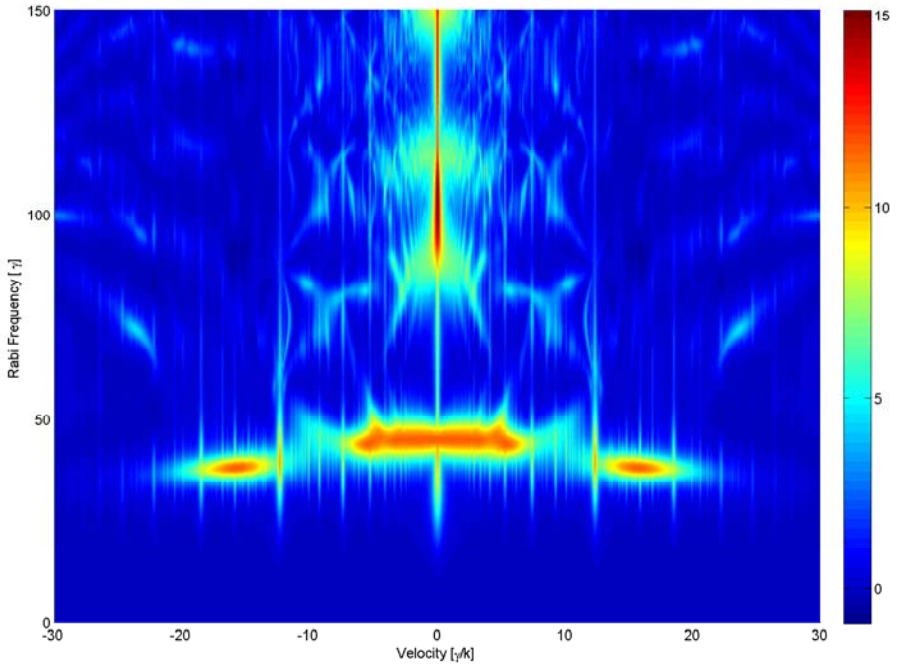

Figure 2.8 Dependence of the bichromatic force on the Rabi frequency. The parameters for the detuning and the relative phase are $\delta = 37\gamma$, $\phi = \frac{\pi}{2}$ as in the experiment. The magnitude of the force is shown by different colors in units of $\hbar k\gamma$.

monochromatic light fields ($F_{\mathrm{rad,max}} = \frac{\gamma}{2}\hbar\vec{k}$) and also the capture range can get huge compared to ordinary Doppler molasses ($v_{c,D} \approx \frac{\gamma}{k}$).

2.4.6 Bichromatic Collimation

To use the bichromatic force for collimation purposes the force profile has to be modified so that the force vanishes for atoms with velocity $v = 0$ and has a large negative gradient around that point. That can be achieved by detuning the frequencies to compensate for the Doppler shift (for a center velocity v_c)

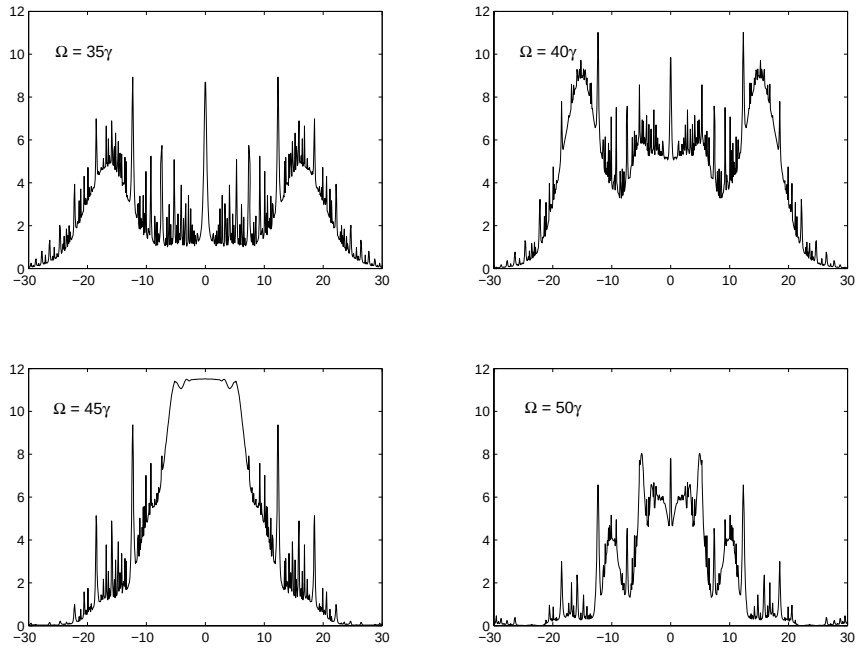

Figure 2.9 Force profiles for different Rabi frequencies. The force is given in multiples of $\hbar k\gamma$, the velocity in multiples of γ/k. The detuning $\delta = 37\gamma$ and the relative phase $\phi = \frac{\pi}{2}$ have the same values as in the experiment. The Rabi frequency used in the experiment is $\Omega = 41\gamma$.

and thereby moving the force profile from figure 2.7 with $\phi = \frac{\pi}{2}$ and adding a second force profile with reversed sign that is frequency shifted for atoms moving in the other direction. In our experimental setup the detuning to compensate for the Doppler shift is chosen to be $kv_c = \frac{\delta}{2} = 2\pi \cdot 30$ MHz. The numerical simulation of the resulting force profile is shown in figure 2.10. It has the necessary properties of a vanishing force for $v = 0$ and a negative force gradient $\frac{\partial F}{\partial v} < 0$ around that point. In that way it is similar to the force profile of optical molasses (cf. figure 2.3), but both the capture range and the

magnitude of the force are much larger.

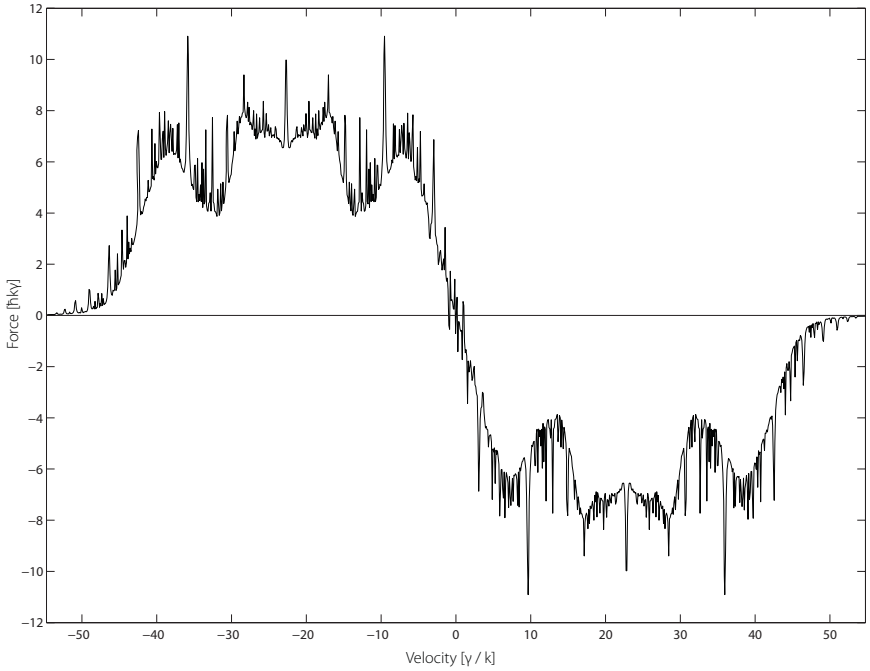

Figure 2.10 Numerical calculation of the force profile for bichromatic collimation. The parameters are those used in the experiment: $\delta = 37\gamma$, $\Omega = 41\gamma$, $v_c = \frac{\delta}{2}$, $\phi = \frac{\pi}{2}$.

Since the exciting and the deexciting pulse are coming from opposite directions, the frequencies in one beam have to be shifted by $+kv$, the other one by $-kv$ to compensate for the Doppler shift. That means that four frequencies in two beams are necessary for bichromatic collimation. Their relative position around the atomic transition frequency is shown in figure 2.11, the production of those frequencies is described in section 4.4.1. In the following description the two beams are often referred to by their Doppler detuning ($+kv$ and $-kv$).

Since the atoms absorb light from the $-kv$ beam and emit it into the $+kv$

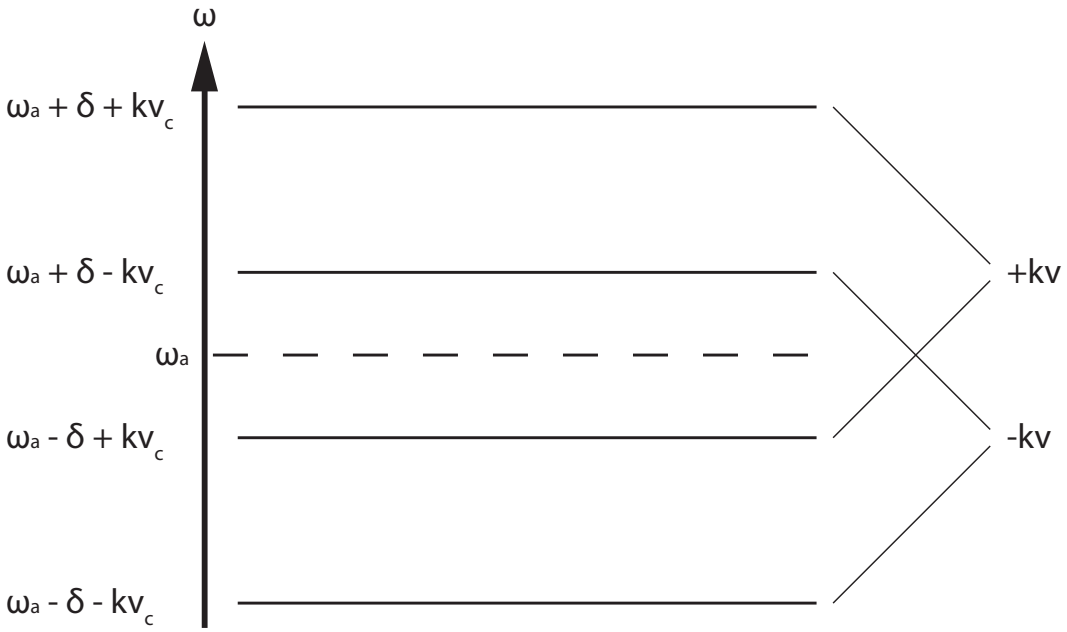

Figure 2.11 Frequencies for bichromatic collimation. The atomic transition frequency ω_a is shown as reference. The two beams carry the name of their Doppler detuning ($+kv$ and $-kv$).

beam, the arising force is dissipative even without spontaneous emission. In each absorption - emission cycle, the atom looses $2\hbar\left(\delta - kv_c\right) = \hbar\delta$ of kinetic energy.

The experimental setup is a little bit more complicated than in the case of optical molasses. It is not enough to just retroreflect the beams to get a push in the other direction because that would violate the phase condition that is necessary for the absorption - stimulated emission cycles. Instead a separate collimation region is necessary for each one-dimensional push, so that four collimation regions in total are needed for a 2D bichromatic collimation (see figure 4.16).

Chapter 3

Metastable Helium Apparatus

The vacuum system mainly consists of standard stainless steel components with copper sealed ConFlat flanges. Some of the components are modified or specially built. The connections for the roughing pumps and the helium inlet and outlet of the source are using Kwik-Flange^{TM}components. The beamline itself could in principle be used to create ultra high vacuum (UHV). However, due to frequent access to the system and components in the system that aren't especially designed for vacuum applications and therefore outgas, only high vacuum (HV) is achievable.

3.1 Metastable Helium

3.1.1 Helium Level Diagram

Helium is the noble gas whose metastable state (He*) has the highest internal energy (19.82 eV). This very high energy corresponds to light with

a wavelength of 62.6 nm and is therefore not accessible with today's lasers. In addition the transition from the helium (^{4}He) ground state 1^1S_0 to the metastable triplet state 2^3S_1 is not allowed in a nonrelativistic description. It is therefore necessary to produce the metastables in a DC electric discharge instead of using light to drive that transition.

The same selection rules that prohibit nonrelativistically any transition between the helium ground state and the metastable triplet state, namely that the total spin has to be preserved and that that only transitions with $\Delta L = \pm 1$ are allowed, assure on the other hand the extremely long lifetime of $\tau = 7900$ s [21]. Only relativistic effects [22] cause the lifetime even in absence of collisions (cf. section 3.1.2) not to be infinite. Therefore the metastable triplet state can be regarded as our actual ground state in the experiment and together with the 2^3P_2 state it forms our effective two-level atom (figure 3.1). This approximation can be made since the spin of the nucleus for ^{4}He is 0 which means that the spectrum shows no hyperfine structure and since the distance to the closest energy level (2^3P_1) is 2.29 GHz which is much bigger than any detuning from resonance used in the experiment. By using an optical pumping scheme (see section 4.4.3) only two levels out of the remaining magnetic sublevels (see figure 4.15) are involved in any transitions.

Some important experimental values for the $2^3S_1 - 2^3P_2$ and the $2^3S_1 - 3^3P_J$ transitions are summarized in appendix A. The latter one is also given since light with a wavelength of 389 nm can be created in our lab with a frequency doubled Ti:Sapphire laser. This might be particularly interesting

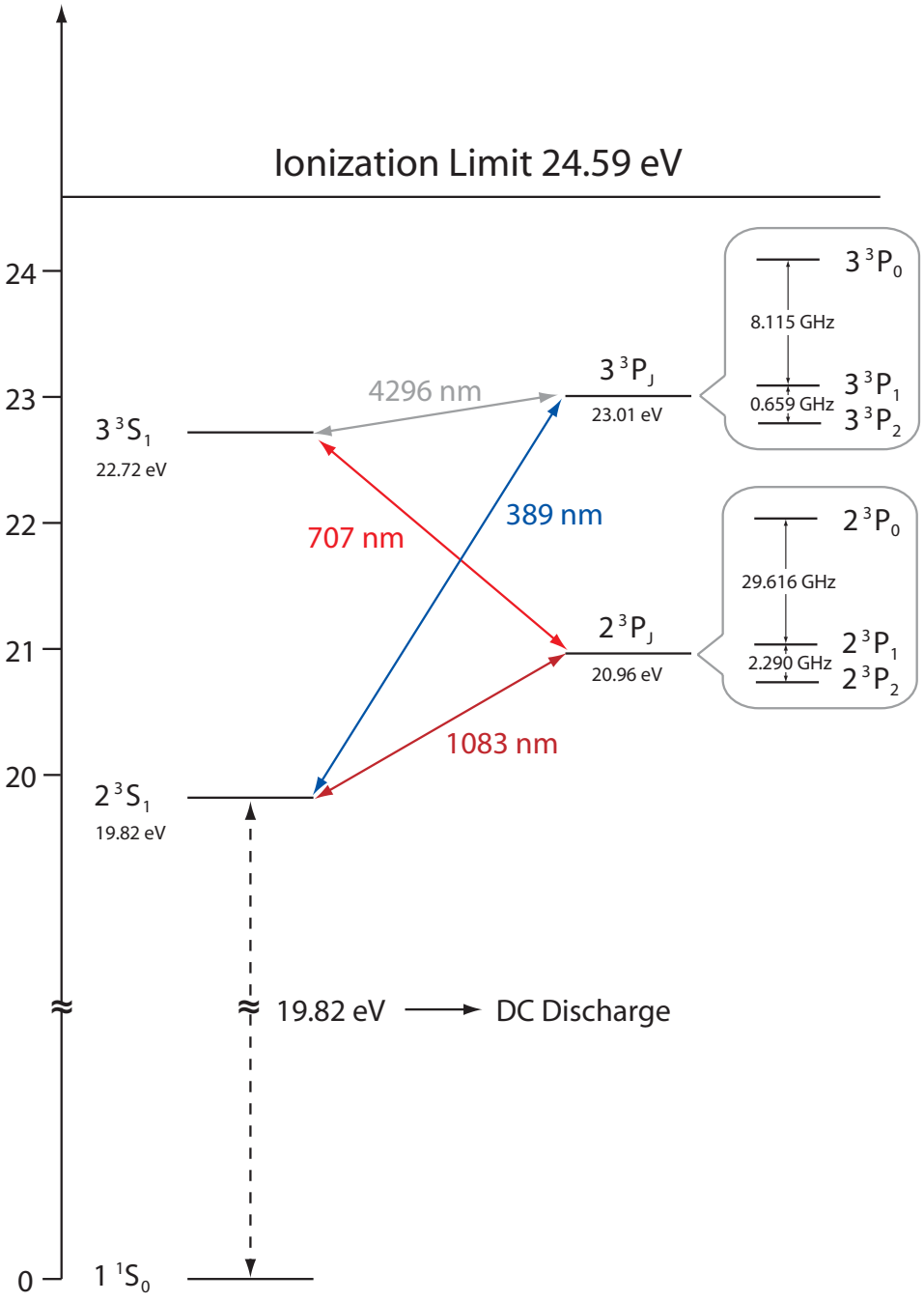

Figure 3.1 Selected energy levels of the helium atom. The 2^3S_1 state forms the effective ground state for the experiment. The spectroscopic data are taken from [23].

for the creation of light masks (see section 5.4) since the size of the structures that can be created is dependent on the wavelength of the used light. For the $2^3S_1 - 2^3P_2$ transition the low saturation intensity of $I_S = 0.17\ {}^{\mathrm{mW}}/_{\mathrm{cm}^2}$ should be emphasized because it enables the high saturation parameters that are necessary to exert huge forces on the atoms with the bichromatic force.

3.1.2 Deexcitation Processes

A good vacuum is a rather critical requirement for the experiment. It has to be guaranteed that the mean free path in the vacuum chamber is long enough that metastable helium atoms coming from the source can travel all the way down to the end of the beamline that is almost a meter away. Two major deexcitation processes can happen when a He* atom collides with another atom. In the process of Penning ionization (PI) [24] the He* atom gets deexcited while ionizing the other atom. The other process that can happen when two He* atoms collide is associative ionization (AI) where a singly ionized He_2^+ molecule is created

$$\mathrm{He}^* + \mathrm{He}^* \rightarrow \mathrm{He} + \mathrm{He}^+ + e^- \qquad \text{(PI)} \qquad (3.1a)$$

$$\mathrm{He}^* + \mathrm{X} \rightarrow \mathrm{He} + \mathrm{X}^+ + e^- \qquad \text{(PI)} \qquad (3.1b)$$

$$\mathrm{He}^* + \mathrm{He}^* \rightarrow \mathrm{He}_2^+ + e^- \qquad \text{(AI)} \qquad (3.1c)$$

AI is a process that only happens at very low energies so it probably doesn't contribute much to the deexcitation of He*. PI can in principle be largely suppressed by aligning the spins of the excited electrons but that is only worth

the effort if the phasespace density is dramatically increased (for example when creating a BEC out of metastable helium).

As a measure how often those collisions that deexcite the metastable helium atoms occur, the mean free path λ can be calculated. It is the average range a particle can move before it collides with another particle and can be calculated to be

$$\lambda = \frac{1}{\sqrt{2} n \sigma} = \frac{1}{\sqrt{2} n \pi d^2} \tag{3.2}$$

where n is the number density of the particles, σ is the collisional cross section and d the "diameter" of the particle. The factor $\sqrt{2}$ appears to account for the Maxwellian velocity distribution of the particles [25].

For helium the effective diameter is $d = 0.218$ nm [26]. Therefore using the relation

$$n = \frac{p}{kT} \tag{3.3}$$

the mean free path in our vacuum system ($p \approx 5 \cdot 10^{-6}$ Torr) at room temperature ($T = 300$ K) can be calculated to be

$$\lambda = \frac{kT}{\sqrt{2} p \pi d^2} \approx 29.4 \text{ m} \tag{3.4}$$

which is long enough to assure that most of the He* atoms make it to the end of the beamline. And even if you calculate the mean free path for air (since there are also other atoms in the vacuum system) the only thing that changes is the effective diameter ($d_{\text{Air}} = 3.74$ nm [26]) which reduces the mean free path by a factor of 3 compared to helium.

3.2 He* Source

For the production of our beam of metastable helium we use a reverse flow DC discharge source that was built at Universiteit Utrecht (Netherlands) and follows the design described by Kawanaka et al. in [27]. The source (see figure 3.2) consists of a pyrex glass tube 1 cm in diameter with a constricted end. Within that tube a tungsten needle of 1 mm diameter is held centered by ceramic spacers. The needle can be extended and retracted by means of a vacuum motion feedthrough. The needle is connected to a high voltage supply through a 170 kΩ high power (2 W) resistor. The negative high voltage creates a DC discharge between the sharpened tip of the needle and the nozzle plate and is regulated to about $2000 - 2500$ V to get a stable discharge current of approximately 6 mA.

On the outside of the glass tube, helium is flowing towards the narrowed end and most of it is pumped back through the glass tube by a mechanical pump (Welch Duo Seal, Model 1402). The flow of the helium is controlled at the He inlet with a small needle valve and is adjusted to get an inlet pressure reading of $600 - 650$ Torr and an outlet pressure reading of approximately 1.2 Torr. The pressure is measured at each position with an MKS Instruments, Inc. Convection Gauge that is controlled with a Terranova Dual Convection Gauge Controller (model 926) and since the gauges are calibrated for measuring air instead of helium the actual pressure certainly differs from the given numbers.

In the discharge region around the needle tip electrons are knocked off

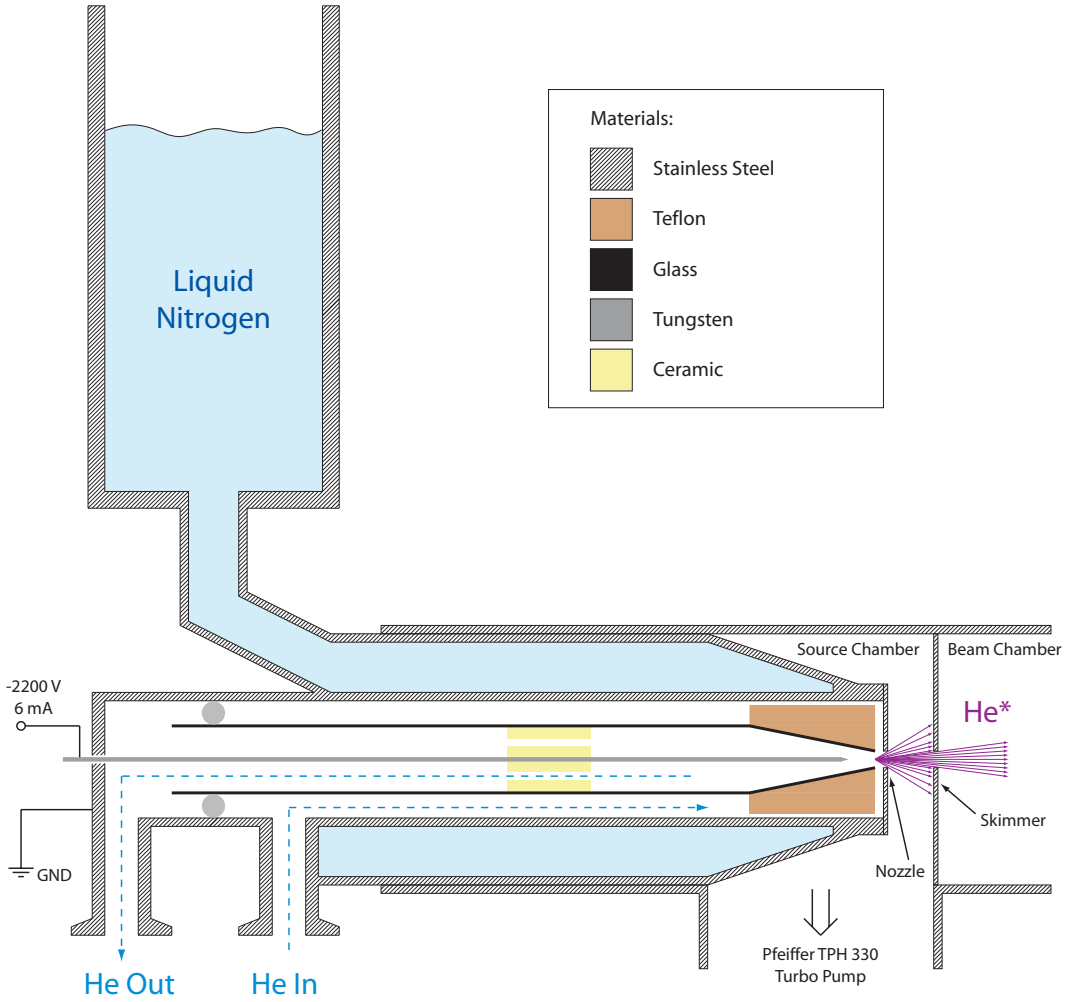

Figure 3.2 Drawing of the He* source. The position of the needle can be adjusted with a linear motion feedthrough and the color of the discharge between the nozzle and the skimmer plate can be checked by looking through a viewport (both not shown).

the helium atoms and accelerated towards the nozzle plate that serves as an anode. In the following recombination process, helium atoms in all different excited states are created, among these also atoms in the metastable 2^3P_2 state. Most of the atoms created within the plasma are immediately quenched to the ground state by collisions with other atoms but helium ions that recombine with electrons at the edge of the plasma or even behind the 0.5 mm hole of the nozzle plate are much more likely to escape towards the vacuum system since the particle density in those regions is lower. Besides the desired He* atoms in the 2^3P_2 state, also a lot of helium atoms in other states (especially ground state atoms), ions, electrons and UV light enter the beam chamber through the skimmer plate. In fact only one out of 10^4 to 10^5 atoms ends up in the metastable state. The region between the nozzle and the skimmer can be watched through a small viewport. That provides an easy mean of checking if the discharge is working correctly or if the source is contaminated since impurities in the supplied helium would change the color and the brightness of the discharge.

The glass tube is surrounded by a stainless steel jacket that is cooled by liquid nitrogen to 77 K. Since the helium is flowing between that jacket and the glass tube, it is cooled before it reaches the discharge region. The thermal contact between the cooled jacket and the helium is further improved by inserting a teflon spacer close to the narrow end of the glass tube that reduces the available space for the helium and makes it flow very close along the stainless steel jacket. Cooling the helium in the source helps to reduce the velocity

of the atoms coming out of the source. While He* sources with a similar design but without any cooling produce metastables with a center longitudinal velocity of ~ 1800 $^{m}/_{s}$ [28], the velocity can be decreased down to ~ 300 $^{m}/_{s}$ by using liquid helium to reach temperatures of around 10 K [29]. The velocity distribution of the metastables coming out of our source was measured by M. Cashen [30] by doing a time of flight (TOF) measurement. The center velocity of the atoms was found to be ~ 1000 $^{m}/_{s}$ with a FWHM of the velocity distribution of ~ 400 $^{m}/_{s}$.

3.3 Beam Chamber

The discharge region is separated from the rest of the vacuum system by the skimmer plate. The small hole (0.5 mm diameter) in the plate (~ 0.3 mm thickness) not only defines the He* beam but also allows for differential pumping. That way the pressure in the main part of the system doesn't increase too much while the source is running ($\sim 3 \cdot 10^{-6}$ Torr compared to $\sim 2 \cdot 10^{-6}$ Torr with the source off) whereas the pressure in the discharge region increases significantly during operation of the source ($\sim 1 \cdot 10^{-4}$ Torr compared to $\sim 1 \cdot 10^{-6}$ Torr). The pressure in both regions can be checked with Kurt J. Lesker G100F ion gauges. The vacuum is created by two Pfeiffer turbo pumps (TPH 330, pumping speed 330 $^{l}/_{s}$) that are controlled with Pfeiffer TCP 121 turbo pump controllers and backed with mechanical pumps (Pfeiffer DUO 10 for the source turbo, Welch Duo-Seal model 1376 for the beamline

turbo). The backing pressure is measured with two MKS Instruments, Inc. Convection Gauges that are connected to a Terranova Dual Convection Gauge Controller (model 926) and is typically $7 - 8$ mTorr for both the source and the beam chamber when the source is off. During operation of the source the backing pressure of the source turbo increases to approximately 150 mTorr. The complete vaccum system is drawn in figure 3.3.

3.3.1 Collimation Region

Directly after the skimmer is a 6" six-way cross welded to the system. For optical access four 6" viewports are attached to the four flanges of the cross that are perpendicular to the He* beam. To reduce reflections off the windows they are AR-coated for both 1083 nm and 389 nm light. The latter one could be used for driving the $2^3S_1 - 3^3P_2$ transition in metastable helium (cf. figure 3.1) but is not used for collimation purposes in our setup. The windows are almost 10 cm in diameter and therefore provide enough space for all four interaction regions for bichromatic collimation ($\sim$ 5 cm altogether) plus the interaction region for the high intensity optical molasses ($\sim$ 2 cm). Although the space for optical components that are necessary to align all the beams and send them through the system is limited it would be probably possible to put in a second low intensity molasses stage for further enhancing the brightness of the beam and decreasing its divergence (see section 4.5).

Since external magnetic fields influence the energy level structure of atoms according to the Zeeman effect we try to cancel at least the magnetic field

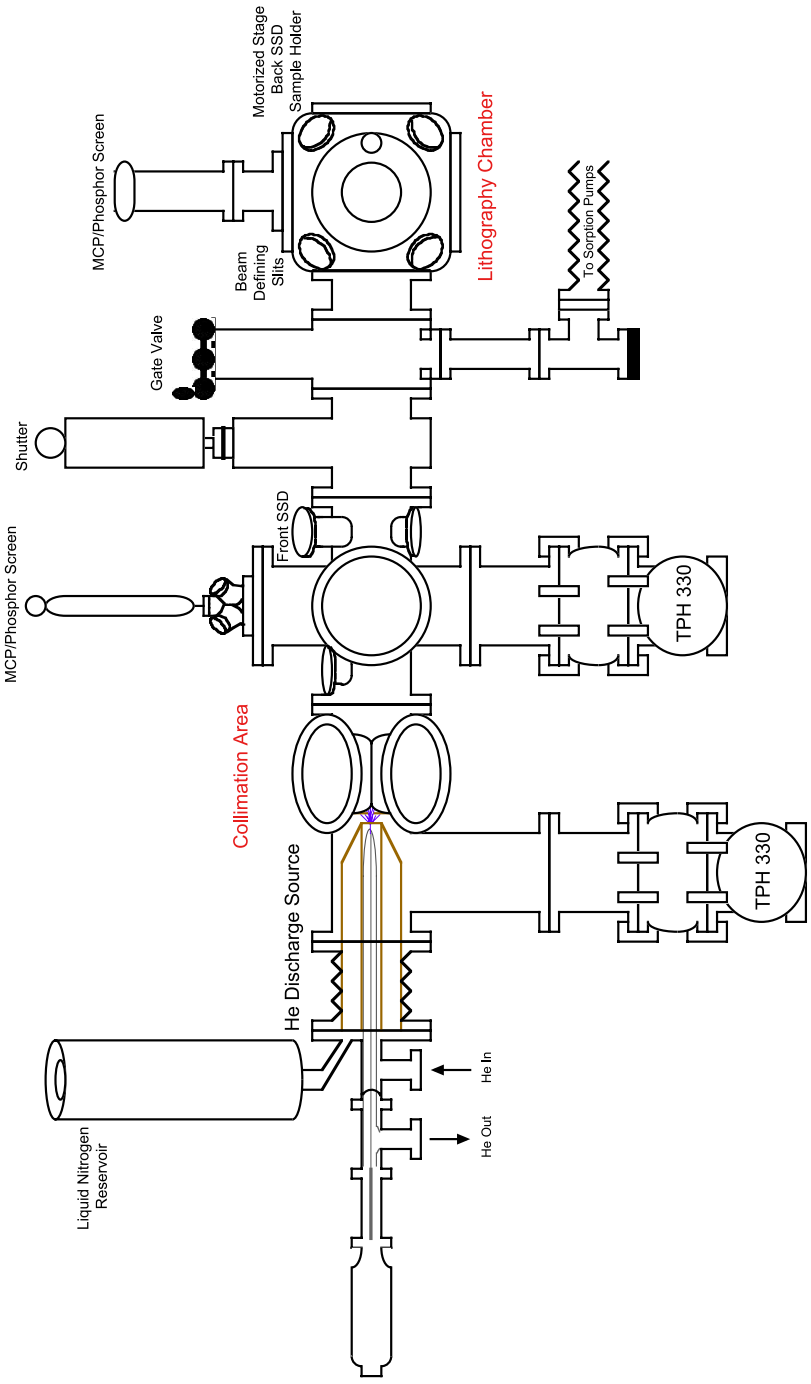

Figure 3.3 Drawing of the Complete Vacuum System. The system is drawn to scale. The distance from the discharge to the end of the beamline is ~ 1 m.

(earth's magnetic field plus stray fields) in direction of the beamline by applying an additional field with the same magnitude but opposite direction. To do so we measured the B-field along the beamline axis and attached coils on both sides of the collimation region to cancel the measured field ($= 3 \cdot 10^{-5}$ T).

3.3.2 First Detection Region

Following the collimation region a second 6" six-way cross serves for detection purposes. Directly after the collimation region two metal plates that are connected to 1000 V deflect any kind of charged particles coming out of the source. An MCP/Phosphor Screen for real time imaging of the atomic beam (see section 3.4.1) is mounted on a 4" motion feedthrough so that it can be retracted to let the beam pass. When the MCP/Phosphor Screen is used for spatial imaging of the beam the image can be viewed with a CCD camera through a window that is mounted to one of the flanges of the six-way cross. The distance from the skimmer plate to the MCP is 25 cm.

After the MCP/Phosphor Screen a stainless steel detector (SSD, see section 3.4.2) is installed that allows for determining the peak flux of the beam and quantitative imaging of the beam. The two slits that are used for the two dimensional scanning of the SSD are mounted on 2" linear motion feedthroughs and can also be retracted to let the beam go through. The motion feedthroughs as well as electric feedthroughs for the necessary electrical connections in this region of the vacuum system are connected to several 2 3/4" ConFlat flanges that are connected by 1 1/2" tubes to the six-way cross. The distance from

the skimmer to the SSD is 33 cm.

3.3.3 Second Detection Region / Lithography Chamber

The next part down the beamline is a manual shutter (Thermionics VLS-600/S) that doesn't seal tightly but can be used for quick blocking of the He* beam. Attached to the shutter is a Thermionics PFB-TLG-4000-H/R gate valve (4" inner diameter) that allows to separate the lithography chamber at the end from the rest of the vacuum system. Connected to the gate valve by a roughing line are two cryogenic sorption pumps (Vacuum Generators, Ltd. MS200 series) that are used for pumping down the sample chamber to approximately 10 mTorr before opening the gate valve to the system. The roughing line can be flooded with pure nitrogen in a controlled way to bring the cube up to air without contaminations from the ambient air getting into the system.

The lithography chamber itself consists of a 6" spherical cube from Kimball Physics (MCF600-SC600800-A) that has six 6" and eight 2 3/4" sealing surfaces. Two quick access doors (Nor-Cal ADV-600) with windows that are AR-coated for 1083 nm light are connected to the 6" openings on the sides that allow easy sample loading without loosening and tightening bolts for ConFlat connections. The two smaller openings on the upper side of the cube facing the source are used for blocking everything coming from the source except for the collimated beam to protect the wafer from complete exposure. To do so, two beam defining slits ($\sim$ 5 mm width for the vertical, $\sim$ 7 mm for the

horizontal one) were built out of sheet metal and connected to two 1" linear motion feedthroughs to center the slits around the beam peak.

To the top opening another MCP/Phosphor Screen (see section 3.4.1) is connected that can be moved up and down with a 2" motion feedthrough. The screen is just used for centering the beam defining slits around the He* peak and can be viewed by bare eye through one of the quick access door windows. The distance from the skimmer plate to the MCP is 79 cm.

To the back of the spherical cube two vacuum compatible miniaturized motorized stages (National Aperture MM-3M-F-1.5-VAC) are attached, one on top of the other, to allow for up to ±19 mm horizontal and vertical travel. The stages are controlled by two MicroMini MVP1 Controllers from National Aperture that are connected to a computer via RS-232 interface. The program for controlling the stages via PC is written in Visual Basic 6.0 and is explained in detail in appendix C. With a positioning accuracy of less than 0.5 μm, a repeatability better than 1 μm and a backlash of 19 μm, the stages allow precise positioning that is good enough for both placing the wafer and scanning the He* beam profile.

To allow for fast switching between scanning the beam and doing exposures, as well as switching between two samples, a home-made aluminum holder is attached to the stages which tightly holds specially machined aluminum pieces without the necessity of using any tools. Up to now three of these aluminum pieces were built, one of which is modified into an SSD with a pinhole (see section 3.4.2) that allows for measuring the profile of the metastable beam

88 cm away from the source skimmer. The other two can be interchangeably used for attaching wafers that then can be easily put in the vacuum system for doing exposures.

3.4 Detection of Metastables

To characterize the collimated beam of metastable helium we use two different detectors. Both rely on the high internal energy of He* that is released in collisions. A combination of a michrochannel plate (MCP) and a phosphor screen provides a good way for qualitative real-time imaging in two dimensions. For reliable quantitative measurements stainless steel detectors (SSDs) are used.

3.4.1 MCP/Phosphor Screen

At distances of 25 cm and 79 cm from the skimmer plate, a combination of a michrochannel plate (MCP) and a phosphor screen serve as retractable detectors for the He* beam. The MCP and the phosphor screen, together with a mirror that allows to see the image from the side (see figure 3.4(a)), are put together with Kimball Physics eV Parts. All electrical connections are done by using vacuum compatible wire that is connected to electrical feedthroughs with MHV connectors on the outside of the vacuum system.

The MCPs (Burle) consist of a large number of channels with 10 μm diameter that are created using glass drawing techniques as in the production of

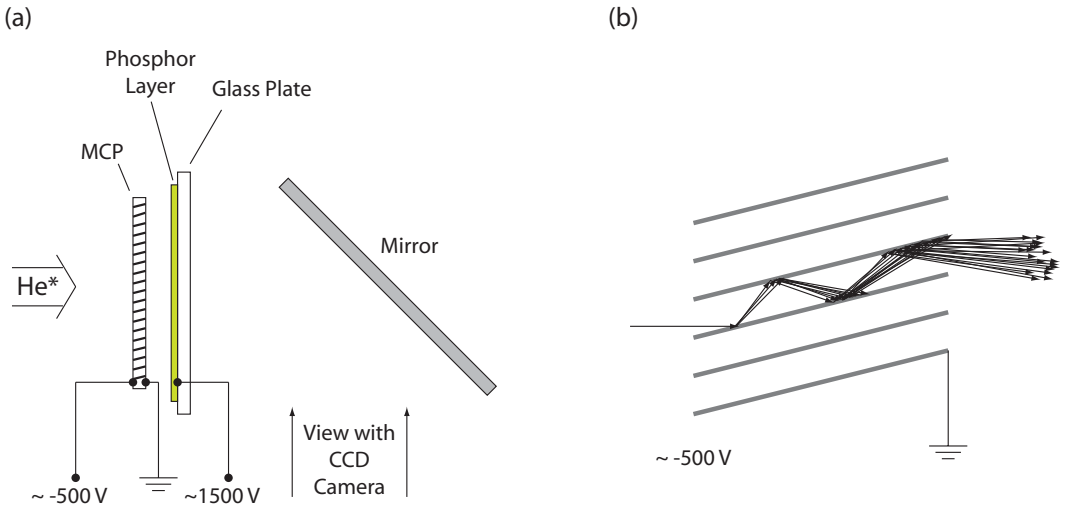

Figure 3.4
(a) Arrangement of the microchannel plate and phosphor screen as seen from the top. The mirror is inserted to be able to detect the phosphor screen image through a window at the side of the vacuum system.
(b) Principle of electron multiplication within a microchannel plate. The incoming He* atom knocks out the first electron that gets accelerated by the high voltage difference and creates large numbers of secondary electrons in electron-wall collisions within the microchannels.

fibers. The channels have a bias angle of 12° and are arranged on a hexagonal grid with a center to center spacing of 12 μm. The length/diameter ratio of the channels is 40 : 1 and a voltage difference up to 1000 V can be applied between the two sides of the MCPs. The active area of the MCP is 25 mm in diameter.

He* atoms hitting the MCP eject electrons from the inside of a channel. Due to the large voltage difference, these electrons are accelerated towards the back side of the MCP. On their way they frequently hit the walls of the channels thereby knocking out bunches of secondary electrons (see figure 3.4(b)) which leads to a signal amplification of up to $\sim 10^4$. In our setup we connect a

negative high voltage between 500 V and 700 V to the front side of the MCP and ground the back side which yields amplification factors of approximately $5 \cdot 10^2$.

The electron avalanche created by the MCP hits a phosphor screen behind it. The phosphor screens were manufactured by James van House (Vancouver, WA) and consist of a glass substrate that is coated with a thin conducting gold layer on top of which the phosphor layer is applied. The active area of the phosphor screen is also 25 mm in diameter. A positive voltage of $1000-2000$ V is connected to the gold layer to accelerate the electrons ejected from the MCP towards the phosphor screen. The electrons hitting screen cause the phosphor to fluoresce at around 450 nm so that the image can be recorded with a CCD camera that is connected to the computer via a TV tuner card.

The main advantage of this detector system is the real-time imaging in two dimensions which is essential for alignment purposes. On the other hand the response of the detector to the He* flux is not very linear which would make it necessary to use a calibration curve to get quantitative information about the number of atoms from that detector. But since the detector response changes over time and depending on the exposure history the gain of the system is spatially inhomogeneous and temporally changing. This makes it difficult to get reliable quantitative results for the beam flux from this detector.

3.4.2 Stainless Steel Detectors

The experimental setup contains two stainless steel detectors (SSD) at distances of 33 cm and 88 cm from the source skimmer respectively. The basic principle of these detectors is similar to that of a Faraday cup: the metastable atoms first pass an aperture and then hit a stainless steel plate where they eject secondary electrons with an efficiency of 70% [31]. These electrons are pulled towards the metallic aperture that is kept at 250 V. The back plate from where the electrons are ejected is connected to ground through a Keithley 486 picoammeter.

The SSD closer to the source consists of two parts that can be moved perpendicularly to each other. The front part is a stainless steel slit that defines the aperture in one dimension. The back part consists of another stainless steel slit that is perpendicular to the front one and the back stainless steel plate where the He* atoms impinge.

The aperture of the second SSD at the end of the beamline consists of a thin brass foil in which a small hole was machined via EDM (electrical discharge machining). The whole SSD is mounted in a way that it can easily be attached to the motorized stages that are controlled with a computer program (see appendix C). To be able to automate the whole scanning process, the analog output of the picoammeter is connected to an Ithaco 1201 Low Noise Preamplifier whose output is read out with a National Instruments NI USB-6008 data acquisition box (12 bit, 10 $^{kS}/_{s}$) that is connected to the computer via USB interface and is controlled with the same program that also controls

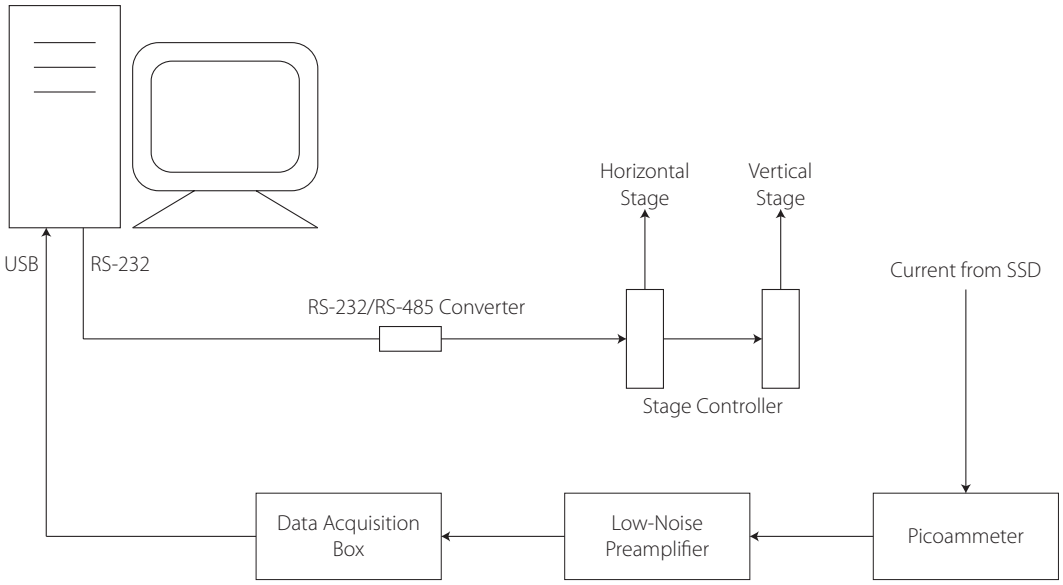

Figure 3.5 Schematics of the setup used to control the stages and readout the current measured by the back SSD.

the stages (see figure 3.5).

To be able to convert the reading from the picoammeter into a flux of metastable helium atoms, first of all the total current of He* atoms per pA has to be calculated. With an electron ejection efficiency of 70% we get

$$\sigma = \frac{\text{number of He* atoms}}{\text{s} \cdot \text{pA}} = \frac{1 \text{ pA}}{0.7 \cdot e} \frac{\text{atoms}}{\text{pA}} = 8.92 \cdot 10^6 \frac{\text{atoms}}{\text{s} \cdot \text{pA}} \tag{3.5}$$

The measured current is of course also dependent on the size of the aperture of the SSD. The more important number is therefore the flux per pA

$$\phi = \frac{\text{number of He* atoms}}{\text{s} \cdot \text{pA} \cdot \text{mm}^2} = \frac{\sigma}{A} \tag{3.6}$$

where A is the open area of the SSD aperture.

The width of the two slits that define the aperture for the first SSD and the diameter of the hole of the aperture of the second SSD were measured

by observing the diffraction pattern created when illuminating the openings with a HeNe laser. The results on the dimensions of the apertures and the corresponding flux per pA that were obtained that way are summarized in table 3.1.

	dimensions		ϕ
SSD1	width front slit	0.205 mm	$8.70 \cdot 10^7$ $^{\text{atoms}}/_{\text{s}\cdot\text{mm}^2\cdot\text{pA}}$
	width back slit	0.5 mm	
SSD2	diameter hole	0.456 mm	$5.46 \cdot 10^7$ $^{\text{atoms}}/_{\text{s}\cdot\text{mm}^2\cdot\text{pA}}$

Table 3.1 Dimensions and flux number for the two stainless steel detectors. The dimensions of the apertures were determined by analyzing the diffraction pattern created by shining the light of a HeNe laser through the apertures.

Chapter 4

Optical Setup

Laser light is used in the experiment for a number of different purposes: for capturing He* atoms coming out of the discharge source with bichromatic light, for further enhancing the brightness of the atomic beam with optical molasses and finally for patterning the atomic beam by using a standing light wave as a light mask. Although the detuning from atomic resonance and the required power is different for each of those applications, the light comes from only one initial light source and is repeatedly detuned with acousto optic modulators (AOM) and amplified by means of fiber amplifiers.

4.1 Light Production

4.1.1 Diode Laser

A Spectra Diode Labs SDL-6702-H1 Distributed Bragg Reflector (DBR) laser diode [32] produces light with a wavelength $\lambda = 1083$ nm that is both transverse and longitudinal single mode. To achieve this single mode behaviour, one part of the diode contains a grating that serves as a wavelength selective

element by causing destructive interference for wavelengths that don't fulfil the Bragg condition.

Since the wavelength of the laser diode light depends on temperature (0.084 $^{\text{nm}}/_{^{\circ}\text{C}}$ [30]), choosing the right temperature can be used as a mechanism for coarsely controlling the output of the diode. To get the correct wavelength for the $2^3S_1 - 2^3P_2$ transition in He* the temperature of the diode is kept stable at (24.1 ± 0.1) °C by an ILX Lightwave LDT-5910 temperature controller. A finer control of the wavelength is possible by adjusting the current of the laser diode which is done with a Thorlabs LDC 500 laser diode controller.

As mentioned in [32] the longitudinal modes of the laser diode cavity are spaced at 1.2 Å intervals and the Bragg grating has an estimated reflectivity bandwith of $\sim$ 5 Å. Therefore the cavity mode that is closest to the peak reflectivity of the grating becomes the lasing mode since its losses are smallest of all modes. When changing the current of the laser diode, the cavity modes change at a different rate than the wavelength with the lowest losses in the diode and therefore when turning up the current, 'mode-hops' from one cavity mode to a neighbouring one occur. This effect results in a hysteresis when varying the current and can be seen in figure 4.1 where the wavelength is measured with a Burleigh WA-1500 wavemeter. The correct wavelength for the $2^3S_1 - 2^3P_2$ transition in He* is 1083.33 nm and can hence only be reached by first turning up the current to $\sim$ 150 mA to get into the correct cavity mode and then turning it back down to $\sim$ 142 mA.

The laser diode current not only influences the emitted wavelength but also

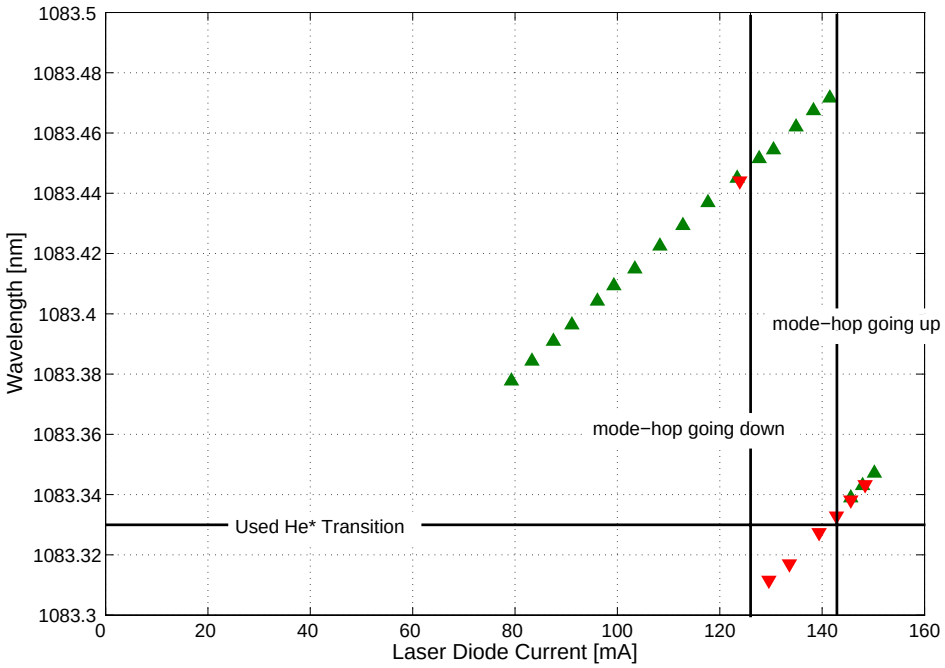

Figure 4.1 Wavelength dependence on the current through the laser diode at a temperature of 24.1 °C. The green upwards pointing triangles mark datapoints taken while turning the current up, the red downwards pointing triangles mark datapoints taken while turning the current back down.

the power of the light. The dependence of the output power (measured at the 70% output of the extended cavity, cf. figure 4.3) from the diode current at a temperature of 24.1 °C is shown in figure 4.2. After reaching a threshold of $\sim$ 75 mA the diode starts lasing and when turning the current up more the output power is increasing pretty much linearly. This graph also shows a slight hysteresis which is a consequence of the fact that under the given conditions the losses of one of the modes compared to the other are smaller.

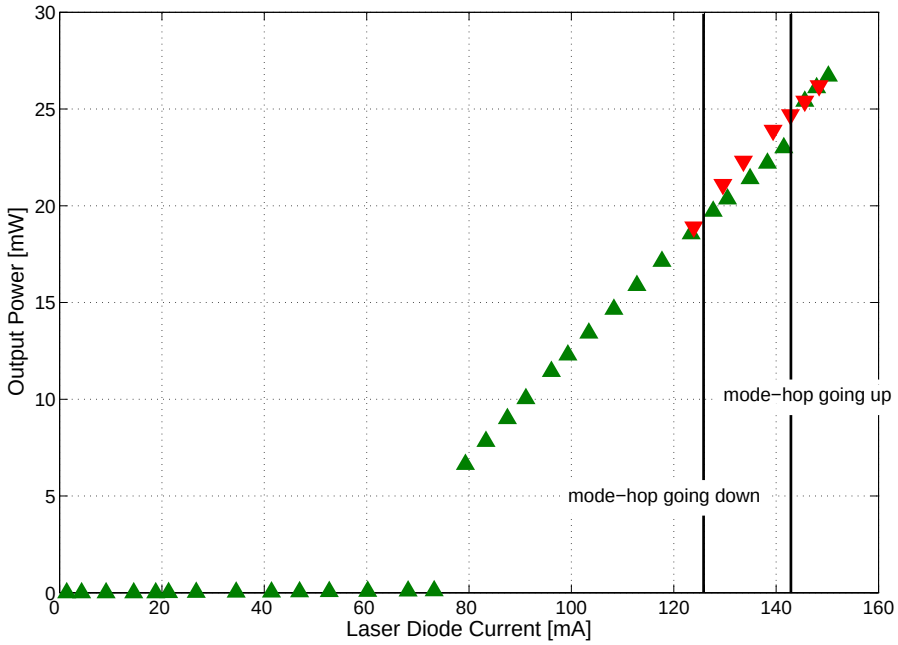

Figure 4.2 Dependence of the laser diode output power on its current at a temperature of 24.1 °C. The measurement was done with the stronger beam coming out of the extended cavity (cf. figure 4.3), so the measured power equals approximately 75% of the total power out of the diode. The green upwards pointing triangles mark datapoints taken while turning the current up, the red downwards pointing triangles mark datapoints taken while turning the current back down.

4.1.2 Extended Cavity

The linewidth of the diode laser is 3 MHz whereas the natural linewidth of the $2^3S_1 - 2^3P_2$ helium transition is 1.6 MHz. To narrow the linewidth of the diode an extended cavity is used (see figure 4.3) that artificially increases the lifetime of the photons within the diode by feeding back about 9% of the light into the diode. By doing so the linewidth is narrowed to approximately 125 kHz which is more than a factor of 10 less than the natural linewidth of

the He* transition. The narrowed linewidth was measured by using two DBR diodes of the same type and observing the beat signal that is created when beams with two different frequencies overlap and therefore interfere with a fast photodiode [30].

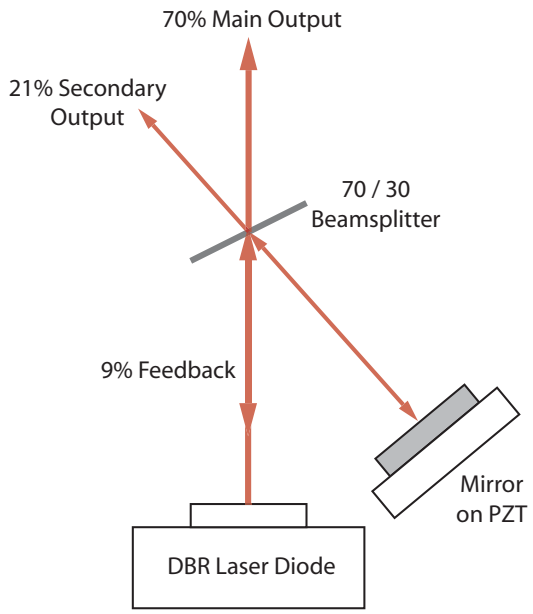

Figure 4.3 Extended Cavity of the Diode Laser. By using an external cavity to extend the lifetime of the photons within the cavity the linewidth of the diode laser is narrowed from 3 MHz to approximately 125 kHz. The length of the cavity is controlled with a PZT.

The extended cavity also offers another possibility for adjusting the output frequency of the laser. By using a mirror mounted on a Piezo-Electric Transducer (PZT) the length of the cavity and therefore the frequency of the diode can be changed by applying a voltage to the PZT. The PZT is driven by a homebuilt high voltage controller and used both for scanning over a broad frequency range to find the atomic transition as well as for feeding the error

signal back to the cavity to keep the laser locked to a specific frequency (see section 4.2).

A side effect of using a 70/30 beamsplitter in the setup is that two beams come out of the extended cavity with 70% and 21% of the total output power of the diode respectively. Both beams show the typical diode laser behaviour of greater divergence in one direction than in the other. Thus it is necessary to use not only spherical but also cylindrical lenses to collimate the outcoming beams. In addition to the collimation optics the beams pass through optical isolators (OFR IO-3-1083-HP for the stronger beam, OFR IO-D-1080-Z for the weaker beam) that rely on the Faraday effect to prevent backreflections of the laser light into the cavity. Both beams are then coupled into single mode optical fibers that not only make the guiding of the light easier and more flexible, but also serve as spatial filters by just transmitting the zero order Gaussian mode.

4.2 Frequency Locking

4.2.1 Saturated Absorption Spectroscopy

To lock our laser to the atomic transition frequency we use a He discharge cell. The cell is driven by a strong RF field of $\sim$ 52 MHz. That way also metastables are created in the cell so that a weak light beam that is resonant with the atomic $2^3S_1 - 2^3P_2$ transition is partly absorbed and scattered by the He* atoms. That leads to a dip in the transmission signal when the frequency

of the laser is scanned across atomic resonance. However, the width of that dip is Doppler broadenend (FWHM $\Delta\omega_D$, see figure 4.4(a)) as a consequence of the different speeds of the atoms within the gas cell.

One method of obtaining a signal that is not Doppler broadened is to use a saturated absorption spectroscopy (SAS) setup (see figure 4.5). In that case a strong ($I_{\text{pump}} \gtrsim I_{\text{sat}}$) counterpropagating pump beam is crossing the much weaker ($I_{\text{probe}} \ll I_{\text{sat}}$) probe beam. If the laser is slightly off-resonance the two beams are talking to different velocity groups in the gas cell; therefore the recorded transmission signal of the probe beam is the same as it was without the pump beam (cf. figure 4.4 (a),(b), situations (1) & (3)). In the case that the laser is resonant with the atomic transition, both beams address the same velocity group ($v_{\parallel} \approx 0$, $v_{\parallel}$ is the component of $\vec{v}$ in direction of $\vec{k}$) in the gas. Since the pump beam is much stronger, it excites a lot of atoms in that velocity group which leads to a reduced absorption of the probe beam. That leads to a detectable peak in the Doppler broadened signal (see figure 4.4 (a),(b), situation (2)). By using an additional beam (the reference beam) that is the same as the probe beam except that it does not cross the pump beam, a reference signal is created so that the Doppler broadened background can be subtracted, leaving just the narrower Doppler-free transmission signal. A more detailed description of saturated absorption spectroscopy can be found for example in [33].

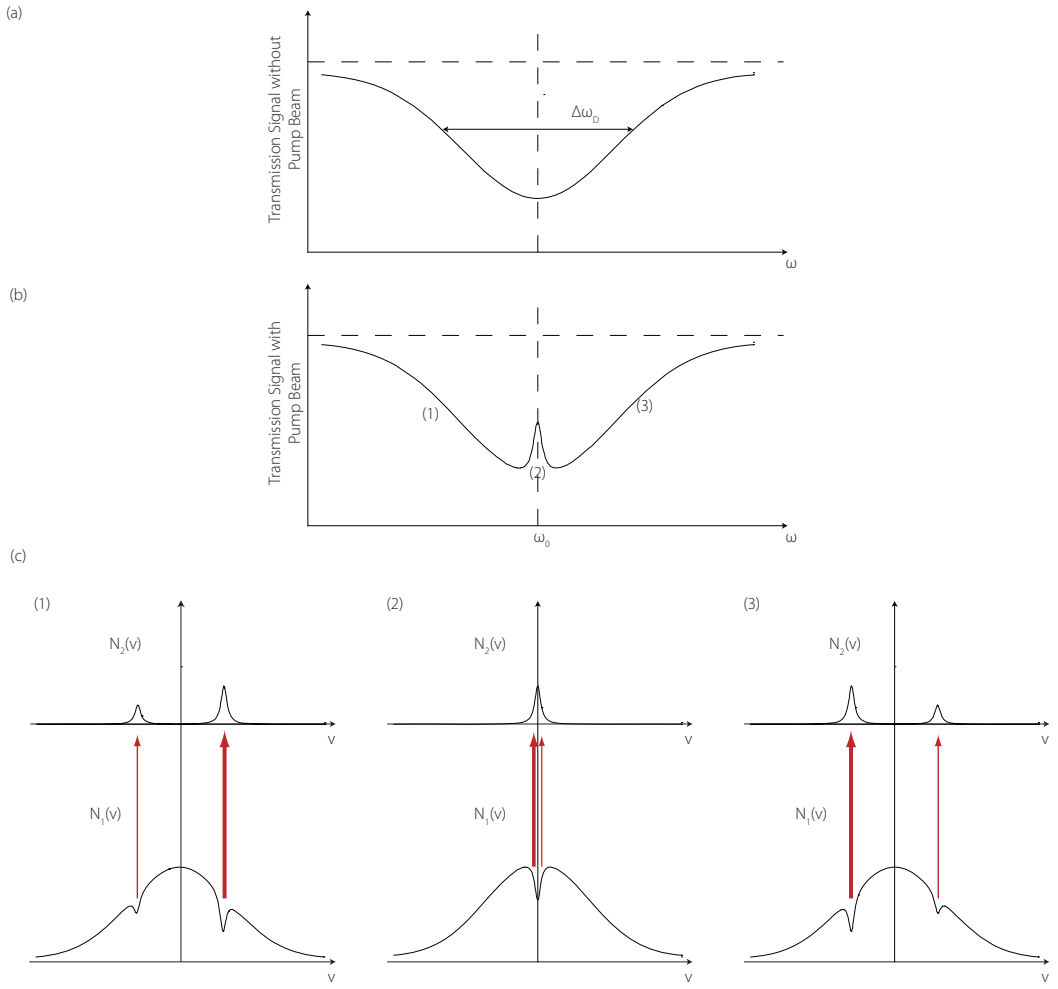

Figure 4.4
(a) In the transmission signal without the pump beam the atomic transition is Doppler broadened.
(b) When the pump beam is present, a small Doppler free signal can be seen on top of the broad dip due to saturation effects.
(c) Only if the laser is resonant with the atomic transition the pump beam and the probe beam talk to the same velocity group of atoms $v_{\parallel} \approx 0$. That leads to a higher transmission of the probe beam since the stronger pump beam saturates the absorption of that velocity group.

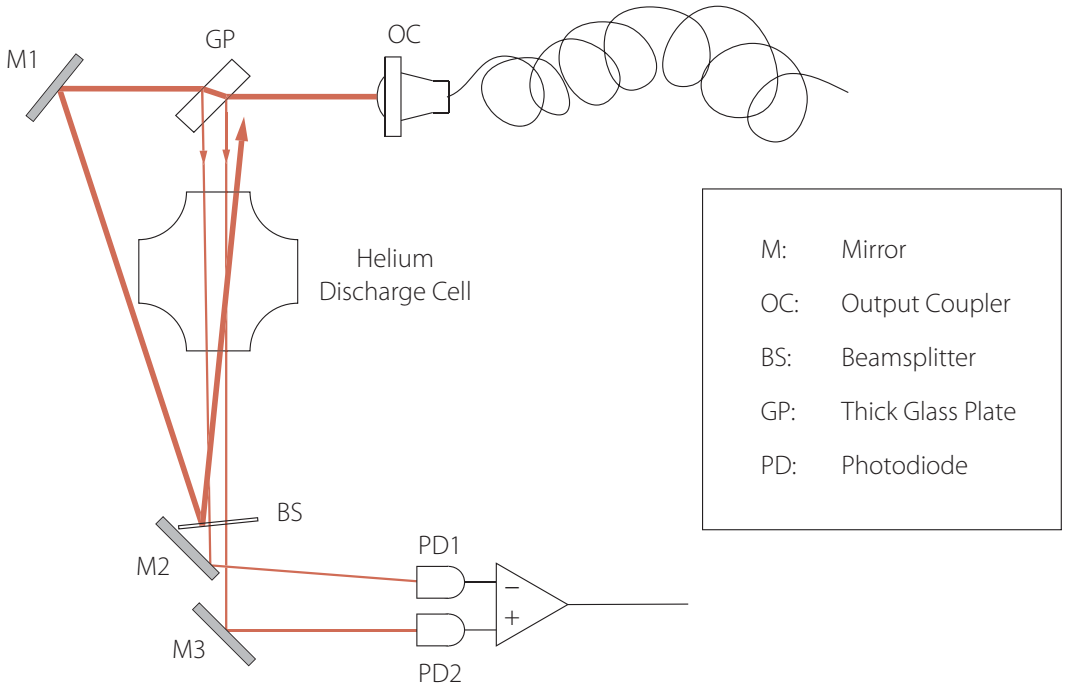

Figure 4.5 SAS Setup. Depending on the locking scheme, different signals can be connected to the output coupler. The pump and probe beam are not exactly counterpropagating to prevent backreflections in the laser diode which would make the frequency very unstable.

4.2.2 Locking Electronics

To lock the laser it is important to create an error signal from the Doppler-free transmission signal that can be used for a feedback loop to keep the laser stable. The schematics of the locking electronics is shown in figure 4.6. The signal coming from the SAS setup is first amplified with a Stanford Research Systems (SRS) SR560 low-noise preamplifier that is also used for filtering noise below 3 Hz and above 30 kHz. The signal is then fed into an EG&G Princeton Applied Research lock-in amplifier (model 5104). A lock-in amplifier is able to recover a signal that is modulated with a reference frequency even if the signal

is extremely noisy. The 10 kHz reference frequency in our setup is provided by an SRS DS345 30 MHz synthesized function generator that modulates the current driving the laser diode and therefore modulates the laser frequency. The lock-in amplifier is not only able to recover a signal but also to generate the derivative of that signal if the internal phase for the lock-in is set correctly. By doing so an error signal is created that is zero at the top of the peak, i.e. where the laser is exactly resonant with the transition. The lock-in amplifier is used with a time constant of 0.01 s and a sensitivity of 100 mV. The SAS signal and the corresponding error signal are shown in figure 4.7.

The error signal is then connected to an SRS SIM960 analog PID controller whose output signal can be calculated according to

$$\begin{aligned} \varepsilon &= \text{Setpoint} - \text{Measure} \\ \text{Output} &= P \times \left\{ \varepsilon + I \int \varepsilon \mathrm{d}t + D \frac{\mathrm{d}\varepsilon}{\mathrm{d}t} \right\} + \text{Offset} \end{aligned} \tag{4.1}$$

That means that, depending on the chosen parameters, the PID controller reacts to fast changes in the error signal (large D) or tries to keep the error signal more constant (large I). The parameters used in our setup are given in table 4.1

The stabilized error signal is then applied to the PZT of the extended cavity of the laser to compensate any fluctuations. By inserting the PID controller in the setup and adjusting the parameters it is now possible to lock the laser for several hours without any intervention whereas before, a constant adjusting by hand was necessary to keep the laser approximately at resonance.

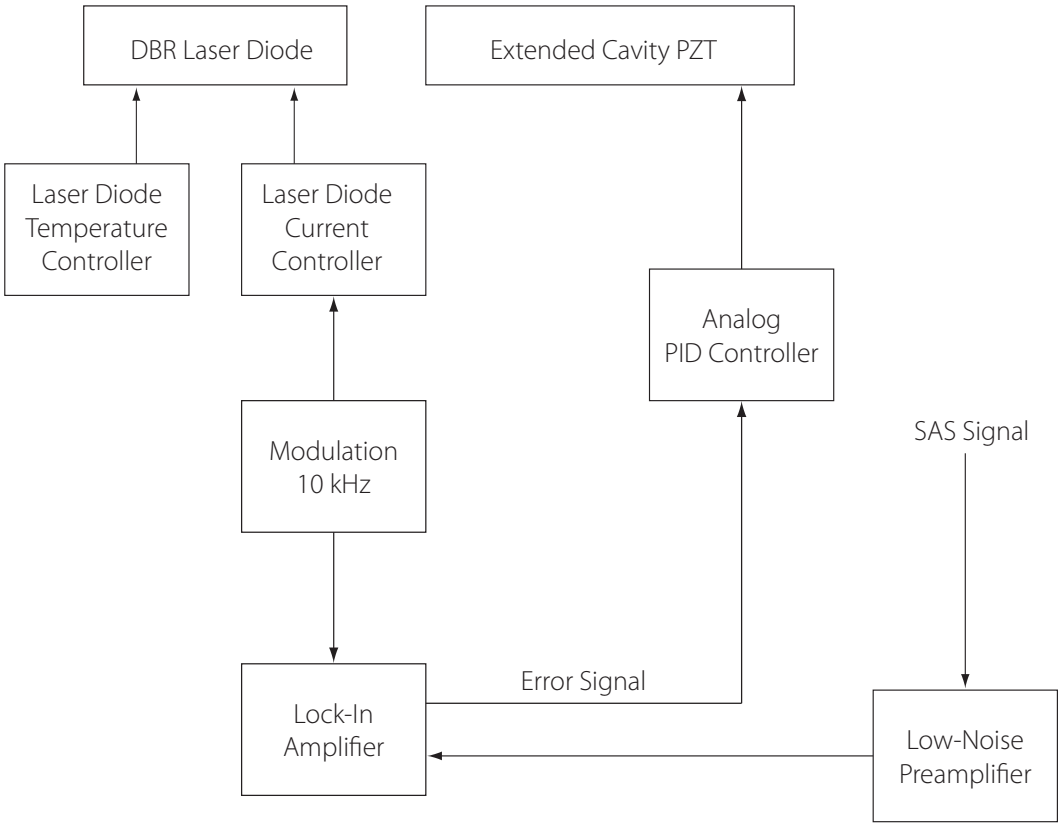

Figure 4.6 Schematics of the locking electronics. Details about the components can be found in the text.

4.2.3 Off-Resonance Locking

For locking the laser to atomic resonance, i.e. $\omega = \omega_a$, the secondary output of the extended cavity of the laser (see figure 4.3) is used for the SAS (see figure 4.7 for the SAS signal and the error signal). In this case the $+kv$ beam contains a component of ω_a and a push of atoms can be detected on the MCP/Phosphor Screen. Therefore that locking scheme is used for aligning the $+kv$ beams to which all other beams are aligned afterwards.

For bichromatic collimation on the other hand it is necessary to lock the

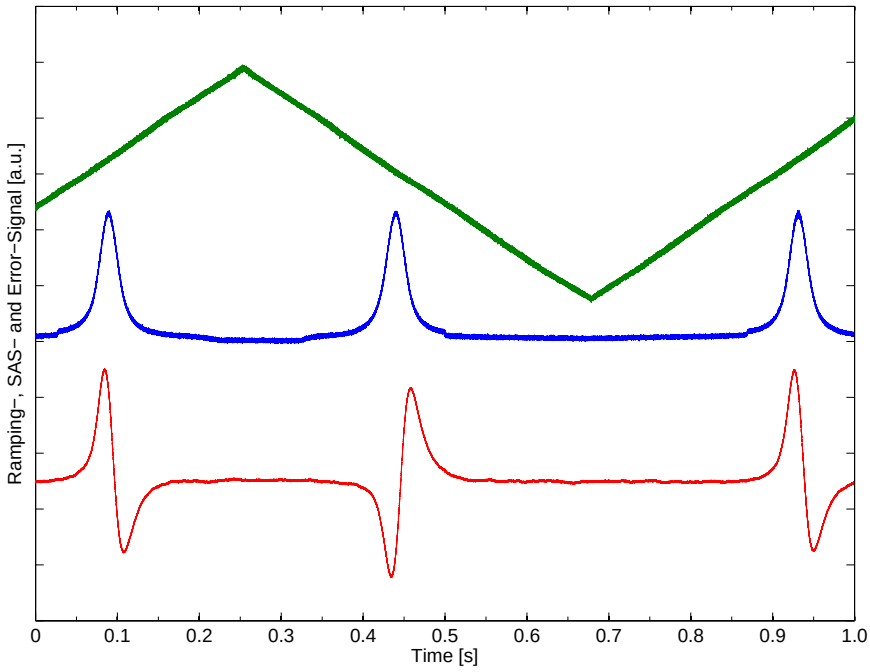

Figure 4.7 The figure shows the SAS signal (blue) and the arising error signal (red) for the first locking scheme. The frequency of the ramping (green) is slowed down to $\sim$ 1 Hz to display the error signal more accurately on the oscilloscope. Usually the scanning frequency is $\sim$ 30 Hz.

laser to $\omega_a - kv_c = \omega_a - 2\pi \cdot 30$ MHz. To do that part of the $-kv$ beam is sent through an AOM that changes the frequency components by $\frac{3}{2}\delta = 2\pi \cdot 90$ MHz, so that it then contains the frequencies $\omega + \frac{\delta}{2}$ and $\omega + \frac{5\delta}{2}$. By sending that modified signal to the SAS it is possible to lock the laser on the lower frequency component which leads to $\omega_a = \omega + \frac{\delta}{2} \rightarrow \omega = \omega_a - \frac{\delta}{2}$, the necessary result for bichromatic collimation (see section 2.4.6).

The SAS signal from that second locking scheme and the created error signal can be seen in figure 4.8. The third peak in between the two frequency

Parameter	Value	
P (gain)	-2.5	
$I = \frac{1}{T_i}$	$8.0 \cdot 10^1$	$1/s$
$D = T_d$	$4.0 \cdot 10^{-4}$	s
Internal Setpoint	0	V
Offset	0	V

Table 4.1 The settings for the PID controller in the laser locking setup. The value for P has to be adjusted sometimes to account for changes in the strength of the signal coming from the SAS cell.

components of the modified $-kv$ beam is a cross-over resonance that arises from the fact that the atoms see the two frequency components as an amplitude modulated signal of the average frequency of both parts. The locking is done on the peak that corresponds to a lower voltage on the PZT of the extended cavity.

4.3 Light Amplification

4.3.1 Fiber Amplifiers

One of the big advantages of working with laser light of a wavelength between 1000 nm and 1600 nm is that a broad range of products that were designed for the telcommunication industry are readily available. Most of them have been on the market for a while and therefore are well-tested and are easy to use. Since many of these products are fiber coupled they are easy to implement in an existing setup that uses fibers. One type of those products are fiber amplifiers.

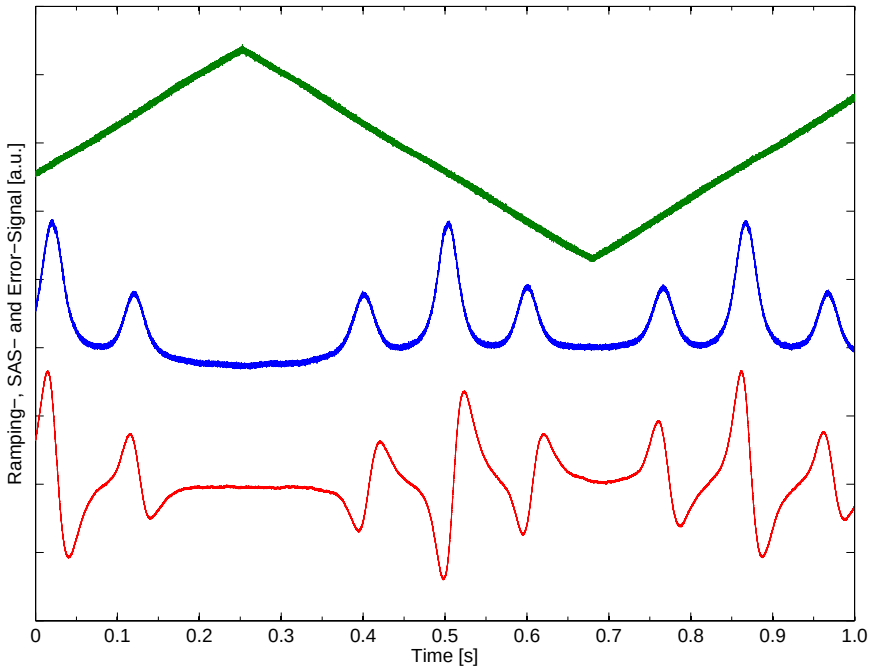

Figure 4.8 The figure shows the SAS signal (blue) and the arising error signal (red) for the second locking scheme. The frequency of the ramping (green) is slowed down to ~ 1 Hz to display the error signal more accurately on the oscilloscope. Usually the scanning frequency is ~ 30 Hz.

For the experiment we have three fiber amplifiers. They all use ytterbium (Yb) doped single mode fibers as a gain medium. The fibers are coiled inside the amplifier and are pumped with light at a wavelength of $900 - 1000$ nm to create population inversion. Light ($1050 - 1090$ nm) travelling through the fiber causes stimulated emission into the same mode and therefore the light gets amplified.

The two newer and bigger models we use are KPS-BT2-YFA-NLS-1083-40-COL fiber amplifiers from Keopsys. They contain three independent pump

lasers that work on different parts of the fiber and are seperated by optical isolators to prevent light in the opposite direction to get amplified. The first pumping diode (preamplifier) amplifies the incoming light to about $120 - 150$ mW pretty much independent of the power of the light at the input. Further amplification can be achieved by turning up the two additional diodes (booster stages). Since their current can be smoothly adjusted, any output power between the power given by the preamplifier and the maximum output power of 4 W can be achieved.

The input and output fibers are connectorized with FC/APC connectors that are angle-polished at an 8° angle to reduce backreflections. At the high powers that are created with these amplifiers, a little bit of dust or some stray reflection back into the output connector can damage the fiber by blowing off the tip as happened with one of the amplifiers. When reconnectorizing that fiber, special care had to be taken in the polishing process to make sure that no light will be backreflected from the freshly polished tip. In addition it is very important to have clean output couplers and optics should be AR-coated to minimize harmful backreflections.

Another thing that can severely damage the fiber amplifier is a too low input power because that allows for the amplification of light that is spontaneously emitted in the backward direction. Therefore the amplifier constantly monitors and displays the input power. The minimum input power recommended by the manufacturer is -3 dBm $\equiv 0.5$ mW.

Both amplifiers have been widely tested within the lab after they were

purchased in late 2003. Especially concerns about nonlinear effects within the amplifiers when going to very high powers existed but could be eliminated [34].

The third amplifier is an OIYb30 fiber amplifier from Optocom Innovation (the company that later became Keopsys). It has just one pump diode, no display of the input power and no optical isolators inside. The maximum output power of that amplifier is 1 W.

4.3.2 Polarization Control with Fibers

It is often necessary, or at least desirable, to control the polarization of the light coming out of a fiber. Several possibilities have been studied of how to control the polarization. They basically all rely on birefringence within the fiber that can be created by making the fiber core elliptical, applying lateral stress on the fiber (the two big fiber amplifiers contain such a device for controlling the output polarization) or twisting the fiber [35]. Another way of creating birefringence wihtin a fiber that is easy to implement is the bending of fibers.

Birefringence in Bent Single-Mode Fibers

The birefringence in a bent single-mode fiber is essentially a stress effect [36]. Therefore basic elasticity theory can be used to calculate the stress within a bent fiber that creates an elasto-optic change in the index of refraction. The presented derivation assumes that the fiber core is made out of an isotropic material which is true for the fibers used in our experiment since they consist of Germanium doped fused silica (SiO_2).

In such an isotropic medium the elastic modulus E, also known as Young's modulus, is defined as the ratio of the stress $\sigma = \frac{\text{Force}}{\text{Area}}$ applied to an material and the resulting strain $\varepsilon = \frac{\text{Change in Length}}{\text{Length without Stress}}$

$$E = \frac{\sigma}{\varepsilon} = \frac{F/A}{\Delta l/l} \tag{4.2}$$

In most media an applied unidirectional stress not only causes a strain in that specific direction but also in the other directions. The magnitude of that effect is described by Poisson's ratio ν which is defined as

$$\nu = \frac{\Delta l_x/l_x}{\Delta l_z/l_z} = \frac{\Delta l_y/l_y}{\Delta l_z/l_z} \tag{4.3}$$

if the applied stress is directed in z-direction and analogously for the other directions.

From Eq. (4.2) and Eq. (4.3) it is easy to derive the difference in the strains in x- and y-direction

$$\begin{aligned} \varepsilon_x &= \frac{\Delta l_x}{l_x} = \frac{\sigma_x}{E} - \nu\left(\frac{\sigma_y}{E} + \frac{\sigma_z}{E}\right) \\ \varepsilon_y &= \frac{\Delta l_y}{l_y} = \frac{\sigma_y}{E} - \nu\left(\frac{\sigma_x}{E} + \frac{\sigma_z}{E}\right) \\ \varepsilon_x - \varepsilon_y &= \frac{1}{E}\left(\sigma_x - \sigma_y\right)(1+\nu) \end{aligned} \tag{4.4}$$

For a single-mode fiber with outer diameter $2r$ and curvature $\kappa = 1/R$ (figure 4.9) the bending induced stress in the z-direction is

$$\sigma_z(x) = E\frac{\Delta l_z}{l_z} = \kappa E x \tag{4.5}$$

We consider the fiber to be only weakly bent, i.e. $\kappa r \ll 1$. The bending radius of the layer dx in figure 4.9(b) is $(R + x)$. The stress $\sigma_z(x)$ in this layer

contributes for a small lateral stress component σ_x with $|\sigma_x| \ll |\sigma_z|$ and

$$\sigma_x(x+dx) - \sigma_x(x) = (R+x)^{-1}\,\sigma_z(x)\,dx \tag{4.6}$$

If we now neglect $|x| \ll R$, we can transform Eq. (4.6) into

$$\frac{\partial \sigma_x}{\partial x} = \kappa^2 E x \tag{4.7}$$

which can be integrated with the boundary conditions $\sigma_x(\pm r) = 0$ to obtain

$$\sigma_x(x) = \frac{\kappa^2 E}{2}\left(x^2 - r^2\right) \tag{4.8}$$

When doing so we neglect any stress component in y-direction ($\sigma_y = 0$) which is justified since the fiber is only bent in the x-direction and considered not to be twisted.

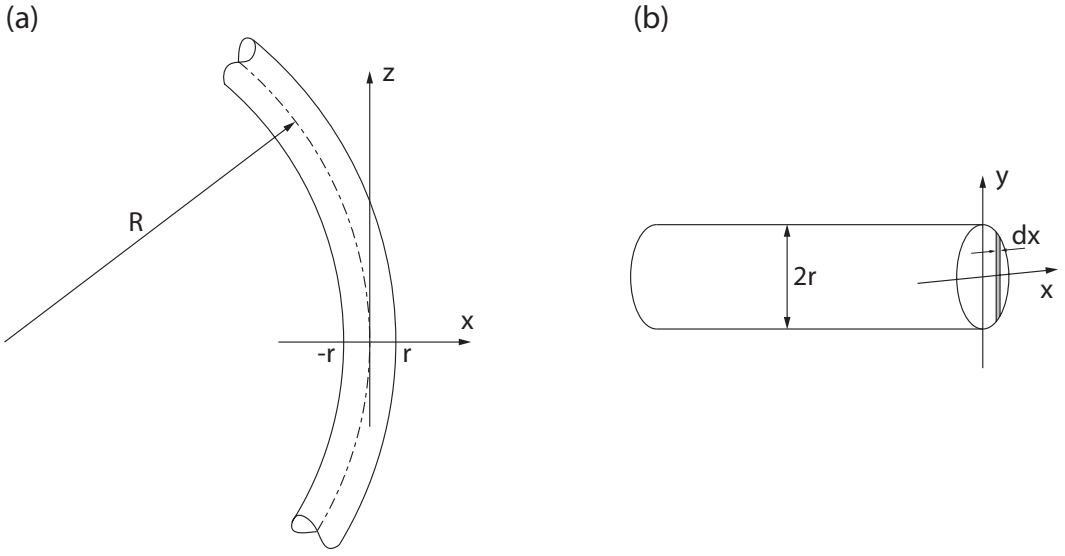

Figure 4.9 Geometry of the bent fiber. The fiber with outer diameter $2r$ is bent in x-direction with a radius of curvature R. The unbent fiber is oriented in z-direction.

Stress can change the refractive index n of a medium. This is called the photoelastic effect and the change in the refractive index was found to behave as [37]

$$\Delta\left(\frac{1}{n^2}\right)_i = p_{ij}\varepsilon_j \tag{4.9}$$

where the photoelastic constants p_{ij} are material dependent.

Since the relative variations of the index of refraction due to applied stress are always small, Eq. (4.9) can be evaluated by differentiation

$$\begin{aligned} &\frac{\Delta\left(\frac{1}{n^2}\right)_i}{\Delta n_i} \approx \frac{d\left(\frac{1}{n^2}\right)_i}{dn_i} = -2\frac{1}{n^3} \\ &\Rightarrow\ \Delta n_i = -\frac{n^3}{2}p_{ij}\varepsilon_j \end{aligned} \tag{4.10}$$

By combining Eq. (4.4), Eq. (4.10) and Eq. (4.8), and keeping in mind that the stress in the y-direction σ_y is considered to be 0, it is easy to express the difference in the refractive index for light polarized in x-direction or y-direction respectively in terms of material constants

$$\begin{aligned} \Delta n_x - \Delta n_y &= -\frac{n^3}{2}\left(p_{11}\varepsilon_x + p_{12}\varepsilon_y - p_{21}\varepsilon_x - p_{22}\varepsilon_y\right) \\ &= -\frac{n^3}{2}\left(\varepsilon_x - \varepsilon_y\right)\left(p_{11} - p_{12}\right) \\ &= -\frac{n^3}{2E}\left(\sigma_x - \sigma_y\right)\left(1+\nu\right)\left(p_{11} - p_{12}\right) \\ &= 0.25\kappa^2 n^3 r^2\left(p_{11} - p_{12}\right)\left(1+\nu\right) \end{aligned} \tag{4.11}$$

Lefèvre Fiber Polarization Controller

Since the birefringence of the fiber is changed depending on the way the fiber is curved, bending and attaching the fiber in a special way provides an easy way

of roughly controlling the output polarization of a fiber. A more sophisticated way of utilizing the photoelastic effect in bent fibers is by using fiber loops as waveplates whose retardation is defined by the number and the radius of the loops [38].

The core of the fiber used for the polarization controller (Thorlabs P3-980A-FC-5 with 900 μm protective tubing) is doped with Germanium. According to Thorlabs, the amount of Ge in the silica core is small ($< 10\%$) but more details aren't disclosed by the manufacturer. But since the index of refraction of the fiber core (according to Thorlabs $n = 1.4563$ for $\lambda = 1064$ nm) is close to the value for pure fused silica ($n = 1.4494$ for $\lambda = 1083$ nm [39]), the rest of the material constants is also considered to be similar.

In table 4.2 the necessary values for the calculation of the retardation are given. Since no information could be found on the dependence of the photoelastic constants p_{ij} on the wavelength of the light and the only data available for fused silica is for a wavelength of 633 nm, those values are used to get at least a rough estimate on the phase delay. No test of the accuracy of these calculations has been done in our laboratory so far.

By using Eq. (4.11) to calculate the difference in the index of refraction for light polarized along the ordinary and the extraordinary axis, respectively, we get $\Delta n_x - \Delta n_y = -0.133\kappa^2 r^2$.

In our setup we use a Thorlabs FPC560 polarization controller that has three paddles that can be rotated independently by up to $\pm 117.5^\circ$ and curl the fiber (cladding diameter $2r = 125$ μm) in a variable number of loops with a

Quantity	Value	Wavelength
Refractive Index n	1.4494	1083 nm
Photoelastic Constant p_{11}	0.121	633 nm
Photoelastic Constant p_{12}	0.270	633 nm
Poisson's Ratio ν	0.17	independent of λ

Table 4.2 Some material constants for fused silica. No value for the photoelastic constants could be found in the literature for $\lambda = 1083$ nm. All values are taken from reference [39].

diameter of $2R = 56$ mm. With the parameters for the fiber that is used, that gives a retardation of $2\pi R\,(\Delta n_x - \Delta n_y) \approx 116$ nm per loop. The schematics of the polarization controller are shown in figure 4.10. We use two loops each in the first and the third paddle and five loops in the second paddle which are the values that are closest to acting as a set of waveplates with $\frac{\lambda}{4}$, $\frac{\lambda}{2}$ and $\frac{\lambda}{4}$ retardation. This setup gives us precise control over the polarization coming out of the fiber.

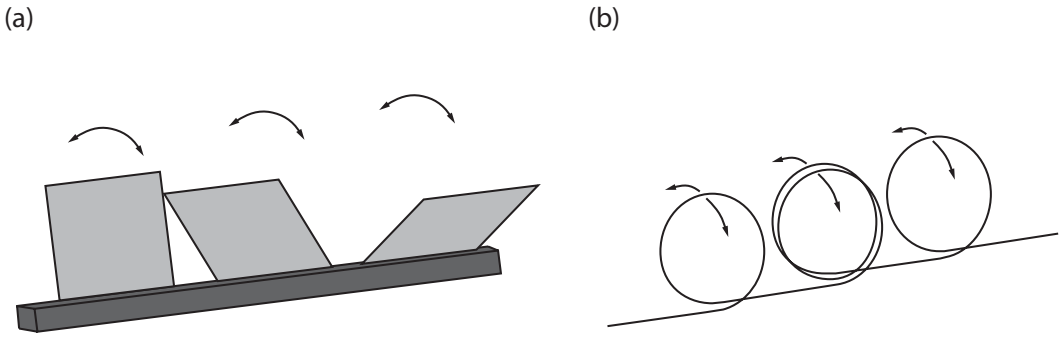

Figure 4.10
(a) Schematic of the Fiber Polarization Controller
(b) Configuration of the fiber within the polarization controller (not all loops are drawn to keep the drawing clearer). Each plane of coils can be individually rotated.

4.3.3 Dual Signal Amplification

The experimental setup involves four different beams with different frequencies: $+kv$ and $-kv$ for Bichro, one beam for molasses and one beam for patterning the He* beam with a light mask. Since we have only three fiber amplifiers for amplifying the signals, a new setup for the amplification was necessary. If two signals with orthogonal polarization are launched into an ideal fiber they should maintain that orthogonality throughout the fiber. That way by overlapping two signals with orthogonal polarization we can amplify them with one fiber amplifier and separate them again after the amplification.

The setup (see figure 4.11) involves two polarizing beamsplitter cubes (PBC) and one Lefèvre polarization controller. The two signals are overlapped with the first PBC, then coupled into a fiber and sent through the polarization controller and the fiber amplifier. The polarization controller is adjusted in such a way that the two signals coming out of the amplifier are vertically and horizontally polarized respectively so that the signals can be easily separated by using another PBC.

The setup was implemented with the small fiber amplifier and the amplified signals were both checked with a powermeter and with Fabry-Perot cavities to check the spectrum of the beams. When the paddles of the fiber polarization controller were adjusted in the right way more than 99% of the amplified signals came from the corresponding input signals. As long as the current of the fiber amplifier wasn't turned up to more than 0.8 A the output polarization was stable. Turning up the current higher caused fluctuations of the polariza-

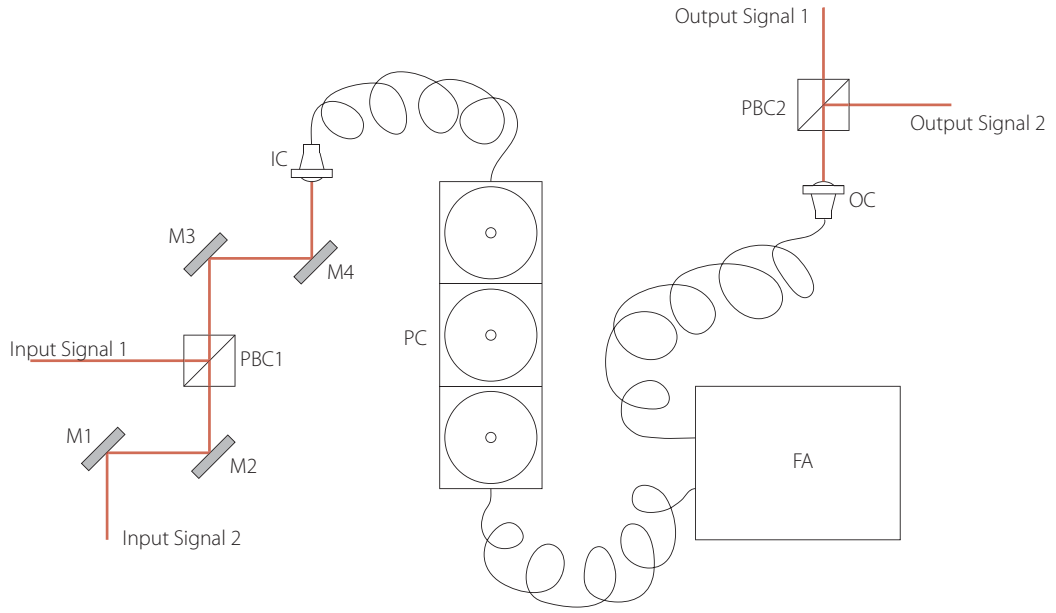

M:	Mirror	IC:	Input Coupler
PBC:	Polarizing Beamsplitter Cube	OC:	Output Coupler
PC:	Fiber Polarization Controller	FA:	Fiber Amplifier

Figure 4.11 Setup for the amplification of two signals with just one fiber amplifier. Adjustment of the polarization controller makes it possible that more than 99% in each of the amplified signals is the same as the corresponding incoming signals.

tion which made it impossible to separate the signals correctly after the fiber amplifier.

This novel way of amplification has two major advantages. The first one is, of course, that only one fiber amplifier is necessary for the amplification of two signals. The second advantage is that the minimum input power (≥ 0.5 mW) is now shared between the two signals. That means that this also provides a way of amplifying signals that otherwise would have been too small for amplification with the fiber amplifiers. The most extreme way of utilizing this

is to use one stronger signal only as a carrier signal that is not longer used after the separation of the two amplified signals and has the sole purpose of providing the minimum input power for the amplifier to prevent any damage that could be caused by spontaneous emission in backward direction.

4.4 Bichromatic Light Setup

4.4.1 Four Frequency Production

As described in section 2.4.6, bichromatic collimation needs two beams containing two frequencies each. One of the beams contains the frequencies $\omega_a \pm \delta + kv$ and is called $+kv$ beam, the other beam contains the frequencies $\omega_a \pm \delta - kv$ and is referred to as $-kv$ beam where ω_a is the frequency of the $2^3S_1 - 2^3P_2$ transition.

Doubly Passed AOM

Both the $+kv$ and the $-kv$ beam can be created with a single, doubly passed acousto optic modulator (AOM). The idea of this so-called 4-ω-AOM has first been proposed by the author of [40] and was first used for experiments with bichromatic light on Rubidium ([41, 42]).

The way this works is illustrated in figure 4.12: a single beam with the frequency of the laser diode ω is incident on the AOM that is driven with an RF frequency $\frac{\delta}{2\pi} = 60$ MHz. Taking the 0 and +1 order deflection from the AOM gives beams with frequencies ω or $\omega + \delta$, respectively. By retroreflecting those two beams they pass the AOM a second time thereby creating two beams

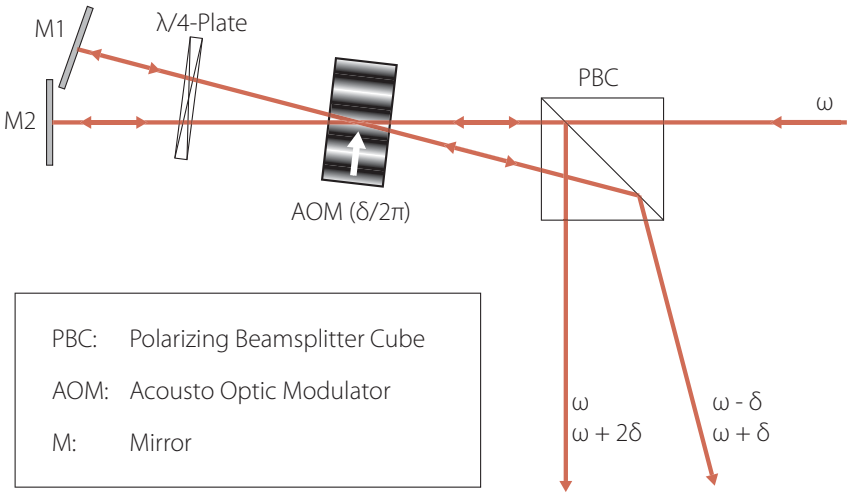

Figure 4.12 Only one AOM is used for producing the two beams containing two frequencies each that are necessary for bichromatic collimation.

containing two frequencies each, one with $\omega - \delta$ and $\omega + \delta$ and the other one with ω and $\omega + 2\delta$. To separate the incoming from the outgoing beams spatially, a $\frac{\lambda}{4}$-plate is used that is passed by the beams twice, and therefore rotates their polarization by 90°. When passing the PBC afterwards the beams are not deflected and can be separately coupled into the input fibers of the fiber amplifiers.

Power Balancing

The model of Bichro assumes that both frequencies in the $+kv$ and $-kv$ beams have equal power. To achieve that, the deflection efficiency of the AOM needs to be adjusted which can be done by changing the RF power driving the AOM and by changing the angle of incidence on the AOM. Whereas the RF power stays constant over time, the position of the AOM has to be readjusted each

time to ensure a correct power balancing. To do so, the AOM is mounted on a six-axes motion stage that allows for 3D translation and tilting. Usually a good power balancing can be achieved by just adjusting the height and the pitch of the AOM.

To check the balancing of the beams, part of the amplified signal after the fiber amplifiers is sent to a Fabry-Perot cavity. One of the mirrors of the cavity is mounted on a PZT and can be scanned by applying a high voltage. As a consequence of the frequency selective properties of a Fabry-Perot cavity [43] only light of certain wavelengths is transmitted and by changing the length of the cavity and detecting the transmitted light with a photodiode a spectrum of the incoming light can be displayed with an oscilloscope. Figure 4.13 shows the signals from the two Fabry-Perot cavities that were recorded with an oscilloscope after adjusting the position of the AOM to get two equally high peaks in each of the signals.

4.4.2 Phase Control

The relative phase between the counterpropagating $+kv$ and $-kv$ beams has a big influence on the magnitude and even the direction of the force since it decides about the timing of the exciting and the deexciting π-pulse. As described in section 2.4.5 the optimal relative phase between the two pulses is $\frac{1}{4}$ of the length of a pulse and with a difference of $\frac{2\delta}{2\pi} = 120$ MHz between the two frequencies in each beam the pulse duration is $T = \left(2 \cdot \frac{2\delta}{2 \cdot 2\pi}\right)^{-1} = 8.3$ ns and the length of a pulse is $c \cdot T = 2.5$ m. The difference in optical pathlength

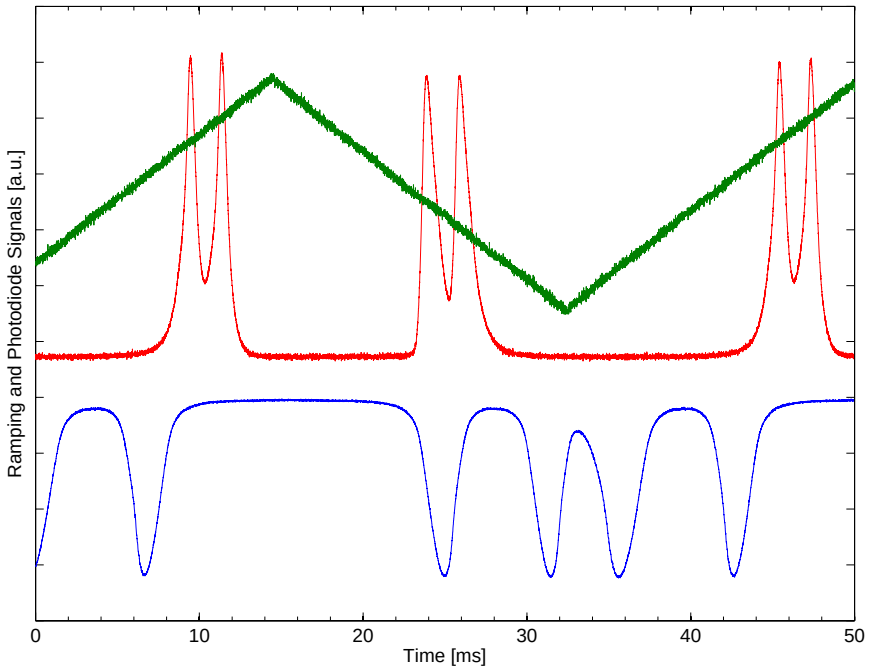

Figure 4.13 Signals from the Fabry-Perot cavities showing the spectrum of the $+kv$ (blue) and $-kv$ (red) beam. The frequency separation between the two peaks is $\frac{2\delta}{2\pi} = 120$ MHz in both signals. As a reference the signal that is applied to the PZTs of the Fabry-Perots is shown in green. Since both peaks have approximately the same height the two frequencies in each of the beams are well balanced.

between the $+kv$ and the $-kv$ line has to be such that the $-kv$ pulse excites the atoms and the deexciting $+kv$ pulse is delayed by $\frac{T}{4}$.

An easy way of changing the optical pathlength without realigning optics is by inserting an additional patchcord of optical fiber between the fiber coupler and the input fiber to one of the FAs. Since according to the manufacturer the length of the fiber is only within $\pm 10\%$ within the specifications and hence a 1 m long fiber has an uncertainty in optical pathlength of ± 1 m$\cdot 0.1 \cdot n = 14.5$ cm

where $n = 1.45$ is the refractive index of the core of a silica single mode fiber from Thorlabs (P3-980A-FC-5) for 1083 nm light. Therefore additional fibers were only used for the coarse adjustment of the phase whereas the fine control was done with a manual delay stage with ~ 32 cm travel range which could change the difference in optical pathlength by up to 64 cm $\equiv \frac{\pi}{2}$ phase delay.

Measurement of the Relative Beat Envelope Phase

To actually measure the relative beat envelope phase between $+kv$ and $-kv$ two fast photodiodes (UDT-InGaAs-100L) were used. To get rid of all the additional phase differences created by the electronics, differences in the length of the BNC cables and difference in pathlength from the output fiber to the photodiodes, we used a setup as drawn in figure 4.14 and took a measurement with the $+kv$ fiber connected to output coupler 1 and $-kv$ to output coupler 2 and then switched the two output fibers to take another measurement and average over both measurements. The signals were recorded with a LeCroy WaveSurfer 434 oscilloscope that was triggered with the RF power driving the 4-ω-AOM.

The data was then analyzed with Mathematica 5 by finding the positions of all minima of the signals and calculating for each minimum in the $-kv$ signal the distance to the next minimum in the $+kv$ signal. This procedure was repeated for five different positions of the phase stage. The results are given in table 4.3.

The change in the relative phase is each time $\sim 25°$ which is in good agree-

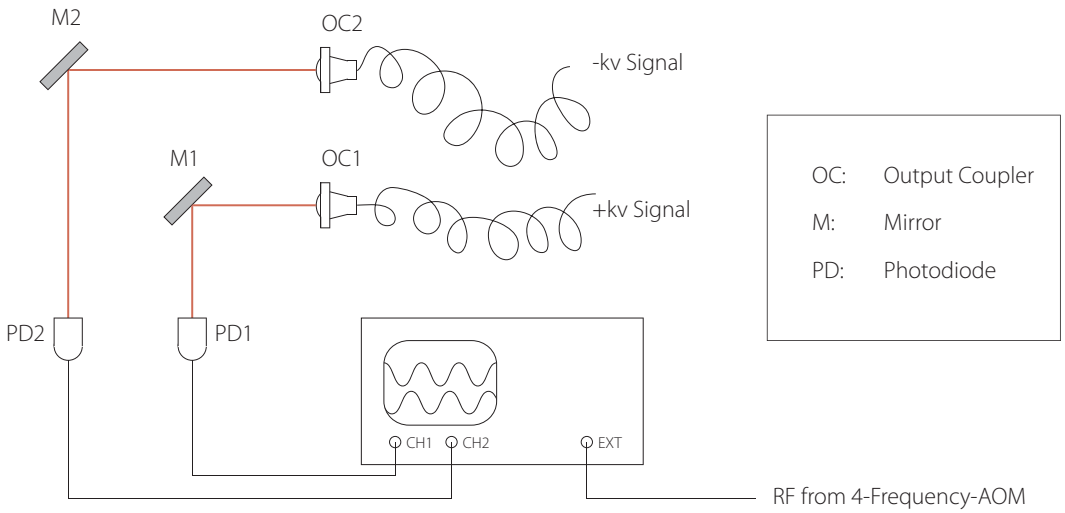

Figure 4.14 Setup for the measurement of the relative phase between the $+kv$ and the $-kv$ signal. The oscilloscope is externally triggered by the RF frequency driving the 4-frequency-AOM. The fibers are switched between OC1 and OC2 to average out effects from different optical pathlengths after the output couplers, effects from the BNC cables, the photodiodes, etc.

ment with the expected value when moving the phase stage by 8.3 cm which gives an additional pathlength of 16.6 cm and therefore a phase difference of $\frac{0.166\ \mathrm{m}}{2.5\ \mathrm{m}} \cdot 360^\circ = 23.9^\circ$. For these measurements the centered position of the stage gave a phase difference between the $+kv$ and the $-kv$ signal of about $270^\circ \equiv -\frac{\pi}{2}$ which is the wrong order of the π-pulses and therefore creates a force in the wrong direction. This was corrected by inserting an additional fiber and moving the phase stage until the collimation signal on the phosphor screen was maximized.

In addition to the relative phase, these measurements also yielded a very precise measurement of the difference between the two frequencies in each beam. By measuring the distance in time between two subsequent minima in

Position phase stage	0 mm	83 mm	166 mm	249 mm	332 mm
$-kv$ at 2	279°	303°	326°	352°	376°
$-kv$ at 1	163°	188°	224°	247°	270°
average	221°	246°	275°	300°	323°

Table 4.3 Measurements of the relative beat envelope phase of the $+kv$ beam with respect to the $-kv$ beam for different positions of the phase stage.

a signal and averaging over all the data taken during the phase measurements, the modulation frequency of the bichro beams could be determined to be $\frac{2\delta}{2\pi} = (119.825 \pm 0.01)$ MHz.

4.4.3 Beam Expansion and Polarization Control

Telescoping the Beams

The output fibers of the fiber amplifiers are plugged into Thorlabs output couplers that roughly collimate the beam. Since the collimation isn't good enough to guarantee that the intensity within the beam stays almost constant over a long distance, and since the beam size after the output couplers is too small (less than 1 mm beam waist) one spherical and one cylindrical telescope are used for beam expansion and collimation. By expanding the beam in one direction more than in the other the region where the atoms interact with the light can be extended without loosing too much of the intensity.

The intensity profiles were taken with a 100 μm slit that was mounted on a Newport powermeter and scanned over the beam. The data was fitted using Origin 7.9 with a Gaussian profile. Using the definition of the spot size given in [44], i.e. the halfwidth at the $\frac{1}{e^2}$ intensity level, we got the beam sizes listed

in table 4.4 and divergence angles smaller than 10^{-5} rad.

	$+kv$ spot size [mm]	$-kv$ spot size [mm]
horizontal	1.9	6.2
vertical	2.1	7.0

Table 4.4 Fitted beamsizes of the bichromatic beams. The numbers give the halfwidth at the $\frac{1}{e^2}$ intensity level.

Optical Pumping

The description of the bichromatic force given in section 2.4 relies on the model of a two-level atom. Since this is just an idealization and never true for any real atom, it is important to make sure that the influences of other levels are negligible. Since the detuning of the modulated $+kv$ and $-kv$ beams from resonance with the $2^3S_1 - 2^3P_2$ transition is only 30 MHz and the transition $2^3S_1 - 2^3P_1$ that is closest to that is almost 2.3 GHz higher (see He* level diagram figure 3.1) the contribution of other transitions can be disregarded.

Nevertheless, both involved levels 2^3S_1 and 2^3P_2 have $J > 0$ and therefore split into several magnetic sublevels with different values for m_J (see figure 4.15). Since $\sigma^{\pm}$ light drives only transitions with $\Delta m_J = \pm 1$ the use of circularly polarized light gives control over the sublevels that are involved. Using σ^+ light optically pumps the atoms in a way that effectively only the $2^3S_1;\ m_J = 1 \leftrightarrow 2^3P_2;\ m_J = 2$ transition is involved. On the other hand the effective two-level atom is formed by the $2^3S_1;\ m_J = -1 \leftrightarrow 2^3P_2;\ m_J = -2$ transition when σ^- light is used for the optical pumping.

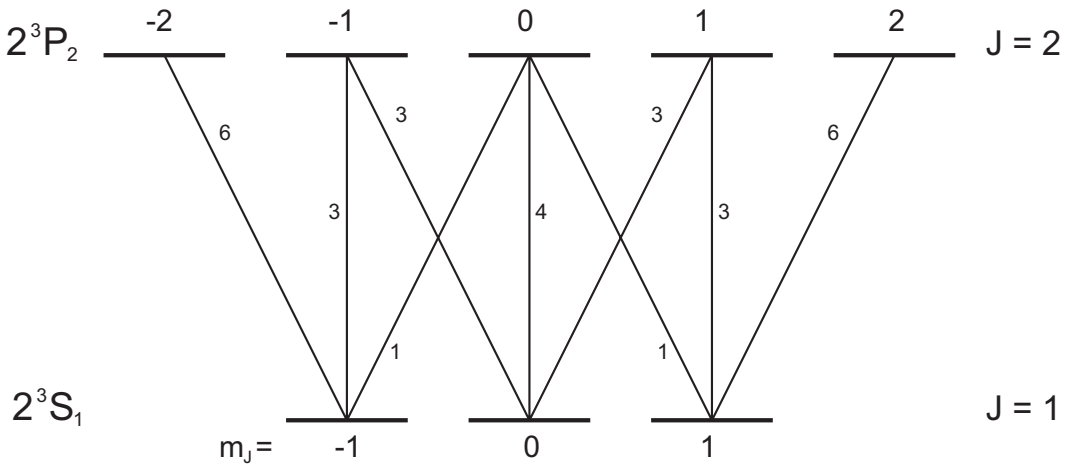

Figure 4.15 Sublevels of the 2^3S_1 and the 2^3P_2 level of He*. The relative transition strengths are also given in the drawing.

In the interaction region the polarization must be the same for both Bichro beams (either σ^+ or σ^-) to be able to optically pump the atoms. Since the beams are counterpropagating when they interact with the atoms they need to have opposite helicity [40]. That is achieved by having $\lambda/4$ plates before and after each interaction region that have their fast axes aligned to each other. The waveplate after the interaction region is passed twice, thereby switching the circular polarization of the light. Before passing the first waveplate the $+kv$ and the $-kv$ beam are linearly polarized and orthogonal to each other. This setup (see figure 4.16) makes sure that in each interaction region is passed by two beams with the same circular polarization.

4.4.4 Setup for 2D Bichromatic Collimation

Each one-directional bichromatic push needs $+kv$ light and $-kv$ light coming from opposite directions and with the $-kv$ pulses ahead by $\phi = \frac{\pi}{2}$. That

means that altogether four interaction regions are necessary to collimate in two dimensions. The two interaction regions for each dimensions are sharing the same light by retroreflecting the $+kv$ and $-kv$ beam in such a way that the beams overlap (see figure 4.16). To get the relative phase right it is important that the distance the light travels between the two interaction regions corresponds to a phase of $(2n-1)\,\pi,\ n \in \mathbb{N}$. In our setup the length is chosen to be 125 cm which corresponds to a phase delay of π. By doing so, the $-kv$ beam is in each interaction region ahead by a quarter of a beat if the phase is adjusted properly (see section 4.4.2).

4.5 Optical Molasses

The bichromatic force collimates the beam to a final transverse velocity of $\sim 9\ {}^{\mathrm{m}}/_{\mathrm{s}}$ [4, 34]. For further collimation an optical molasses stage is implemented right after the four collimation regions for bichromatic collimation. Part of the $-kv$ beam is send through an AOM that is driven with a frequency of 82 MHz. That shifts the two frequencies in the beam to $\omega_a - 2\pi \cdot 8$ MHz and $\omega_a + 2\pi \cdot 112$ MHz respectively. The latter frequency component is too far detuned from atomic resonance to have a significant influence on the atoms. The other frequency component improves the collimation of the atoms in an optical molasses configuration. The detuning of $\delta = -2\pi \cdot 8$ MHz is chosen to capture most of the atoms precooled by the bichromatic force (because $\frac{v_t}{\lambda} \cong 9$ MHz, v_t is the transverse velocity of the atomic beam after bichromatic collimation). The intensity of the molasses beam can be adjusted with one of

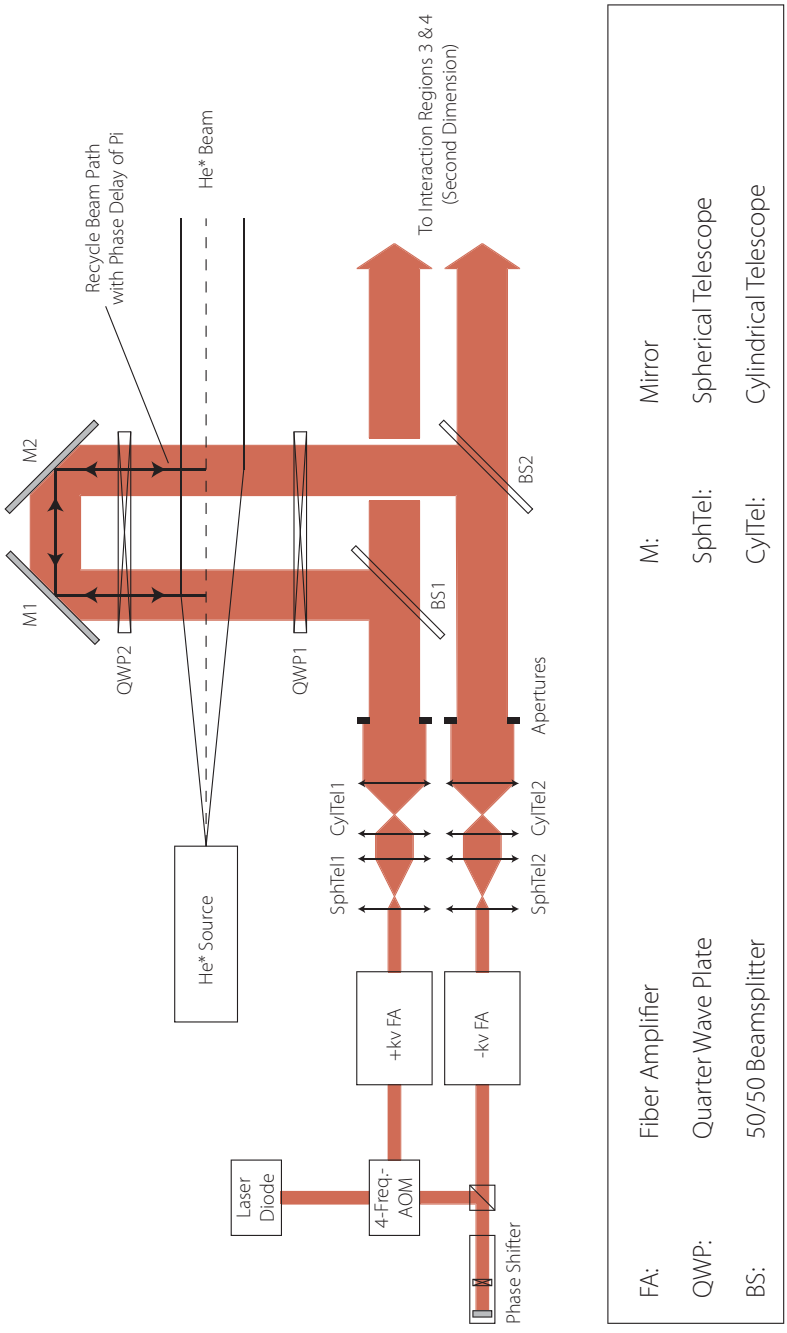

Figure 4.16 Diagram of the interaction regions for bichromatic collimation in two dimensions. Four separate interaction regions are necessary that all have to fulfill conditions for the relative phase between the counterpropagating $+kv$ and $-kv$ beam. The diagram is not drawn to scale.

the 1 W fiber amplifiers and is adjusted in such a way that the peak flux that is checked with the SSD is maximized.

The final velocity of that molasses configuration is $3.5 - 4$ m/s [4]. With a transversal velocity of 1000 m/s that still corresponds to a divergence angle of 7.5 mrad FWHM. Since this divergence does not only reduce the peak flux at the place where the sample is exposed, but also leads to larger aberrations with a standing wave light mask (see section 5.4.1), a second molasses stage is planned. By choosing parameters close to those of ordinary Doppler molasses, most of the atoms from the first molasses stage could be captured and their final velocity could reduced close to the Doppler velocity $v_D \approx 0.3$ m/s.

4.6 Light Mask Setup

Attempts to pattern a wafer using a standing wave light mask have thus far been unsuccessful. Most of these attempts were made with the old beamline. Part of the problem certainly was that the atomic beam is not well enough collimated and that the beamwaists of the laser beam for the light mask was too big for the divergence of the atomic beam. Another reason could be that with the old beamline, no accurate positioning of the sample in the atomic beam was possible to compensate for changes in the collimation alignment. The latter problem is solved with the new setup for the beamline, the former one can be significantly improved by inserting another molasses stage (see section 4.5). Since the implementation of a rudimentary light mask will be the next step after getting control over the exposure and etching times, the setup

that basically resembles the one used with the old beamline is described here.

The light for the light mask comes from the secondary output of the extended cavity of the laser (see figure 4.3). It is frequency shifted by an AOM to get the desired detuning, then amplified with the small 1 W fiber amplifier as a secondary signal as described in section 4.3.3. The amplified beam is then extended with a telescope to get the desired beamwaist. The smaller the size of the beam waist the smaller are aberrations of the standing wave light mask (cf. section 5.4.1). Two translation stages are used for positioning the beam so that the height equals the height of the atomic beam and the wafer is positioned so that half the beam can pass in front of the wafer. A mirror is mounted on the sample holder that retroreflects the light mask beam thereby creating a standing wave.

Chapter 5

Neutral Atom Lithography

5.1 Atomic Nanofabrication

About 15 years ago people started using the techniques and the knowledge that arose from research in laser cooling and atomic physics to create structures on the nanometer scale by using beams of neutral atoms. Starting with the very first experiment that used a beam of sodium atoms that were patterned with a standing wave light field and deposited on a surface [45] a research field called atomic nanofabrication (ANF) [5] developed.

In principle one can distinguish between two main branches in ANF: the first one creates the structures by directly depositing atoms on a surface. This direct deposition technique has been successfully demonstrated with a wide variety of different atoms, for example sodium [45], aluminum [46], or chromium [47]. The advantage of this direct deposition (DD) technique is that no further processing is necessary. On the other hand atomic sources with high atomic flux are necessary because, depending on the desired structure height, several atomic layers have to be deposited.

The second branch of ANF resembles the technology used in today's microchip fabrication where other steps have to follow the exposure to actually create the structures. In this so-called neutral atom lithography (NAL) the atoms constituting the atomic beam are not forming the resulting structures. They are just used to either damage a resist layer locally or to modify other substances to form a resist at certain positions. By using an etching solution that acts differently on the damaged / modified parts than on the rest of the sample, it is possible to transfer the pattern in an underlying layer.

Several combinations of resists and surfaces have been used together with different kinds of exposing atoms. The most popular combinations of resists and surfaces are self-assembled monolayers (SAM) of alkanethiols on a gold surface and alkylsiloxane SAMs on SiO_2. For both combinations exposures were done with beams of alkali atoms [48, 49] as well as with beams of metastable rare gases [50, 51]. Metastable noble gas atoms carry internal energies between 8 eV for Xe* and 20 eV for He*. Since these are huge amounts of energies on the atomic level, and since that energy is released when the atoms hit a surface, metastable rare gas atoms are sometimes referred to as *nature's nanogrenades* and are especially useful for damaging resists using relatively small flux numbers.

Besides those experiments that use the atomic beams to damage a resist layer, it is also possible to modify molecules in a way that they form a resist for an underlying layer. A beam of Ar* in the presence of dilute vapors of trimethylpentaphenyltrisiloxane can be used for such an approach [52]. Since

those vapors are the main component of the diffusion pump oil used in that experiment, that technique is also referred to as *contamination lithography*.

One advantage of NAL techniques compared to DD are that much lower flux numbers are necessary and still the structure height can be significant since it depends on the etching technique and the thickness of the substrate and not on the amount of atoms hitting the sample as long as it is enough to damage the resist layer locally. The method is also much more easily transferable to different substrates since only an appropriate combination of resist and etching solution has to be found.

For both NAL and DD the atomic beam has to be patterned to create the desired structures on the nanometer scale. The use of a material mask (a simple mesh for example) is the easiest way of doing that but of course that implies that other processes are available to create such a mask. Therefore more flexible ways of steering the atoms have been developed. The use of the intrinsic magnetic dipole moment of the atoms is possible but requires very high control over the magnetic fields that create the mask, especially if the structures are getting smaller and smaller. The most flexible and accurate way of creating small structures in ANF without the use of a material mask so far is the use of light for steering the atoms. The working principle of a simple standing wave light mask is described in section 5.4, for more complicated light masks a good overview can be found in [53].

In our lab we use gold-coated silicon wafers for the experiments. They are protected with a nonanethiol SAM and damaged by metastable helium. So

far, lithography experiments have been done with a mechanical mask [6] (see also section 6.2.2). Since then the vacuum system and the optical setup have been redesigned to allow for more efficient and reproducible exposing of the wafers. The next step is the implementation of a light mask (see section 5.4) for the patterning of the He* beam. To do so we have already implemented the necessary preconditions in our current setup (cf. sections 4.3.3 and 4.6).

5.2 Self-Assembled Monolayers as a Resist

The resist layer in our experiment is formed by a self-assembled monolayer (SAM) of alkanethiols. Alkanethiols are molecules with an alkane chain and an -SH head group and have the chemical formula $CH_3\,(CH_3)_{n-1}\,SH$. In our experiment we usually use nonanethiol ($n = 9$) and sometimes dodecanethiol ($n = 12$). Those molecules have the property that they assemble themselves in a single layer, and a lot of research on their properties has been done over the last years. A good review article on those and similar SAMs can be found in [54].

Of special interest for our research is the building of a monolayer on a gold surface. The molecules preferably adsorb to the {111} surface of gold. The part connecting to the gold atoms is the -SH group of the molecules. The chemical process describing the adsorption is

$$\text{R-SH} + \text{Au}_n^0 \rightarrow \text{RS}^- - \text{Au}^+ + \frac{1}{2}\text{H}_2 + \text{Au}_{n-1}^0 \tag{5.1}$$

Since the energy of this bond is $\sim 200\ {}^{\text{kJ}}/_{\text{mol}}$ [55], it is relatively stable.

When the nonanethiol is dissolved in ethanol and a gold-coated silicon wafer is put into that solution, the SAM starts to form on the coated surface. After just a few minutes already 80% - 90% of the surface is covered with nonanethiol molecules [54], but it takes 15 to 24 hours until a good resist has formed. Within that time the chains of the molecules all align themselves in an angle of $\sim 30^{\circ}$ to the surface normal. The thickness of the formed SAM is ~ 1 nm.

The evaporation of a very thin gold layer ($\sim 20 - 30$ nm) on a silicon surface doesn't give a smooth gold surface. Instead, small gold grains are built up similar to small amount of water forming drops on a smooth surface. This effect can be reduced by using another substrate underneath the gold layer. Muscovite mica has been used instead of silicon for example and was found to give a smoother gold surface [56]. However, since defect formation within the SAM also occurs on single-crystal atomically flat surfaces with defect-free regions of only ~ 20 nm, that does not eliminate all the defects in the SAM.

When a metastable helium atom hits the SAM, it damages the molecules in such a way that the protection against the etching solution becomes less effective. Due to the high internal energy of 20 eV, the doses for damaging the SAM don't have to be very high. In an experiment with dodecanethiol it was found that the necessary dosage is a few times 10^{13} $^{\text{atoms}}/_{\text{mm}^2}$ to sufficiently damage the SAM for good etching results [57]. And since secondary electrons with energies on the scale of the internal energy of He* have a mean free path in the substrate of only a few ångströms the energy deposit and therefore the damage of the SAM is well localized.

There are still a lot of things in the behaviour of alkanethiols that aren't very well understood, e.g. the self-assembling process and how to influence it. But since there is still a lot of research going on, it might very well be that some of the techniques we used for doing the chemistry can be replaced with other procedures that are better suited for ANF. For example the authors of [58] claim that when using a mixture of water and Triton X-100 instead of ethanol for dissolving the alkanethiols, a more uniform and therefore better protecting SAM is formed on the surface of the gold-coated wafers.

5.3 Experimental Procedure

The wafer preparation and the etching both involve chemical substances. When dealing with hazardous chemicals the work is done under a fume hood with heavy rubber gloves. The area where the chemistry and the analysis of the exposed wafers is done is shielded from the rest of the lab with plastic shielding to keep it clean. On top of the shielded area a fan is filtering the air before it gets in.

5.3.1 Wafer Preparation

The wafers used for the lithography experiments are 2" silicon wafers from Montco Silicon Technologies. They are coated with a 50 Å layer of chromium as a primer and a 200 Å layer of gold on top of it. More details on the wafers can be found in table 5.1. If not a whole wafer is used for one exposure the wafers can be divided into smaller pieces by applying pressure with the sharp

edge of a piece of stainless steel.

It is very important to have a clean gold surface to get a good SAM on the wafer. Therefore the wafer is first rinsed with acetone and ethanol and then further cleaned with a mixture of sulfuric acid (H_2SO_4) and a 30% hydrogen peroxide (H_2O_2) solution (50% in volume each). This so-called piranha solution dissolves organic material and has to be treated with great care since it is extremely corrosive. The wafers stay in that solution for several minutes and are rinsed with pure ethanol afterwards to get rid of any residues from the piranha solution.

Material	Silicon
Growth Method	CZ
Diameter	2" (50.8 mm)
Type	N/Phos
Orientation	$\langle 100 \rangle$
Resistivity	$0 - 100\ \Omega$ cm
Thickness	$256 - 305\ \mu$m
Grade	Prime
Front Surface	Polished
Back Surface	Etched
Coating	50 Å Cr / 200 Å Au, evaporated

Table 5.1 Properties of the silicon wafers used for the lithography experiments.

In the experiments we use nonanethiol (1-Nonanethiol, 95% from Aldrich) for the formation of the SAM. It is dissolved with a concentration of $1.0 \cdot 10^{-3}$ $^{\mathrm{mol}}/_{\mathrm{l}}$ in pure ethanol (200 Proof from Pharmco-AAPER). When putting the wafers into that solution for 24 hours the nonanethiol molecules assemble

themselves in a monolayer on the gold surface (see section 5.2). Since their hydrophobic tail is sticking up, the SAM is able to protect the wafer from water based etching solutions. Each wafer is put separately in $\sim$ 100 ml of solution. A lab scale with 2 mg accuracy is used to determine the amount of nonanethiol. Afterwards the correct amount of ethanol is added.

When taking the wafer out of the solution it is rinsed again in pure ethanol to prevent nonanethiol molecules from piling up in the spots the ethanol evaporates last. After the evaporation of remaining ethanol the wafer is prepared for exposure.

5.3.2 Masking and Exposure

Right after the wafer has been taken out of the nonanethiol solution, it is mounted on a sample holder than can be attached to the motorized stages in the vacuum system. The wafer is held in place with a couple of screws and washers that are tightened just enough to not let the wafer fall off. A millimeter grid printed on a transparency is used for marking the positiong of the wafer relative to the sample holder. That helps determining the positions where the wafer should be exposed and with those positions also marked on the grid it is easy to put the transparency over the wafer after the etching to compare the results with the intended layout.

For doing exposures with a mechanical mask, the mask (usually a fine mesh) is put right on top of the prepared wafer and also held by screws. The sample holder with the wafer is then attached to the motorized stage at the

back of the beamline. For the case of using a light mask, a mirror has to be attached to the sample holder and the light mask beam has to be aligned as described in section 4.6. After that the quick access doors have to be closed again and the system has to be pumped down slowly with the sorption pumps to minimize any damage to the SAM by fast pressure changes. A schematic diagram of the exposure and etching procedure is shown in figure 5.1.

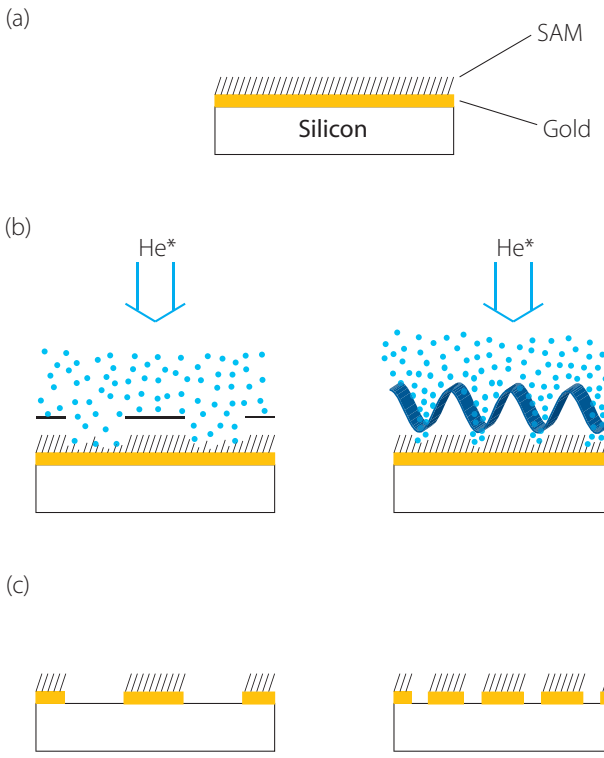

Figure 5.1 Schematic Diagram of the Exposure and Etching Process.
(a) A SAM is used as a resist for the gold-coated silicon wafer.
(b) The masking is done with either a material mask that blocks atoms at certain points or a light mask that redirects the atoms to get a spatially varying flux.
(c) After the etching the gold is removed at places where the sample was exposed to sufficient flux of metastables.

The program that controls the stage (see C) can be used for scheduling multiple exposures. The stages are then moved to the different positions corresponding to the spots on the wafer that are to be exposed and stay there for the desired exposure time. After the last exposure is over, the lithography chamber can be brought up to air slowly (nitrogen gas is used to keep the system as clean as possible) and the sample holder can be taken out of the system.

5.3.3 Etching

When the metastable helium atoms hit the SAM they locally remove small parts of the long chainlike molecule, namely H^+ and $CH_x{}^+$ ions [59]. Thus the hydrophobicity of the damaged molecules is reduced so that an etching solution that acts selectively on the damaged parts of the SAM can be used together with alkanethiol SAMs in lithography experiments.

The water based etching solution we use was developed by the authors of [60]. The solution is $S_2O_3{}^{2-}$/ferri/ferrocyanide based and contains the constituting chemicals in the concentrations given in table 5.2. The potassium thiosulfate (pure) used is from Riedel-de Haën, the potassium ferricyanide (99+%) and the potassium ferrocyanide (99%) are from Sigma-Aldrich and the potassium hydroxide is from Fisher Scientific.

The weight of the chemicals is determined with a lab scale of accuracy 2 mg. The constituents are mixed with a magnetic stirrer until all chemicals are dissolved in the solution and the color is bright yellow. The wafer is put

Name	Chemical Formula	c [mol/l]	Amount
Potassium Hydroxide	KOH	1	15.586 g
Potassium Thiosulfate	$K_2S_2O_3$	0.1	4.758 g
Potassium Ferricyanide (III)	$K_3Fe(CN)_6$	0.01	0.823 g
Potassium Ferrocyanide (II) Trihydrate	$K_4Fe(CN)_6 \cdot 3\,H_2O$	0.001	0.106 g
Distilled Water	H_2O	solvent	250 ml

Table 5.2 Chemicals used for the chemical etching solutions. The amount given in the last column is for 250 ml of etching solution. Potassium hydroxide naturally contains 10-15% water. For the weight calculation a water content of 10% of the weight is assumed.

into the etching solution for $5 - 10$ minutes. During that time the magnetic stirrer is still on at a low speed ($100 - 300$ rpm) to get a more homogeneous etching process. To avoid direct contact of the stirrer with the wafer, a large beaker is used and the stirrer and the wafer are positioned on opposite sides within the beaker.

The etching of the gold happens in an electrochemical process consisting of (1) metal oxidation (dissolution)

$$Au^0 + 2{S_2O_3}^{2-} = Au\,{(S_2O_3)_2}^{3-} + e^- \tag{5.2a}$$

or

$$Au^0 + 2OH^- = Au\,{(OH)_2}^- + e^-$$

$$Au\,{(OH)_2}^- + 2{S_2O_3}^{2-} = Au\,{(S_2O_3)_2}^{3-} + 2OH^- \tag{5.2b}$$

and (2) reduction of an oxidizer

$$Fe\,{(CN)_6}^{3-} + e^- = Fe\,{(CN)_6}^{4-} \tag{5.3}$$

The etching solution also works without ferrocyanide, but with it the defects formed in the part covered by the SAM are significantly reduced.

After the etching the wafer is taken out of the etching solution and rinsed with distilled water and acetone to get rid of residues of the etching solution and the SAM.

5.3.4 Analysis

A rough analysis of the exposure and the etching can be done by just looking at the sample and distinguish between areas with gold and areas without gold. To facilitate that, one of the atomic beam defining slits at the entrance of the spherical cube (see section 3.3.3) is covered with a coarse mesh ($\sim$ 1 mm distance between two wires), so that the unexposed areas behind wires can even be seen by bare eye. An example for that is shown on the picture in figure 5.2.

For analyzing smaller structures some sort of microscope is needed. We use a Quesant Instrument Corporation atomic force microscope (AFM) model Q-Scope$^{\mathrm{TM}}$ 350. The scanning of the sample is done by rastering a sharp, $15 - 20$ μm long silicon tip that sits at the end of a several hundred μm long silicon cantilever across the surface. The lateral movement of the tip is done with PZTs. The AFM can be used both in contact mode and intermittent contact mode. The latter one gives usually better resolution and is therefore used for the scans of the exposed samples. In this mode the cantilever is brought to oscillation close to its resonance frequency ($\sim 100 - 200$ kHz). The

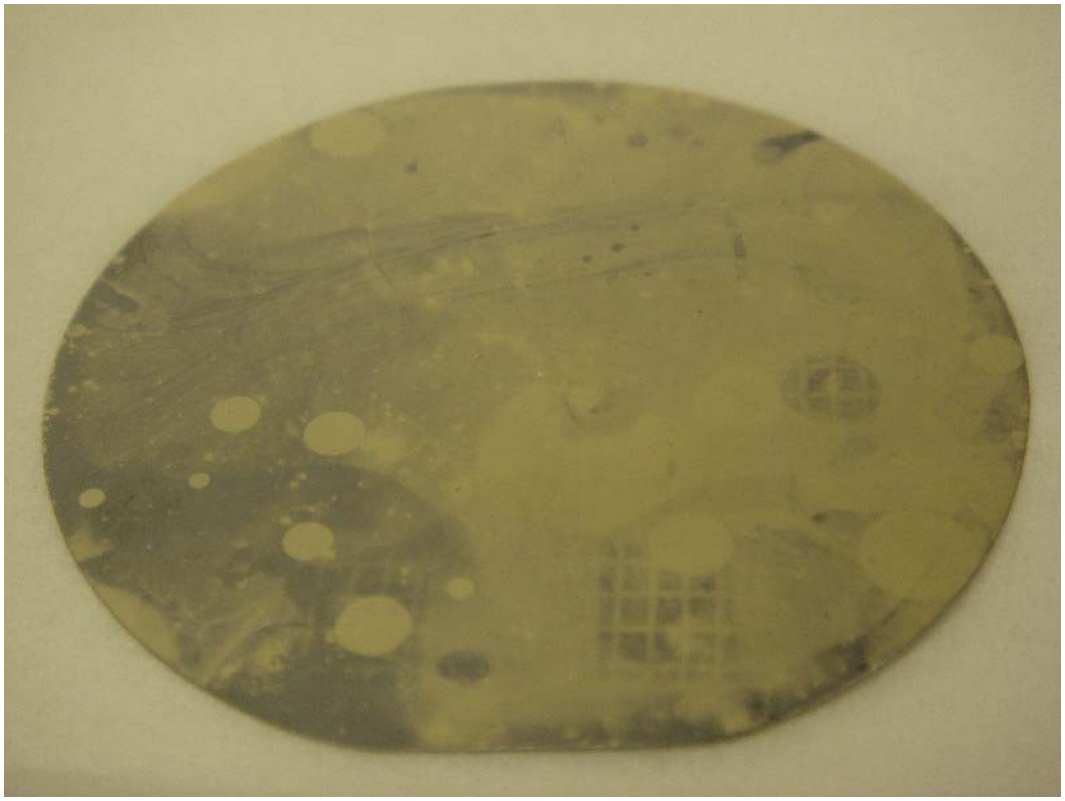

Figure 5.2 Picture of an exposed wafer. Three spots can be seen where the exposure dose was high enough and therefore the big mesh pattern can be seen. The inhomogeneities are mainly artifacts of the very rudimentary etching procedure.

amplitude of the oscillation is monitored with a laser beam that is deflected off the back of the cantilever. If the tip is brought close to the surface, the oscillation is damped. By adjusting the height of the tip with a PZT tube, the damping is held constant at around 50% by a feedback loop. That way the tip follows the height of the surface structures.

The Quesant AFM has another feature, called Broadband mode. In this mode the error signal from the feedback loop that controls the height of the tip

is calibrated and added to the height value of the tip. This allows for better scanning results even with increased scanning speeds. Yet the resolution of this method is still limited by uncertainties in the error signal calibration curve. Despite all uncertainties the resolution of the AFM is on the sub-nanometer range, given a slow scanning speed and a low level of external vibrations.

The software of the AFM has some features for analyzing the scans. Several tilt removal algorithms are implemented to subtract effects arising from an overall curvature or slope of the sample. The scans shown in section 6.2.2 are all processed with a *Parabolic Line by Line* tilt removing algorithm that fits each scanned line with a polynomial of order two and subtracts the result from the image. The software also allows to show the distribution of height values in a histogram which especially helps to see the difference between exposed and unexposed regions. In addition a camera is mounted on top of the AFM that shows a magnified top view of the cantilever tip and the underlying sample. That way pictures of the sample as seen by a light microscope can be recorded.

5.4 Standing Wave Light Mask

The simplest form of a light mask is a standing wave. Calculations and numerical simulations for a blue-detuned (detuning $\delta = \omega - \omega_a > 0$) near-resonant light field have been done for that case [61, 62, 63]. In this section a short summary shall be given, further details can be found in the given references.

The force acting on the atoms in the standing wave light field is the conservative dipole force (see section 2.3). For a low light intensity and/or a

large detuning from atomic resonance the potential U creating the dipole force $F = -\nabla U$ is given by (Eq. (2.16))

$$U(x,y,z) = \frac{\hbar\Omega^2}{4\delta} = \frac{\hbar\gamma^2}{8\delta}\frac{I(x,y,z)}{I_S} \tag{5.4}$$

That result can be generalized for saturation effects that occur when the intensity of the light field is higher and/or the detuning is smaller. Assuming that the atoms are moving slowly enough so that the process can be considered adiabatic but fast enough so that spontaneous emission can be neglected for the time the atoms are travelling through the light mask, the generalized potential creating the dipole force is given by [64]

$$U(x,y,z) = \frac{\hbar\delta}{2}\ln\left[1 + \frac{I(x,y,z)}{I_S}\frac{\gamma^2}{\gamma^2 + 4\delta^2}\right] \tag{5.5}$$

In the case of a standing wave with light of wavelength $\lambda = \frac{2\pi}{k}$ we have an intensity distribution of (laser beams forming the standing wave are along x-direction, atoms moving along z-direction)

$$I(x,y,z) = I_0 g(z)\sin^2 kx \tag{5.6}$$

with $g(z)$ being the laser beam profile along the z-axis and I_0 being the maximum intensity in the standing wave.

We assume that forces in y-direction can be neglected and therefore end up with two differential equation determining the motion of the atoms

$$\ddot{x} + \frac{1}{m}\frac{\partial U(x,z)}{\partial x} = 0 \tag{5.7a}$$

$$\ddot{z} + \frac{1}{m}\frac{\partial U(x,z)}{\partial z} = 0 \tag{5.7b}$$

Using the conservation of energy, these two equations can be combined and by eliminating time we get a single differential equation that expresses x in terms of z [61]

$$\frac{\mathrm{d}}{\mathrm{d}z}\left[\left(1-\frac{U\left(x,z\right)}{E_0}\right)^{\frac{1}{2}}\left(1+x'^2\right)^{-\frac{1}{2}}x'\right] + \frac{1}{2E_0}\left(1-\frac{U\left(x,z\right)}{E_0}\right)^{-\frac{1}{2}}\left(1+x'^2\right)^{\frac{1}{2}}\frac{\partial U\left(x,z\right)}{\partial x}=0 \quad (5.8)$$

where $x'=\frac{\mathrm{d}x}{\mathrm{d}z}$ and E_0 is the total energy of the atom, i.e. its kinetic energy before entering the light field.

Eq. (5.8) can be solved numerically. However, to get a little more insight, we want to look at what happens to the equation in the paraxial approximation limit, i.e. we consider $U\left(x,z\right)\ll E_0$, $x'\ll 1$ and $kx\ll 1$. Using these approximations and plugging Eqs. (5.5) & (5.6) in Eq. (5.8) we get

$$x''+q^2g\left(z\right)x=0 \quad (5.9)$$

where

$$q^2\equiv\frac{\hbar\delta}{2E_0}\frac{I_0}{I_S}\frac{\gamma^2}{\gamma^2+4\delta}k^2 \quad (5.10)$$

For a Gaussian laser beam we have $g\left(z\right)=\exp\left(-2z^2/{\sigma_z}^2\right)$ and by replacing z by the dimensionless quantity $Z\equiv z/\sigma_z$ we get

$$x''+a\exp\left(-2Z^2\right)x=0 \quad (5.11)$$

with

$$a\equiv{\sigma_z}^2q^2=\frac{\hbar\delta}{2E_0}\frac{I_0}{I_S}\frac{\gamma^2}{\gamma^2+4\delta}k^2{\sigma_z}^2 \quad (5.12)$$

This equation has to be solved numerically. One interesting solution is the situation where the atoms are focussed to the center of the beam since this configuration is easier to align than others because of its symmetry. For that case a was determined to be 5.37. By expressing the peak intensity I_0 by the power of the incident traveling laser beam P_0

$$I_0 = \frac{8P_0}{\pi {\sigma_z}^2} \tag{5.13}$$

we see that the laser power that is necessary for focussing the atoms to the center of the standing wave is independent of the beamwaist σ_z and for a large detuning ($\delta \gg \gamma$) we get

$$P = 5.37\frac{\pi E_0 I_S \delta}{\hbar \gamma^2 k^2} \tag{5.14}$$

For the $2^3S_1 - 2^3P_2$ transition in helium that gives a power of

$$P \approx 1.629 \ {}^{\mu\mathrm{W}}/_{\mathrm{MHz}} \cdot \delta \tag{5.15}$$

so the necessary power for the light mask is really small.

5.4.1 Aberrations

There are several contributing factors that can limit the resolution of any light mask technique. The first one is *diffraction* effects because the wavelike nature of the atomic beam with the de Broglie wavelength as the characteristic quantity can't be neglected. The second factor is *chromatic aberration* whereas in this case the term is used to describe the change in the focal length due to the longitudinal velocity spread of the atomic beam. Numerical calculations

show, however, that this effect is rather small compared to others even for atomic beams with a thermal velocity spread, i.e. the spread is on the order of the average longitudinal velocity [61]. Another factor is *spherical aberration* which results from higher order terms in the equation of motion for the atoms that have been neglected in the paraxial approach done here. And as a last effect, any *divergence* of the atomic beam limits the resolution that can be achieved. Having a beam with angular spread (FWHM) 2θ, a geometrical optics approach for thin lenses gives a broadening of the created structures on the order of $\Delta x \approx f \cdot \theta$ [5]. Since f is often chosen in a way that it equals the beam waist of the standing wave light field σ_z it is important to keep both the laser beam waist and the divergence of the atomic beam as small as possible.

Chapter 6

Results

6.1 Imaging the Atomic Beam

To get reproducable results in the lithography experiments it is important to know the parameters defining the He* beam. The alignment of the collimation is important so that the beam hits the back of the beamline as centrally as possible so that the full travel range of the motorized stages can be used. The flux at the position of the sample defines the dosage of He* atoms that damages the resist layer. And to eventually switch to a light mask in the setup, the divergence of the beam has to be known to get an estimate of the minimum feature size arising from aberrations due to the transverse velocity component of the atoms.

6.1.1 MCP/Phosphor Screen

When doing the alignment of the laser collimation optics, two goals have to be achieved. Firstly, the different collimation stages (bichromatic collimation and optical molasses and in the near future probably another molasses stage)

have to be aligned with respect to each other so that they all collimate atoms in the same direction. And secondly, the beam has to be collimated in a direction that is as collinear with the beamline as possible. Both goals require a detector that reacts fast to changes in the alignment and covers a big part of the angular spread of atoms coming from the source. Both requirements are met by the MCP/Phosphor Screen Combination used in our setup (see section 3.4.1). The first detector is 25 cm away from the source and has a diameter of 25 mm thereby covering a detection angle of 100 mrad. The image of the phosphor screen is recorded with a CCD camera and displayed in real-time on a computer screen. Screenshots can be taken and saved as bitmap files that can afterwards be analyzed in more detail. Several of those screenshots are shown in figure 6.1.

The second MCP/Phosphor Screen is mounted in the spherical cube at the end of the beamline. It is used for aligning the beam defining slits at the entrance to the cube to the atomic beam. That way only the part of the atomic beam with the highest flux exposes the sample while everything else coming from the source is blocked, thereby protecting the rest of the wafer until it is moved to a different position for the next exposure.

6.1.2 Flux Measurements

To get actual numbers for the atomic beam flux the SSDs have to be used. With the conversion factors given in table 3.1 the measured currents can be converted to the flux of He* atoms. The SSD detects the current produced by

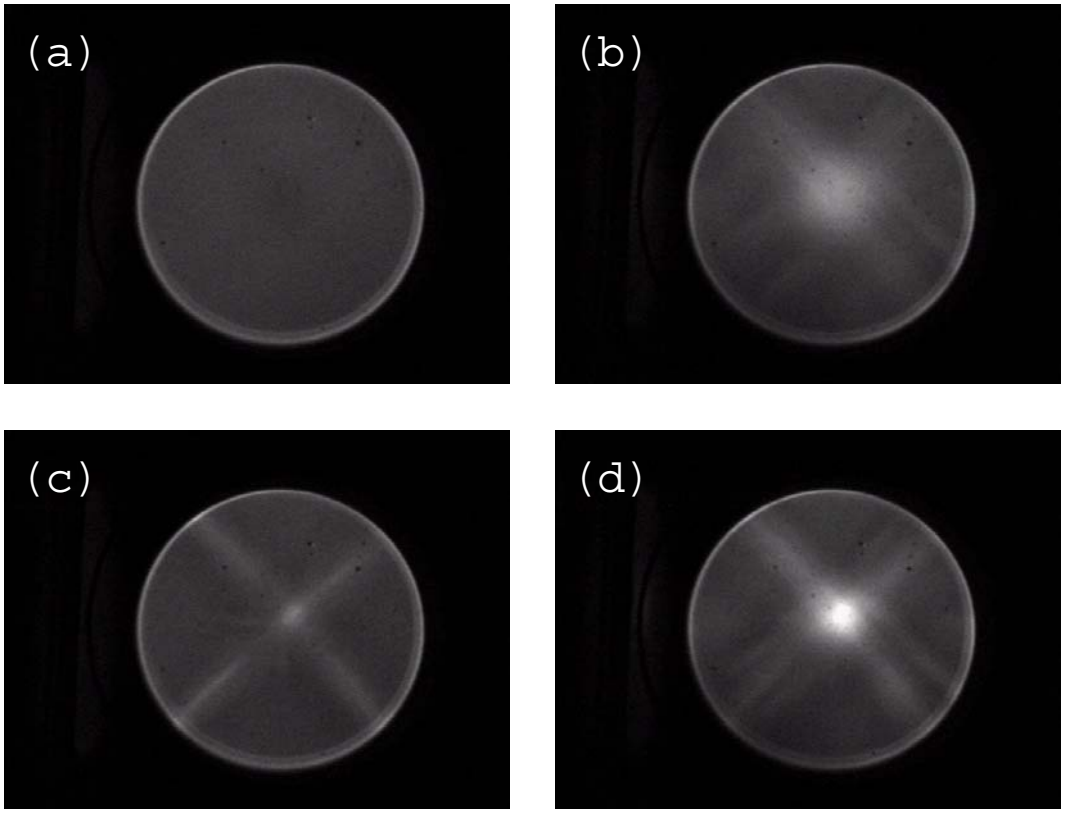

Figure 6.1 Several images recorded with a CCD camera looking at the MCP/Phosphor Screen.
(a) Uncollimated beam coming from the source.
(b) Beam collimated with the bichromatic force.
(c) Beam collimated with optical molasses.
(d) Combination of both collimation methods.

the electrons that are ejected when metastable helium atoms hit a stainless steel plate. Of course the detector is also sensitive to UV light and to charged particles. To get a measure for the part of the signal that is due to other contributions than He* atoms, we did an experiment with blue molasses. That means we changed the detuning of our light going to the molasses setup to a frequency above atomic resonance (*blue*). That means that the sign in

Eq. (2.10) is reversed so that all the atoms are pushed out of the central region. By measuring the change in the current of the SSD when the blue molasses is blocked, we determined for the front SSD that 38% of the current produced by the uncollimated output from the source is the real contribution from metastable helium atoms. For the back SSD no effect of the blue molasses configuration could be observed. That could mean that only a small fraction of the signal is due to metastables as an effect of a larger divergence of the atomic beam compared to emitted UV light from the source. However, it could also be that the molasses stage is too far away from the back SSD so that the effect gets less clear. To rule out that possibility it is necessary to use a blue molasses setup close to the back SSD. For all numbers given here it is assumed that a similar percentage of the signal stems from He* atoms as with the front SSD.

The crossed slit SSD that is 33 cm away from the skimmer plate has to be scanned by hand. Since doing a two dimensional scan by hand takes a lot of time, the front SSD is mostly just used for determining the peak flux. That can be done rather quickly by maximizing the signal while moving the slit corresponding to the first dimension and afterwards maximizing the signal by moving the second dimension slit. When the peak is found it can be further maximized by adjusting the power going into the high intensity molasses beam. That typically leads to values for the peak flux between $3 \cdot 10^9$ $^{\text{atoms}}/_{\text{s}\cdot\text{mm}^2}$ and $6 \cdot 10^9$ $^{\text{atoms}}/_{\text{s}\cdot\text{mm}^2}$, corresponding to a current of approximately $40 - 80$ pA. The result of a complete two dimensional scan with the front SSD is shown in

figure 6.2.

In figure 6.3 a one dimensional scan across the peak position is shown. The big slit is positioned at 26.7 mm and the small slit is scanned over the peak. The figure not only shows the uncollimated source output and the combined collimation of the bichromatic force and optical molasses but also the two collimation methods separately. From these profiles it can be seen that the total peak flux is more than the sum of the peak flux numbers of the single collimation stages. That is the case because the bichromatic force has a large capture range and therefore is able to collect a lot of atoms from the source and slow them down to within the capture range of the molasses stage. Due to the smaller final velocity of optical molasses compared to the bichromatic force, the phase-space is compressed further which leads to a significant increase in the peak flux.

The peak flux measured with the front SSD has only limited significance for the flux at the position of the sample. In addition, the picoammeter that is used to measure the current from the SSDs is extremely sensitive to external noise. It is, for example, clearly visible in the signal if people move around too close to the vacuum system. Since the back SSD sits on top of the motorized stages, at the same position the sample is mounted during the exposure, and the stages can be fully controlled by a computer program (see appendix C), we can obtain less noisy scans with a higher resolution at the position where the exposure is taking place. An example for a two dimensional scan with the back SSD is shown in figure 6.4. Each scan consists of almost 300 datapoints that

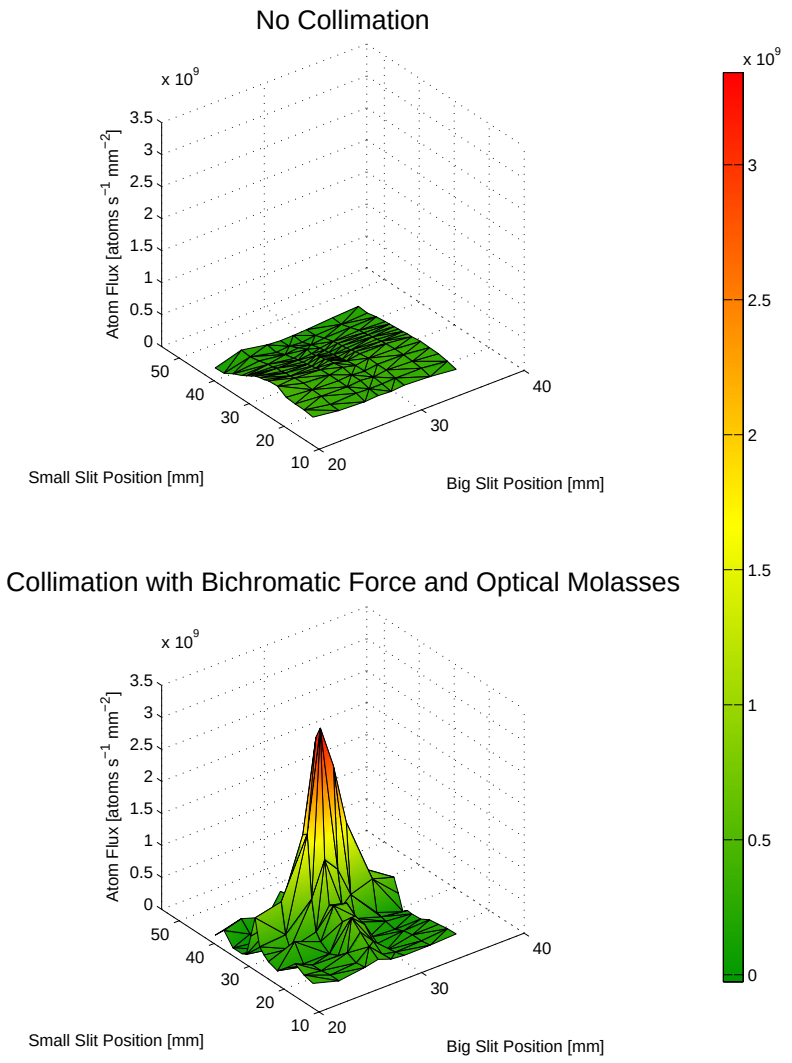

Figure 6.2 Two dimensional profile of the atomic beam (measured with the front SSD). The top part shows the uncollimated output from the source, the bottom part shows the beam when collimated with the bichromatic force and optical molasses. Both parts are using the same scale to make a comparison easier.

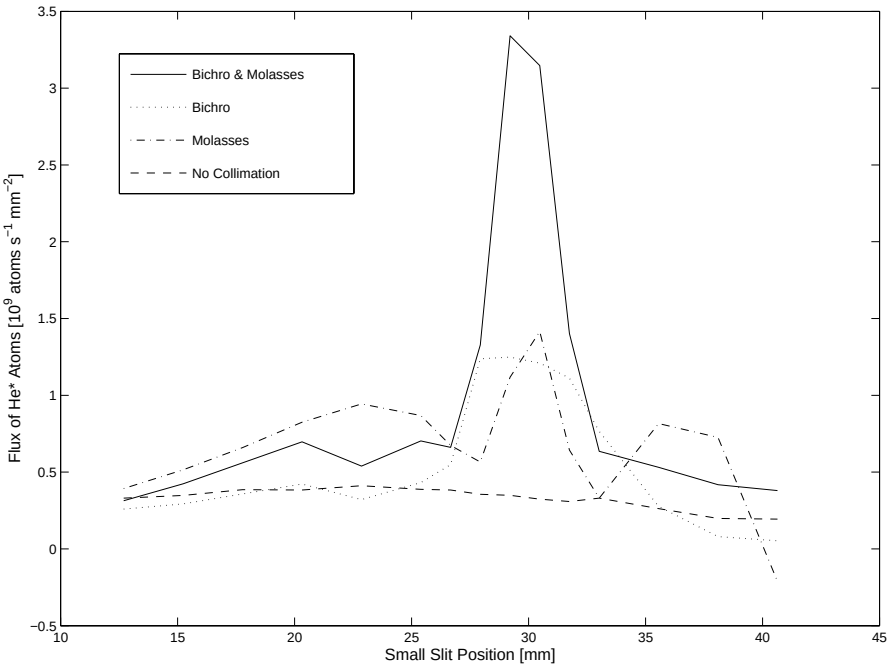

Figure 6.3 One dimensional scan across the peak of the atomic beam. In addition to the uncollimated output of the source and the collimation result with both collimation stages (bichromatic collimation and optical molasses), also the collimation effects of the single collimation methods are shown.

are equally spaced with a distance of 0.5 mm between neighboring points. Although the resolution is much higher than in the two dimensional scan recorded by hand with the front SSD, it takes only ~ 20 min for one complete scan.

In both parts of the picture a sharp edge is clearly visible where the signal drops immediately to ≈ 0. That is the "shadow" of the beam defining slits and demonstrates that they are doing a good job blocking everything coming from the source. The peak flux is about one order of magnitude smaller than

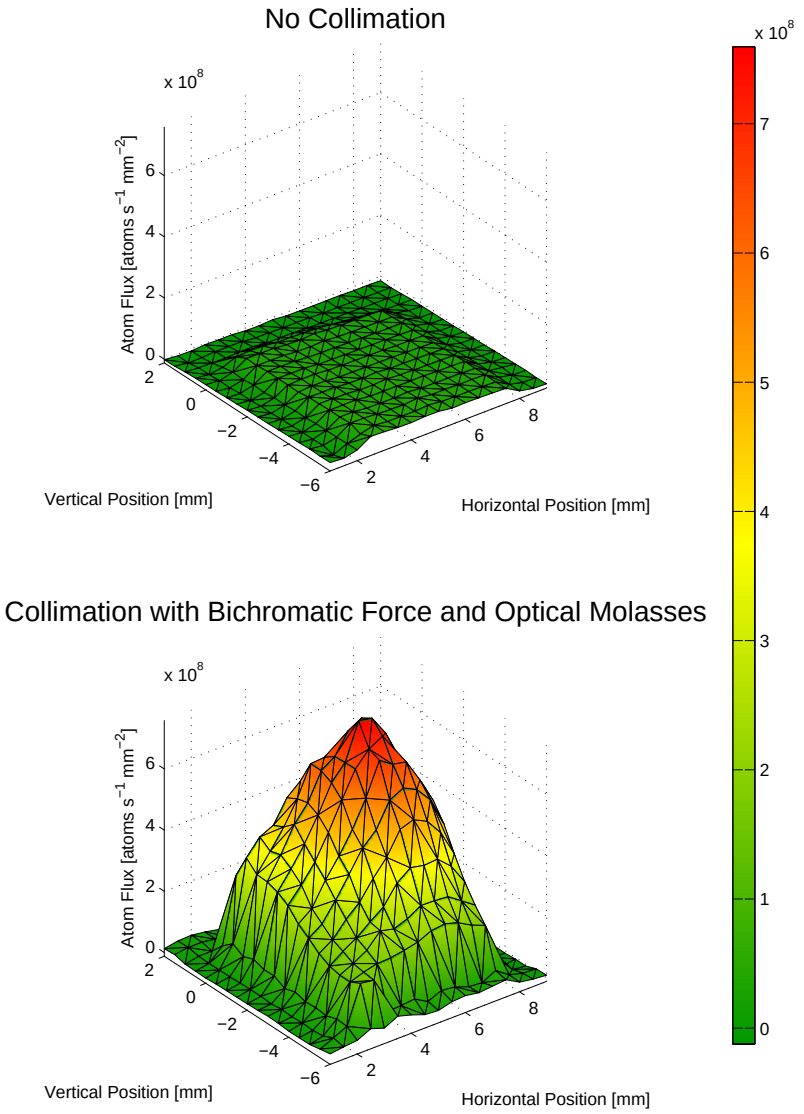

Figure 6.4 Two dimensional profile of the atomic beam (measured with the back SSD). The top part shows the uncollimated output from the source, the bottom part shows the beam when collimated with the bichromatic force and optical molasses. Both parts are using the same scale to make a comparison easier.

the one measured with the front SSD. Since lower flux numbers mean longer exposure times, a second molasses stage is in preparation to get an atomic beam with less divergence which automatically leads to higher flux numbers at the end of the beamline.

6.2 Neutral Atom Lithography

6.2.1 Improvements in the Experimental Setup

First results with a small grid as a material mask were already obtained in our lab about one year ago [6]. The edge resolution in these exposures was $60 - 70$ nm. These experiments showed that the techniques as applied in our lab are working for the use in NAL but they also showed the negative aspects:

- A maximum of three exposures in a fifteen hour day was achievable - but only if no problem occurred.

- The beamline was extending onto the optical table thereby making it difficult to get access to the sample chamber (that was also very small) and very likely to misalign the optics when switching samples.

- It was very hard to give actual numbers on the dosage of He* atoms during an exposure since

  - The laser lock was very weak, making it necessary to keep it on resonace by hand without real control over how well that could be

achieved. That led to changes in the collimation efficiency over time and thus in the atomic flux.

  - The sample holder was designed to hold the sample in one specific position so a misalignment in the collimation of the atomic beam could easily lead to a situation where the sample was only hit by the weaker part of the beam or even missed completely.

- Barely any space was left on the optical table for further extensions in the experimental setup, for example to set up a more complicated light mask.

Rebuilding the Vacuum System

The long list of problems finally led to the decision to completely rebuild the experimental setup in a way that it is possible to concentrate more on new aspects of NAL rather than dealing with collimation problems or tightening ConFlat flanges. Starting from late fall 2005 in a first step the vacuum system was almost completely disassembled, put on a new, bigger stand and extended in several ways: The SSD was moved from the end of the vacuum system closer to the collimation region where it originally used to be when the experiments with bichromatic collimation were done [34, 65]. A manual shutter was inserted in the beamline that made it possible to quickly block the atomic beam. The old lithography chamber was replaced by a bigger spherical cube with two quick access doors that now made it possible to access the chamber without the need for loosening and tightening ConFlat flanges. It also gave enough space for a

second MCP/Phosphor Screen and two movable beam defining slits that were needed to have the option of multiple exposures without bringing the vacuum system up to air.

Changes in the Optical Setup

Since the experiment was not only modified but completely moved to another laboratory, all the optics had to be newly set up. By moving the diode laser and the SAS setup to a second optical table and better planning of the setup, it was possible to organize the optics in a way that the functional units (light production, 4-frequency production, light amplification, collimation) were set up separately and about half of the optical table is still free for future extensions of the setup. The use of a commercial analog PID controller in the locking electronics (see section 4.2.2) made it possible to lock the laser on atomic resonance for several hours without the need of manual intervention. By creating the preconditions for a dual signal amplification with one fiber amplifier, enough light for a light mask is available. Since optical fibers were inserted in some new places, for example to get light to the SAS setup, an easy switching between different configurations (even between two experiments that both use the same vacuum system and part of the optics) was made possible.

Automating Parts of the Daily Procedures

To do multiple exposures without opening the vacuum system, it is necessary to be able to control the position of the wafer from the outside of the vacuum

system. In order to do that, we attached two motorized translation stages with ~ 40 mm travel range each at the end of the beamline. They are connected via an electric vacuum feedthrough to external controllers that can be programmed via the serial port of a PC. A home-built sample holder allows for easy switching between different samples and one of the interchangeable holders is modified into an SSD with a pinhole in the front plate. That way, the stage can also be used for doing profiles of the atomic beam flux.

The stages are controlled with a Visual Basic 6.0 program that is explained in detail in appendix C. It can also readout a data acquisition box from National Instruments that is connected to the USB port of the PC, so that the scanning process with the SSD can be fully automated. By doing a two dimensional scan of the collimated peak and the uncollimated source output with the SSD every time before doing exposures, the dosage can be accurately calculated, and within the travel range of the stages the sample can be accurately positioned thus ensuring that the sample is hit with the highest flux possible.

6.2.2 Lithography Results

While still working with the old vacuum system, we repeated the experiments described in [6]. As a mechanical mask an electron microscope grid (2000 Mesh, i.e. 2000 lines per inch, periodicity of 12.7 μm) was used. The peak flux was measured to be $1.8 \cdot 10^9$ $^{\text{atoms}}/_{\text{mm}^2\cdot\text{s}}$. The wafer was exposed for 40 min. Under the assumption that the sample was indeed exposed to the part of the atomic beam with the highest flux, that leads to a dosage of $4.3 \cdot 10^{12}$ $^{\text{atoms}}/_{\text{mm}^2}$.

By assuming that the active area of one SAM molecule is 0.22 nm^2 [55], 0.94 He* atoms on average are enough to damage one molecule of the resist layer. The etching time was 7 minutes.

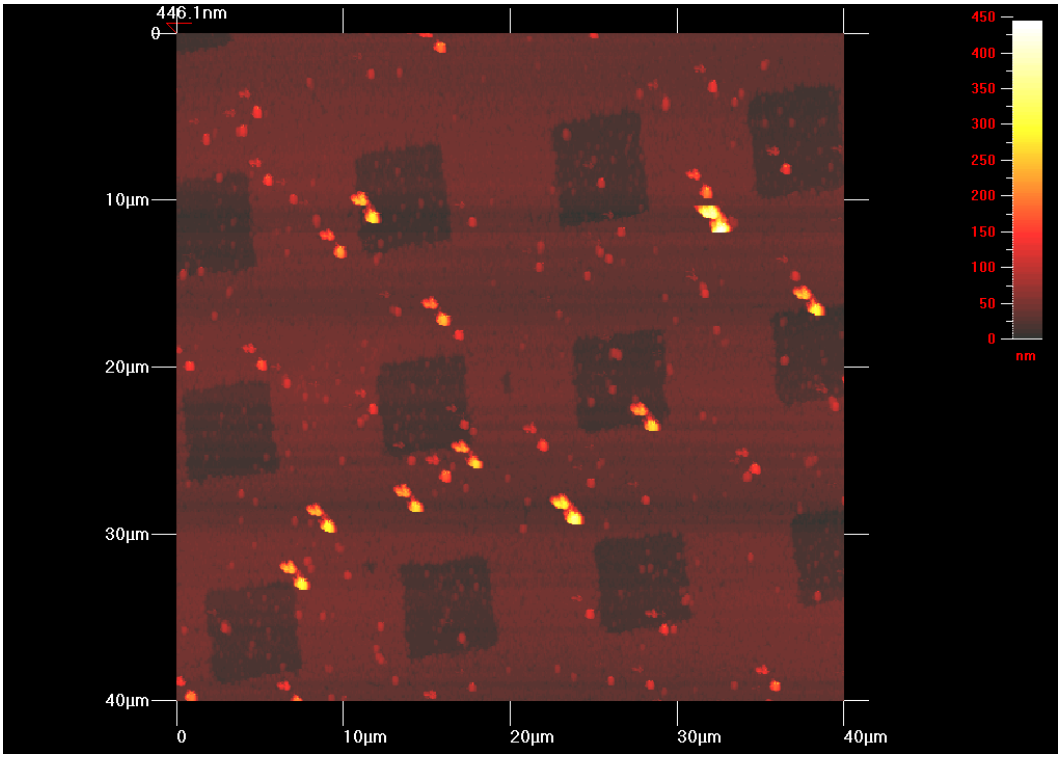

Figure 6.5 AFM Scan of a sample with good contrast. The boxes were created by using a micromesh as a mechanical mask during the exposure. The bright spots are from contaminations on the gold layer.

The AFM scan in figure 6.5 shows clearly the boxes that were etched in the gold layer where the wafer was exposed to the atomic beam. When looking at a histogram of the height distribution of the scan (see figure 6.6) two peaks are clearly visible at $\sim$ 19 nm and $\sim$ 40 nm which is a good indication that the SAM covered parts were barely affected by the etching process while in the exposed parts almost the whole 20 nm thick gold layer was etched away.

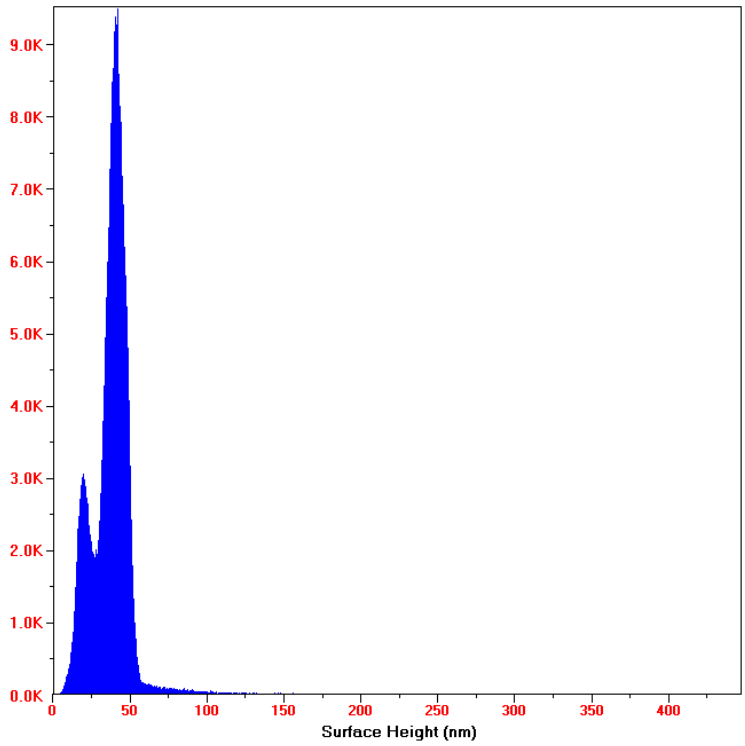

Figure 6.6 Histogram of the height distribution. The peaks are located at $\sim$ 19 nm and $\sim$ 40 nm, a good indication that the etching solution etched the exposed parts all the way through the 20 nm thick gold layer.

To reduce influences like over- or underexposure and over- or underetching, it is important to exactly know the right dosage of He* and the correct etching time. Therefore it is worth investing time in finding the right parameters for that. So that was the first thing we tried to figure out as soon as we had control over the modified beamline and optical setup. That work is still in progress but the advantages of the new experimental setup were already clearly visible. It is now easily possible to do up to 10 exposures a day and since the main limiting factor right now is the rather long exposure time of $\sim$ 30 min due to an only moderate atomic flux, the efficiency of the exposure process can

probably be further increased by collimating the atomic beam better with a second optical molasses stage with smaller final transverse velocities of the atoms.

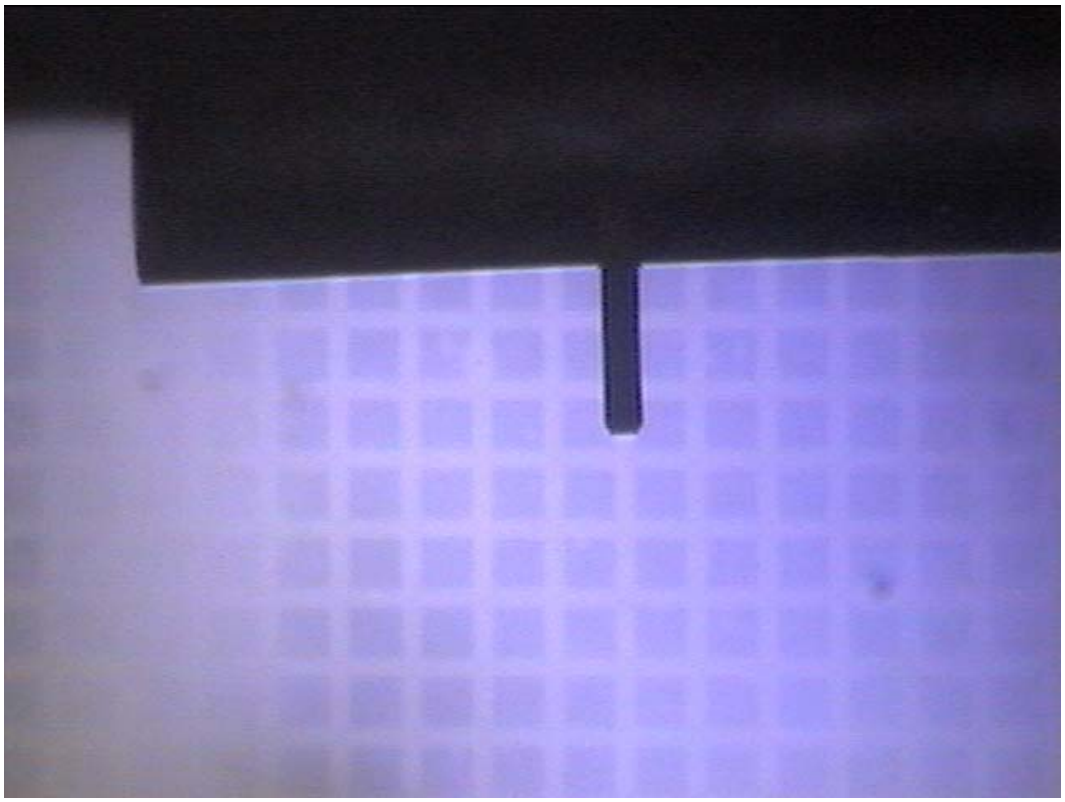

Figure 6.7 View with the camera mounted on top of the AFM. The small black part is the cantilever of the AFM. The underlying sample is out of focus but the etched structures are still visible.

For some of the exposures that were done so far with the new system, a coarser mesh ($\sim$ 100 μm periodicity) was used as a mask. The structures created that way are even big enough to be seen with the camera mounted on top of the AFM to monitor and position the cantilever tip (see figure 6.7). When looking at an actual AFM scan (figure 6.8) or the height distribution

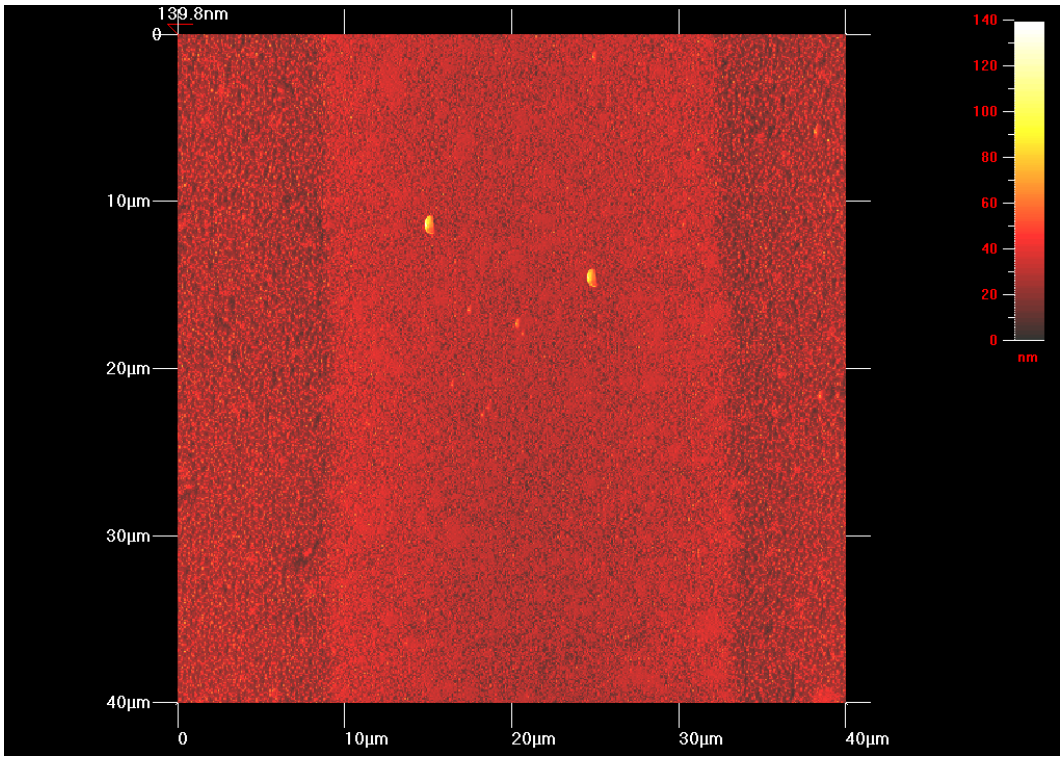

Figure 6.8 AFM Scan of a sample with weak contrast. The roughness of the surface everywhere and the small difference in height between exposed and unexposed parts is a clear sign for wrong exposure/etching parameters

histogram (figure 6.9) of those structures, it can be seen that the exposure and/or the etching parameters weren't quite correct yet. The surface of the exposed areas is very uneven, an indication that the etching process didn't penetrate all to the silicon surface that would be very flat. That assumption is further supported by the position of the two peaks in the height histogram (23 nm and 34 nm) that are closer together than the 20 nm thickness of the gold layer.

Since the AFM scans take a considerable amount of time to scan a region of up to 40 μm $\times$ 40 μm other options of looking at the wafer surface have to be

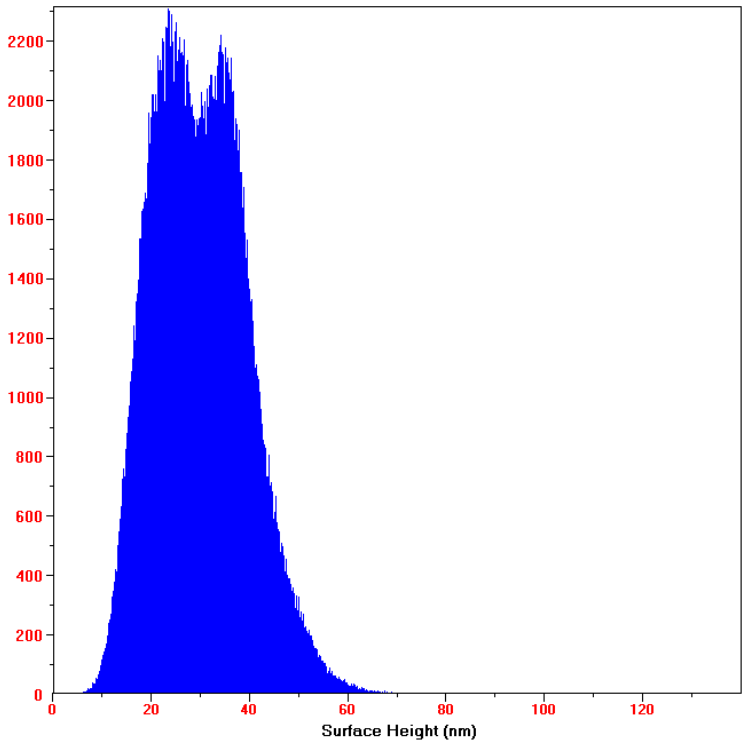

Figure 6.9 Histogram of the height distribution. The peaks are located at $\sim$ 23 nm and $\sim$ 34 nm. That means that the sample doesn't have the best contrast possible (that would be the thickness of the gold layer = 20 nm).

explored. Figure 6.10 shows a picture taken with an optical microscope. The boxes have a periodicity of ≈ 10 μm and the picture shows that a good optical microscope provides an easy way of looking for interesting parts on the wafer in real time. These regions can be scanned afterwards in more detail with the AFM to get a better picture of the quality of the structures. The optical microscope is also a good way of looking at the overall structure. Especially for creating periodic structures that extend over several millimeters it is important to check if the structures only exist in a very small region or if they spread over a considerable area on the wafer. Pictures taken with a light microscope

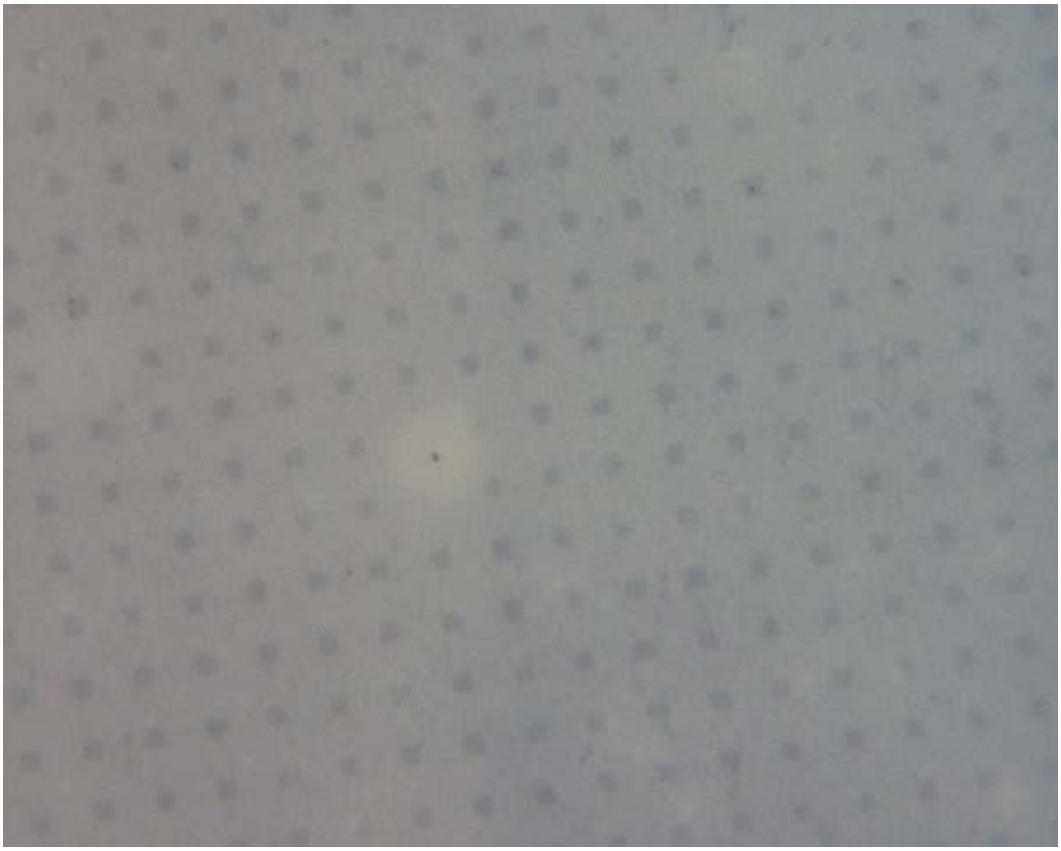

Figure 6.10 Picture of a patterned wafer taken with an optical microscope. The periodicity of the structures is ≈ 10 μm

.

with lower resolution show that the boxes created with a fine mesh extend at least over an area of 1 mm $\times$ 1 mm.

The results show the importance of gaining a good understanding of the dependence of the etching process on the exposure time and the time the wafer stays in the etching solution. The work done so far is the first step in analyzing those parameters quantitatively. Once that will be done it might be possible to get close to the resolution limit of $\sim$ 20 nm that arises from

the homogeneous etching procedure used that is etching to the side as well as in the desired downward direction. For further improvement in the resolution it would be necessary to switch to another etching technique. Since etching techniques that etch preferentially downwards have been explored widely for applications in the microchip industry, a transfer of similar techniques that can be used together with alkanethiol SAMs seems attainable.

Chapter 7

Conclusion

Starting from a setup that produces a bright beam of metastable helium [4] and first results in neutral atom lithography (NAL) [6] it was necessary to completely rebuild the system to be able to proceed in a more effective and reproducable manner with NAL experiments. A better separation between the vacuum system and the optical setup as well as an easier access to the sample chamber were the main motivations for the complete restart. In the process of setting everything up again, not only those goals were achieved but also a lot of other things. The optical setup was structured more clearly and now consists of independent parts that are connected via fibers which makes the experiment more flexible. The laser locking was drastically improved by inserting a PID controller in the locking electronics. By installing motorized stages in the vacuum system that can both hold a detector or a wafer for lithography experiments, it is now possible to do multiple exposures without opening the vacuum system. Also, we can now determine the atomic flux at the very position where the exposure happens.

All those changes laid the foundations for future advances in NAL experiments. By now being able to precisely determine the dosage of He* atoms and doing multiple exposures in a single day (whose number is now mostly limited by the exposure time while before it was mainly limited by the time needed for preparing an exposure) we're on the way of improving the exposure and etching procedure to minimize errors connected to uncertainties in those fields. First results are presented in this thesis and the determination of the optimum parameters is expected soon.

The next steps for the experiment are the use of a second optical molasses stage to reduce the divergence of the atomic beam even further. That would help decreasing the exposure times and reducing aberrations when using light masks in the exposure process. The use of standing wave light masks with 1083 nm and 389 nm light should demonstrate the use of non-material masks for patterning the atomic beam. In order to get enough light from the diode laser, a setup has been developed and implemented that allows for the amplification of two independent signals with one fiber amplifier.

After the use of simple geometrical beam configurations as light masks, the intermediate goal is to move on to creating more complicated patterns which hasn't been done by any group so far. Since the *inverse problem*, i.e. the calculation of the intensity distribution of a light field that is necessary to create a specific pattern on the sample, has not been solved analytically so far, it might be necessary to use a genetic algorithm approach to do so. Since the shaping of laser beams with computer controlled spatial light modulators

[66, 67] provides an easy way of creating more complex light masks, there might still be a big potential in the field of atomic nanofabrication that hasn't been explored yet.

Appendix A

Spectroscopic Data for He* transitions

	$2^3S_1 - 2^3P_2$	$2^3S_1 - 3^3P_2$
Wavelength (λ)	1083.33 nm	388.98 nm
Excited State Lifetime (τ)	98.04 ns	106.83 ns
Transition Linewidth ($\gamma/2\pi$)	1.62 MHz	1.49 MHz
Saturation Intensity ($I_S = \pi hc/3\lambda^3\tau$)	0.17 $^{\mathrm{mW}}/_{\mathrm{cm}^2}$	3.31 $^{\mathrm{mW}}/_{\mathrm{cm}^2}$
Recoil Frequency ($\omega_r/2\pi$)	42.46 kHz	329.35 kHz
Capture Velocity ($v_c = \gamma/k$)	1.76 $^{\mathrm{m}}/_{\mathrm{s}}$	0.58 $^{\mathrm{m}}/_{\mathrm{s}}$
Doppler Velocity ($v_D = \sqrt{\hbar\gamma/2M}$)	28.44 $^{\mathrm{cm}}/_{\mathrm{s}}$	27.25 $^{\mathrm{cm}}/_{\mathrm{s}}$
Recoil Velocity ($v_r = \hbar k/M$)	9.200 $^{\mathrm{cm}}/_{\mathrm{s}}$	25.6 $^{\mathrm{cm}}/_{\mathrm{s}}$

Table A.1 Mass $M = 6.646 \cdot 10^{-27}$ kg, Doppler Temperature $T_D = \hbar\gamma/2k_B$, $k = 2\pi/\lambda$, all data from Ref. [1].

Appendix B

Code for Bichromatic Force Calculations

```
1  program force
2    implicit none
3
4    ! constants
5    ! lambda is the wavelength, k the wavevector, gamma the linewidth of the atomic
         transition
6    ! the calculated force will be given in multiples of forfact, the velocity in multiples
         of velfact
7    double precision pi, lambda, k, hbar, gamma, forfact, velfact
8    parameter(pi=3.141592654, lambda=1083.0E-9, hbar=1.054572E-34, gamma=10.2E6)
9    parameter(k=2.0*pi/lambda, forfact=hbar*k*gamma, velfact=gamma/k)
10
11   ! input parameters
12   ! datapoints gives the number of velocity steps calculated
13   integer datapoints
14   parameter(datapoints=1024)
15   ! vmin and vmax are the minimum and maximum velocity
16   double precision vmin / (-30.0*velfact) /
17   double precision vmax / (0.0*velfact) /
18   ! delta is half the beat frequency (angular frequency)
19   double precision delta / (5.89*gamma) /
20   ! wR is the Rabi frequency (gives the light intensity)
21   double precision wR / (4.63*gamma) /
22   ! d is omega - omega_atom, i.e. the detuning of the carrier frequency from atomic
         resonance (angular frequencies)
23   double precision d / (0.0*gamma) /
24   ! phi is the relative phase between the counterpropagating pulses
25   double precision phi / (pi/2.0) /
26   ! relative and absolute tolerance for the numerical ODE solver
27   double precision rtol / 1.0E-4 /
28   double precision atol / 1.0E-4 /
29
30   integer i
31
32   ! several definitions for the numerical ODE solver
33   ! number of differential equations
34   integer neqn
35   ! initial step size for the ODE solver
36   double precision h0
37   integer lwork,liwork
38   parameter(neqn=3)
39   parameter(lwork=24+neqn*(48+2*neqn),liwork=37+neqn)
40   double precision work(lwork)
41   integer iwork(liwork)
42   ! real parameters that can be used in the ODE solving subroutine
43   double precision rpar(9)
44   ! integer parameters that can be used in the ODE solving subroutine
45   integer ipar(1)
46   ! return code of the ODE solver
47   integer idid
48   external feval, jeval, solout
49   integer ijac, mljac, mujac, iout
```

```
50
51    ! array for the calculated force values
52    double precision F(datapoints)
53    ! Bloch vector
54    double precision r(3)
55    ! velocity range and stepsize
56    double precision vrange, vstep
57    integer ndata
58    ! velocity, infinitesimal force contribution, start time, stop time for one ODE step,
          end time, time step
59    double precision v, dF, tstart, tstop, tend, dt
60    integer ntime
61    ! averaged force
62    double precision FF
63    integer icount
64    double precision term1, term2
65    integer pos1, pos2, pos3
66
67    ! initialize for ODE solver (default parameters for work)
68    do i = 1, 14
69      work(i) = 0.0
70    end do
71    idid = 0
72    ijac = 0
73    mljac = neqn
74    mujac = neqn
75    iout = 0
76
77    iwork(1) = 100000 ! max number of integration steps
78    iwork(2) = 4   ! min order for ode solving process (between 4 and 12)
79    iwork(3) = 12  ! max order for ode solving process (between min order and 12)
80    iwork(4) = 10  ! max number of blended iterations per integration step, order 4
81    iwork(5) = 12  ! max number of blended iterations per integration step, order 6
82    iwork(6) = 14  ! max number of blended iterations per integration step, order 8
83    iwork(7) = 16  ! max number of blended iterations per integration step, order 10
84    iwork(8) = 18  ! max number of blended iterations per integration step, order 12
85
86    ! parameters that can be used during the ODE solving process
87    rpar(1) = gamma
88    rpar(2) = -gamma/2.0
89    rpar(3) = d
90    rpar(4) = delta
91    rpar(5) = 0      ! is set to k*v in each v-step
92    rpar(6) = 4.0*wR*dsin(phi/4.0)
93    rpar(7) = 4.0*wR*dcos(phi/4.0)
94    rpar(8) = -2.0*hbar*k*wR*dsin(phi/4.0)
95    rpar(9) = -2.0*hbar*k*wR*dcos(phi/4.0)
96
97
98    vrange = vmax - vmin
99    vstep = vrange / datapoints
100   ndata = 0
101
102   ! open file for output
103   open(unit=88, file='output.dat')
104
105   ! loop on velocities
106   do v = vmin + vstep/2.0, vmax, vstep
107     ndata = ndata + 1
108     dF = 0.0
109     rpar(5) = k*v
110
111     ! initial Bloch vector
112     r(1) = 0.0
113     r(2) = 0.0
114     r(3) = -gamma
115
116     tstart = -1.0E-5
117     dt = 1.0 / (max(dabs(delta), dabs(k*v)) * 10.0)
118     tend = 100.0 * 2.0 * pi / dabs(k*v) * idint(1.0+200 * dabs(k*v) / delta)
119     ntime = idint(tend/dt)
120
121     ntime = idint((tend-tstart)/dt)
122     ! start with a force of 0 and add up infinitesimal contributions
123     FF = 0.0
124     icount = 0
125     h0 = dt / 1000.0
126
127     ! loop on time
128     do i = 1, ntime
129       tstop = tstart + dt
```

```
130         ! call routine for ODE solving
131         call bim(neqn, feval, tstart, tstop, r, h0, rtol, atol, jeval, ijac, mljac, mujac,
                work, lwork, iwork, liwork, rpar, ipar, iout, idid)
132         ! error handling
133         if (idid.ne.0) then
134           write(*,*) 'ERROR: returned idid =', idid
135         end if
136
137         ! time until 0 is just for initializing the Bloch vector, after that the force
                contributions are added up
138         if (tstop .ge. 0.0) then
139           icount = icount + 1
140           term1 = rpar(9) * dcos(delta*tstop) * dsin(rpar(5)*tstop) * r(1)
141           term2 = -rpar(8) * dsin(delta*tstop) * dcos(rpar(5)*tstop) * r(2)
142           dF = term1 + term2
143           FF = FF + dF
144         end if
145       end do
146
147       ! get the average force
148       F(ndata) = FF/real(icount)
149       ! write output in multiples of velfact and forfact
150       write(88,9999) v/velfact, F(ndata)/forfact
151     end do
152
153     9999 format(2F25.9)
154     stop
155   end
156
157
158   ! subroutine implements optical Bloch equations (OBEs)
159   subroutine feval(neqn, t, r, dr, ierr, rpar, ipar)
160     integer neqn, ierr, ipar
161     double precision t, r(neqn), dr(neqn), rpar(9), a, b
162
163     ! rpar(1) = gamma
164     ! rpar(2) = -gamma/2.0
165     ! rpar(3) = d
166     ! rpar(4) = delta
167     ! rpar(5) = k*v
168     ! rpar(6) = 4.0*wR*dsin(phi/4.0)
169     ! rpar(7) = 4.0*wR*dcos(phi/4.0)
170     ! rpar(8) = -2.0*hbar*k*wR*dsin(phi/4.0)
171     ! rpar(9) = -2.0*hbar*k*wR*dcos(phi/4.0)
172
173     a = rpar(6) * dsin(rpar(5)*t) * dsin(rpar(4)*t)
174     b = rpar(7) * dcos(rpar(5)*t) * dcos(rpar(4)*t)
175
176     dr(1) = rpar(2)*r(1) + rpar(3)*r(2) - a*r(3)
177     dr(2) = rpar(3)*r(1) + rpar(2)*r(2) + b*r(3)
178     dr(3) = a*r(1) - b*r(2) - rpar(1)*r(3) + rpar(1)
179
180     return
181   end
182
183
184   ! subroutine for evaluating the Jacobian of the function
185   ! just dummy, since Jacobian is calculated numerically
186   subroutine jeval (neqn, t, y, jac, ldim, ierr, rpar, ipar)
187     integer neqn, ldim, ierr, ipar
188     double precision t, y(neqn), jac(ldim, neqn), rpar
189
190     return
191   end
192
193
194   ! subroutine for output after each step
195   ! just dummy, since no output after each step
196   subroutine solout(m, t, y, f, k, ord, irtrn)
197     integer m, k, ord, irtrn
198     double precision t(k), y(m, k), f(m, k)
199
200     return
201   end
```

Listing B.1 FORTRAN Code: Numerically Solves the Optical Bloch Equations

Appendix C

Program for Stage Control and Data Readout

The program for the control of the stage movements and the readout of the picoammeter is done by a program written in Visual Basic 6.0. The stages are addressed via the serial port of the computer while the data readout is done by using a National Instruments data acquisition box that is connected to the USB port. The source code of the program is too long to include it in the thesis. Nonetheless, the code is commented to make it easy for other people to understand the program and extend its functionality. In this appendix only the user interface is described to facilitate the handling of the program.

C.1 Start and Initialization

When starting the program by double-clicking on *StageControl.exe*, the program first tries to detect if any stage controllers are connected. If the program fails to detect at least one of the two stages, it displays an error message like that in figure C.1.

Possible reasons for that are problems with the serial connection of the controllers or the fact that the power supply for the stage controllers isn't

Figure C.1 Error message that is displayed when the controller 1 can't be found. A similar is displayed for controller 2 if it can't be detected.

turned on. It can also be that the stage controller are in an faulty internal state which can often be solved by turning off the power supply for the stage controllers and turn it back on. A third possible reason are wrong settings in the program for the serial port configuration. How that can be changed is described in section C.2.1.

After a successful (or not successful) detection of the stages the main window of the program (see figure C.2) is displayed. Most of the controls are usually disabled at that point unless the stages were initialized before and haven't been turned off since. Otherwise there are two options how to initialize the stages. The first is by pressing the button *Enable* which enables the stages (and with them most of the buttons in the control window) and defines the current position as the home position. The home position is the zero position of the stages. Negative position values for the vertical stage mean that the stage is below the home position, positive values are describing the positions above. Negative values for the horizontal stage correspond to a position further away from the optical table than the home position, positive

values correspond to positions closer to the optical table.

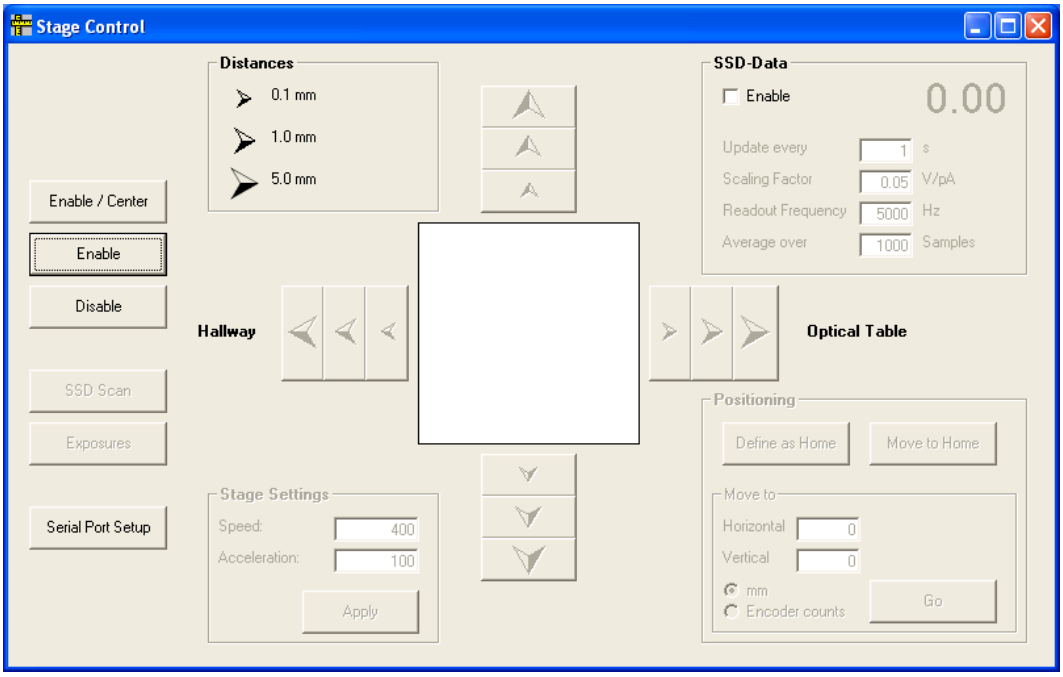

Figure C.2 Main window of the program while the stages are not yet enabled.

The second way of enabling the stages is by pressing *Enable / Center* which not only enables the stages but also centers them within their travel range and defines that center position as home. That way the coordinate system of the stages gets independent from the position of the stages during the startup.

Figure C.3 Message window after the centering process of the stages is completed.

The centering process can take a little while since the stages are moved over the whole travel range to detect the boundaries. After the centering process is complete the message box shown in figure C.3 is displayed.

C.2 The Main Control Window

C.2.1 Changing the Serial Port Configuration

To configure the serial port of the computer, a click on *Serial Port Setup* opens the dialog in figure C.4.

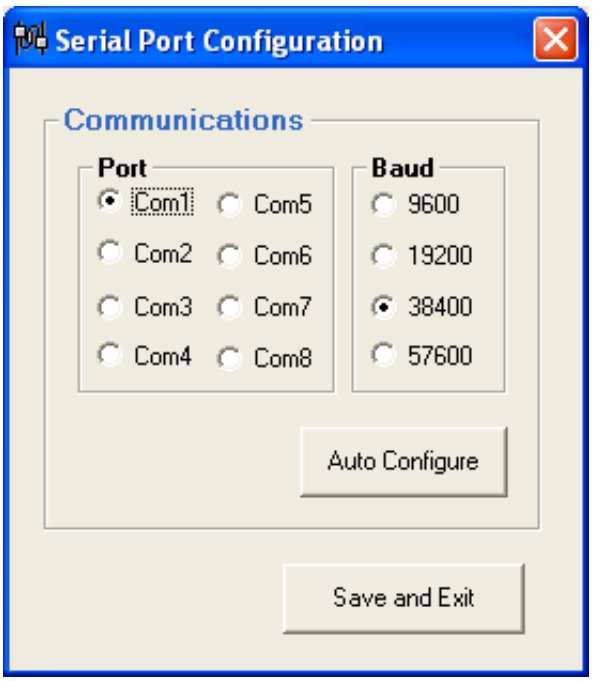

Figure C.4 Dialog for the configuration of the serial port.

If it is known which serial port the controllers are connected to and what the settings for the baud rate on the stage controllers are then the options can be selected by hand and saved as the standard configuration by clicking

on *Save and Exit*. If the parameters are not known a click on *Auto Configure* starts and automatic detection process. For that detection only one stage controller is allowed to be connected to the computer. To remind the user of that a message box is shown before the process starts.

The success of the detection procedure is shown in another message box. The detected settings are now marked in the dialog and a click on *Save and Exit* changes the values so that they are loaded when starting the program.

C.2.2 Moving the Stage by Hand

Clicks on the arrow buttons in the main window move the stage in the directions indicated. The step size of those movements is 0.1 mm, 1.0 mm or 5.0 mm depending on the selected button. If one wants to move the stage to a specific position it is possible to enter the position (in either mm or encoder counts in the lower right corner and press *Go*. Pressing the button *Define as Home* marks the current stage position as the $(0, 0)$ position and clicking on *Move to Home* has the same effect as choosing the position $(0, 0)$ and then pressing *Go*.

The speed and the acceleration of the stage can be changed by typing in new values in the *Stage Settings* box and then pressing *Apply*. The values are given in units that are related to encoder counts and time intervals of an internal timer. The factor for a conversion to standard units in speed and acceleration can be extracted from the manual for the stage controllers. Selecting too high values can impair the accuracy in the positioning process or

even severely damage the stages. Therefore the manual should be consulted prior to increasing the preset values dramatically.

C.2.3 Displaying Data Readout

To measure a current with the picoammeter and display the value within the program, the check-box *Enable* in the *SSD Data* box has to be marked. When doing so the program reads the measured value from the data acquisition box with the time-interval given. The readout frequency and the number of datapoints to average over (to get rid of any low-frequency noise, especially 60 Hz line noise) can also be specified. The scaling factor can be adjusted to be able to cover different amplification settings of the low noise preamplifier and different measurement ranges of the picoammeter. For changes in the settings to take effect it is necessary to click on the *Enable* check-box twice. That is done to prevent problems in the readout procedure when changes are made during one measurement. A screenshot of the main window when the SSD readout is activated is shown in figure C.5.

C.3 SSD Scans

By clicking on *SSD Scan* in the main window another window is opened which appearance is shown in figure C.6. The lower left corner of the SSD scan can be specified by adjusting the parameters for the *Starting Point*. The stepsize and the number of steps that are taken in both vertical and horizontal direction can be set independently of each other. That way it is also possible to just do

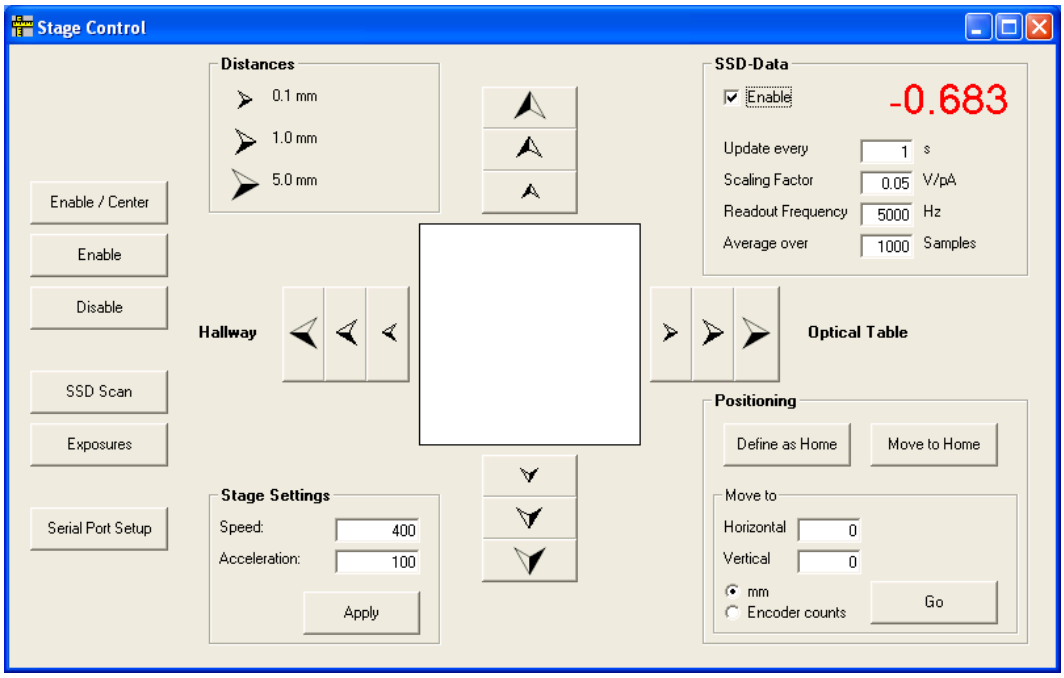

Figure C.5 Main window while the readout of the SSD is enabled.

one dimensional SSD scans (in that case either the *Number of Vertical Steps* or the *Number of Horizontal Steps* is set to 0. The *Settings for Scan* box contains fields to adjust different parameters for the stage behavior as well as for the readout process that are already explained in section C.2. In addition to that, *Wait before Scanning* defines the time before the scan starts after pressing the *Scan* button and after moving the stage to the start position. By waiting $10 - 30$ s the picoammeter can settle after the possibly long way to the start position and people can leave the laboratory since the picoammeter is easily influenced by people moving close by. *Wait after Moving* specifies the time between two scanning steps. A value of $2 - 3$ s turned out to be a good compromise between a high scanning speed and giving the picoammeter

enough time to settle after the movement of the stages.

When pressing the *Scan* button the scan is started with the given settings. During the scan the progress is displayed with a progress bar. The settings can't be adjusted while the program is scanning, but by pressing *Cancel* the scanning process is aborted. The measured values for the SSD current are displayed in a graphical way where the color corresponds to the measured value: blue indicates the lowest measured value during the scan, red marks the highest value, values in between are given a color whose red and blue components are calculated from the value with respect to the minimum and maximum value (see figure C.7). When moving the cursor on top of the colored field of a measured point a tool tip shows the corresponding stage position and

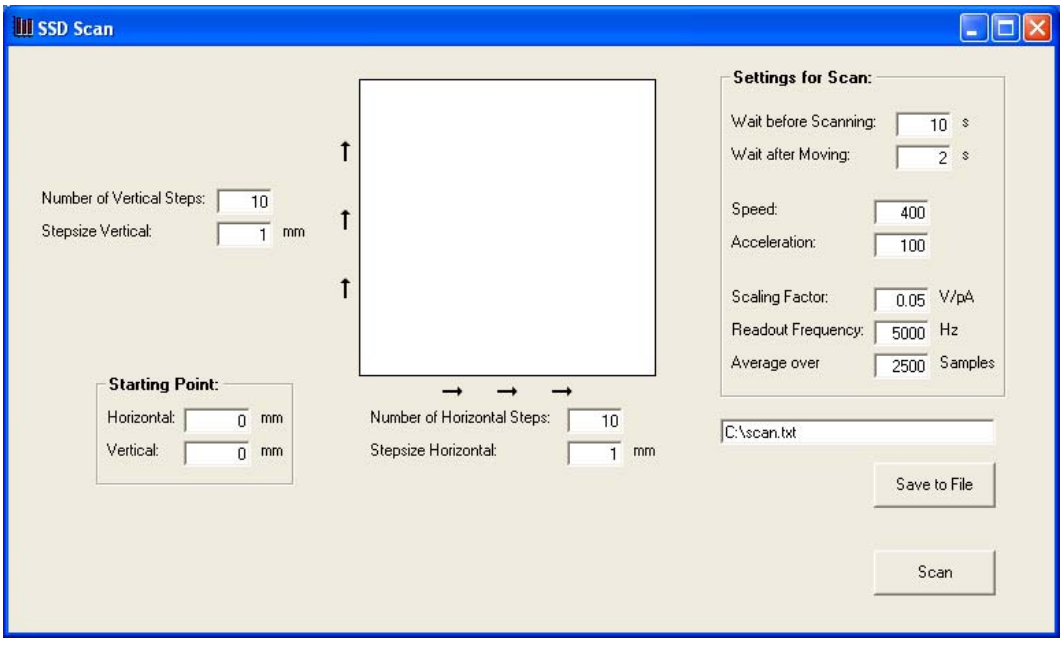

Figure C.6 Window for doing SSD scans. The results can be exported to a text file after the scan.

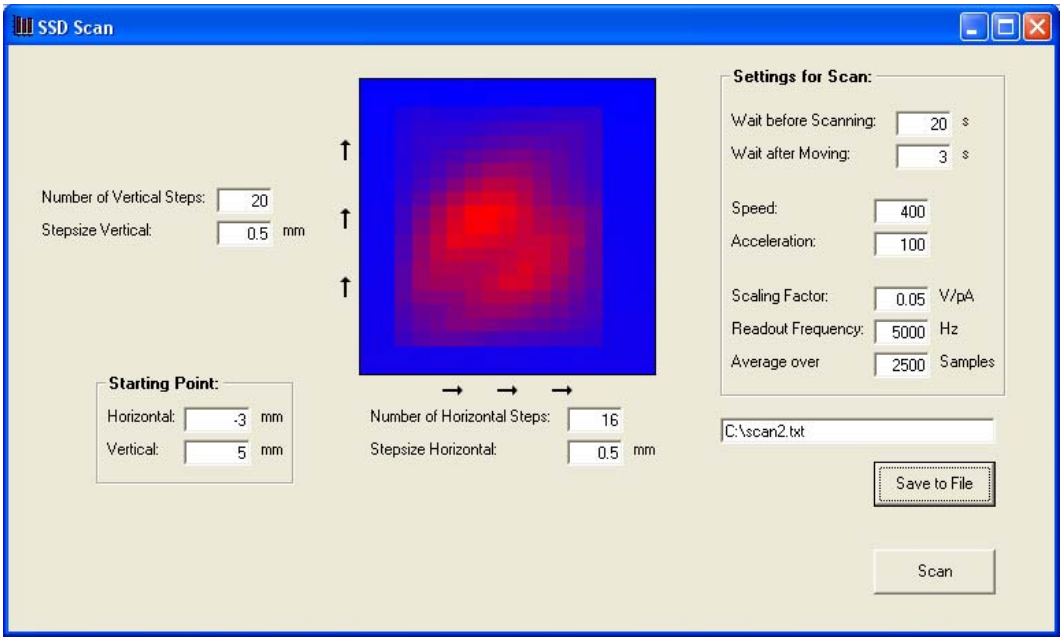

Figure C.7 Window for doing SSD scans after a scan is completed. The measured currents are represented with colors where red marks the highest value and blue the lowest.

the measured value. The data can be exported by choosing a file name and then pressing *Save to File* after the scan is done.

C.4 Scheduling Exposures

A click on *Exposures* in the main window opens another window where multiple exposures can be scheduled. For each exposure a position of the stage and the exposure time can be chosen. To remove an entry from the list it has to be marked by clicking on it and then can be removed by clicking on *Remove from List*. The *Do Exposures* button changes the look of the window (see figure C.8). The stage moves to the first specified position in the list and stays

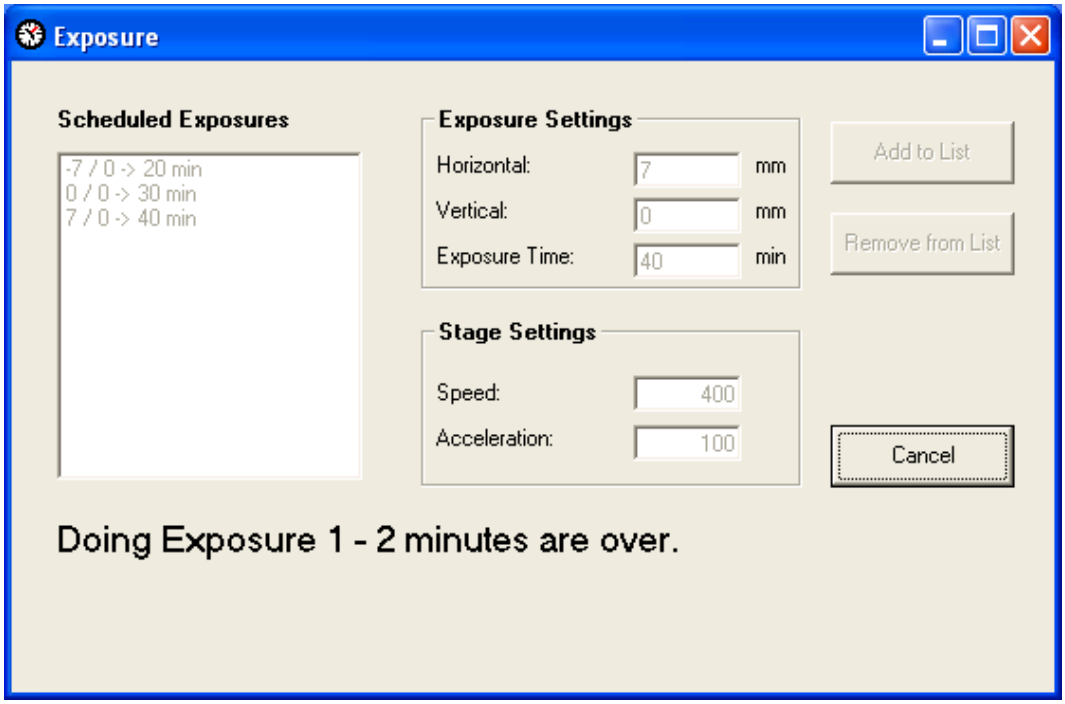

Figure C.8 Window for the scheduling of exposures. While the exposures are done the remaining time for the current exposure is displayed.

there for the entered time. The time that remains until the current exposure is done is displayed in the window. After each exposure the stage moves to the next position until the end of the list is reached. When the last exposure is done, a status message is shown that indicates that all tasks are completed.

Bibliography

[1] H. J. Metcalf and P. van der Straten, *Laser Cooling and Trapping*, *Graduate Texts in Contemporary Physics* (Springer-Verlag, New York, 1999).

[2] X. Miao, *Optical Force on Atoms with Periodic Adiabatic Rapid Passage Sequences*. Ph.D. thesis, Stony Brook University, 2006.

[3] M. T. Cashen and H. Metcalf, *Bichromatic Force on Helium*. Phys. Rev. A **63**, 025406 (2001).

[4] M. Partlow, X. Miao, J. Bochmann, M. Cashen, and H. Metcalf, *Bichromatic Slowing and Collimation to Make an Intense Helium Beam*. Phys. Rev. Lett. **93**, 213004 (2004).

[5] D. Meschede and H. Metcalf, *Atomic Nanofabrication: Atomic Deposition and Lithography by Laser and Magnetic Forces*. J. Phys. D: Appl. Phys. **36**, R17 (2003).

[6] M. P. Riedmann, *Neutral Atom Lithography Using a Beam of Metastable Helium Collimated by Bichromatic Light*. Master's thesis, Stony Brook University, 2005.

[7] A. Einstein, *Zur Quantentheorie der Strahlung*. Physikalische Zeitschrift **18**, 121 (1917).

[8] C. Doppler, *Über das farbige Licht der Doppelsterne und einiger anderer Gestirne des Himmels*. Abhandlungen der königlichen böhmischen Gesellschaft der Wissenschaften **2**, 465 (1843).

[9] J. V. Prodan and W. D. Phillips, *Chirping the Light - Fantastic? Recent NBS Atom Cooling Experiments*. Prog. Quant. Electron. **8**, 231 (1984).

[10] W. D. Phillips and H. Metcalf, *Laser Deceleration of an Atomic Beam*. Phys. Rev. Lett. **48**, 596 (1982).

[11] R. Gaggl, L. Windholz, C. Umfer, and C. Neureiter, *Laser Cooling of a Sodium Atomic Beam Using the Stark Effect*. Phys. Rev. A **49**, 1119 (1994).

[12] E. Kyrölä and S. Stenholm, *Velocity Tuned Resonances as Multi-Doppleron Processes*. Opt. Commun. **22**, 123 (1977).

[13] V. G. Minogin and O. T. Serimaa, *Resonant Light Pressure Forces in a Strong Standing Laser Wave*. Opt. Commun. **30**, 373 (1979).

[14] T. W. Hänsch and A. L. Schawlow, *Cooling of Gases by Laser Radiation*. Opt. Commun. **13**, 68 (1975).

[15] V. S. Voitsekhovich, M. V. Danileiko, A. M. Negriiko, V. I. Romanenko, and L. P. Yatsenko, *Light Pressure on Atoms in Counterpropagating*

Amplitude-Modulated Waves. Sov. Phys. Tech. Phys. **33**, 690 (1988). [Original Paper: Журнал Технической Физики **58**, 1174 (1988)]

[16] V. S. Voitsekhovich, M. V. Danileiko, A. M. Negriiko, V. I. Romanenko, and L. P. Yatsenko, *Observation of a Stimulated Radiation Pressure of Amplitude-Modulated Light on Atoms*. JETP Lett. **49**, 161 (1989). [Original Paper: Письма в ЖЭТФ **49**, 138 (1989)]

[17] M. O. Scully and M. S. Zubairy, *Quantum Optics* (Cambridge University Press, Cambridge, 1997).

[18] R. P. Feynman, F. L. Vernon Jr., and R. W. Hellwarth, *Geometrical Representation of the Schrödinger Equation for Solving Maser Problems*. J. Appl. Phys. **28**, 49 (1957).

[19] J. Söding, R. Grimm, Y. B. Ovchinnikov, P. Bouyer, and C. Salomon, *Short-Distance Atomic Beam Deceleration with a Stimulated Light Force*. Phys. Rev. Lett. **78**, 1420 (1997).

[20] L. Brugnano and C. Magherini, *The BiM Code for the Numerical Solution of ODEs*. J. Comput. Appl. Math. **164-165**, 145 (2004).

[21] J. R. Woodworth and H. W. Moos, *Experimental Determination of the Single-Photon Transition Rate Between the* 2^3S_1 *and* 1^1S_0 *States of He I*. Phys. Rev. A **12**, 2455 (1975).

[22] G. Łach and K. Pachucki, *Forbidden Transitions in the Helium Atom*. Phys. Rev. A **64**, 042510 (2001).

[23] J. E. Sansonetti and W. C. Martin, *Handbook of Basic Atomic Spectroscopic Data* (July 18, 2006),
URL: http://physics.nist.gov/PhysRefData/Handbook/index.html.

[24] F. M. Penning, *Über Ionisation durch metastabile Atome.* Naturwissenschaften **15**, 818 (1927).

[25] A. Chambers, *Modern Vacuum Physics*, *Masters Series in Physics and Astronomy* (Chapman & Hall/CRC, Boca Raton, 2005).

[26] J. M. Lafferty (ed.), *Foundations of Vacuum Science and Technology* (John Wiley & Sons, New York, 1998).

[27] J. Kawanaka, M. Hagiuda, K. Shimizu, F. Shimizu, and H. Takuma, *Generation of an Intense Low-Velocity Metastable-Neon Atomic Beam.* Appl. Phys. B: Lasers Opt. **56**, 21 (1993).

[28] D. W. Fahey, W. F. Parks, and L. D. Schearer, *High Flux Beam Source of Thermal Rare-Gas Metastable Atoms.* J. Phys. E: Sci. Instrum. **13**, 381 (1980).

[29] G. R. Woestenenk, J. W. Thomsen, M. van Rijnbach, P. van der Straten, and A. Niehaus, *Construction of a Low Velocity Metastable Helium Atomic Beam.* Rev. Sci. Instrum. **72**, 3842 (2001).

[30] M. T. Cashen, *Optical Forces on Atoms in Polychromatic Light Fields.* Ph.D. thesis, SUNY at Stony Brook, 2002.

[31] F. B. Dunning, R. D. Rundel, and R. F. Stebbings, *Determination of Secondary Electron Ejection Coefficients for Rare Gas Metastable Atoms*. Rev. Sci. Instrum. **46**, 697 (1975).

[32] J. S. Major Jr. and D. F. Welch, *Singlemode InGaAs/GaAs Distributed Bragg Reflector Laser Diodes Operating at 1083 nm*. Electron. Lett. **29**, 2121 (1993).

[33] C. J. Foot, *Atomic Physics*, *Oxford Master Series in Physics* (Oxford University Press, New York, 2005).

[34] J. Bochmann, *Atomic Beam Collimation Using the Bichromatic Force*. Master's thesis, Stony Brook University, 2004.

[35] R. Ulrich and A. Simon, *Polarization Optics of Twisted Single-Mode Fibers*. Appl. Opt. **18**, 2241 (1979).

[36] R. Ulrich, S. C. Rashleigh, and W. Eickhoff, *Bending-Induced Birefringence in Single-Mode Fibers*. Opt. Lett. **5**, 273 (1980).

[37] J. Sapriel, *Acousto-Optics* (John Wiley & Sons, Chichester, 1979).

[38] H. C. Lefèvre, *Single-Mode Fibre Fractional Wave Devices and Polarisation Controllers*. Electron. Lett. **16**, 778 (1980).

[39] D. E. Gray (coord. ed.), *American Institute of Physics Handbook* (McGraw-Hill, New York, 1972).

[40] M. R. Williams, *Measurement of the Bichromatic Force on Rubidium Atoms*. Ph.D. thesis, SUNY at Stony Brook, 1999.

[41] M. R. Williams, F. Chi, M. T. Cashen, and H. Metcalf, *Measurement of the Bichromatic Optical Force on Rb Atoms*. Phys. Rev. A **60**, R1763 (1999).

[42] M. R. Williams, F. Chi, M. T. Cashen, and H. Metcalf, *Bichromatic Force Measurements Using Atomic Beam Deflections*. Phys. Rev. A **61**, 023408 (2000).

[43] M. Born and E. Wolf, *Principles of Optics*, 7^{th} (expanded) ed. (Cambridge University Press, Cambridge, 1999).

[44] P. W. Milonni and J. H. Eberly, *Lasers* (John Wiley & Sons, New York, 1988).

[45] G. Timp, R. E. Behringer, D. M. Tennant, and J. E. Cunningham, *Using Light as a Lens for Submicron, Neutral-Atom Lithography*. Phys. Rev. Lett. **69**, 1636 (1992).

[46] R. W. McGowan, D. M. Giltner, and S. A. Lee, *Light Force Cooling, Focusing, and Nanometer-Scale Deposition of Aluminum Atoms*. Opt. Lett. **20**, 2535 (1995).

[47] B. Brezger, T. Schulze, U. Drodofsky, J. Stuhler, S. Nowak, T. Pfau, and J. Mlynek, *Nanolithography with Neutral Chromium and Helium Atoms*. J. Vac. Sci. Technol. B **15**, 2905 (1997).

[48] M. Kreis, F. Lison, D. Haubrich, D. Meschede, S. Nowak, T. Pfau, and J. Mlynek, *Pattern Generation with Cesium Atomic Beams at Nanometer Scales*. Appl. Phys. B: Lasers Opt. **63**, 649 (1996).

[49] R. Younkin, K. S. Berggren, K. S. Johnson, M. Prentiss, D. C. Ralph, and G. M. Whitesides, *Nanostructure Fabrication in Silicon Using Cesium to Pattern a Self-Assembled Monolayer*. Appl. Phys. Lett. **71**, 1261 (1997).

[50] K. K. Berggren, A. Bard, J. L. Wilbur, J. D. Gillaspy, A. G. Helg, J. J. McClelland, S. L. Rolston, W. D. Phillips, M. Prentiss, and G. M. Whitesides, *Microlithography by Using Neutral Metastable Atoms and Self-Assembled Monolayers*. Science **269**, 1255 (1995).

[51] P. Engels, S. Salewski, H. Levsen, K. Sengstock, and W. Ertmer, *Atom Lithography with a Cold, Metastable Neon Beam*. Appl. Phys. B: Lasers Opt. **69**, 407 (1999).

[52] K. S. Johnson, K. K. Berggren, A. Black, C. T. Black, A. P. Chu, N. H. Dekker, D. C. Ralph, J. H. Thywissen, R. Younkin, M. Tinkham, M. Prentiss, and G. M. Whitesides, *Using Neutral Metastable Argon Atoms and Contamination Lithography to Form Nanostructures in Silicon, Silicon Dioxide, and Gold*. Appl. Phys. Lett. **69**, 2773 (1996).

[53] M. K. Oberthaler and T. Pfau, *One-, Two- and Three-Dimensional Nanostructures with Atom Lithography*. J. Phys.: Condens. Matter **15**, R233 (2003).

[54] F. Schreiber, *Structure and Growth of Self-Assembling Monolayers*. Prog. Surf. Sci. **65**, 151 (2000).

[55] C. O'Dwyer, G. Gay, B. Viaris de Lesegno, and J. Weiner, *The Nature of Alkanethiol Self-Assembled Monolayer Adsorption on Sputtered Gold Substrates*. Langmuir **20**, 8172 (2004).

[56] X. Ju, M. Kurahashi, T. Suzuki, and Y. Yamauchi, *Microlithography Using Metastable Helium Atoms: Patterning of Gold Film Coated with Dodecanethiol Self-Assembled Monolayers on Mica*. Jpn. J. Appl. Phys. **42**, 4767 (2003).

[57] A. Bard, K. K. Berggren, J. L. Wilbur, J. D. Gillaspy, S. L. Rolston, J. J. McClelland, W. D. Phillips, M. Prentiss, and G. M. Whitesides, *Self-Assembled Monolayers Exposed by Metastable Argon and Metastable Helium for Neutral Atom Lithography and Atomic Beam Imaging*. J. Vac. Sci. Technol. B **15**, 1805 (1997).

[58] V. Ganesh and V. Lakshminarayanan, *Self-Assembled Monolayers of Alkanethiols on Gold Prepared in a Hexagonal Lyotropic Liquid Crystalline Phase of Triton X-100/Water System*. Langmuir **22**, 1561 (2006).

[59] Y. Yamauchi, T. Suzuki, M. Kurahashi, and X. Ju, *Metastable-Atom-Induced Dissociation of Dodecanethiolate Self-Assembled Monolayers on Gold Substrates*. J. Phys. Chem. B **107**, 4107 (2003).

[60] Y. Xia, X.-M. Zhao, E. Kim, and G. M. Whitesides, *A Selective Etching Solution for Use with Patterned Self-Assembled Monolayers of Alkanethiolates on Gold*. Chem. Mater. **7**, 2332 (1995).

[61] J. J. McClelland, *Atom-Optical Properties of a Standing-Wave Light Field*. J. Opt. Soc. Am. B **12**, 1761 (1995).

[62] S. J. H. Petra, K. A. H. van Leeuwen, L. Feenstra, W. Hogervorst, and W. Vassen, *Numerical Simulations on the Motion of Atoms Travelling through a Standing-Wave Light Field*. Eur. Phys. J. D **27**, 83 (2003).

[63] S. J. H. Petra, *Nanolithography with Metastable Helium Atoms*. Ph.D. thesis, Vrije Universiteit Amsterdam, 2004.

[64] J. P. Gordon and A. Ashkin, *Motion of Atoms in a Radiation Trap*. Phys. Rev. A **21**, 1606 (1980).

[65] M. J. Partlow, *Bichromatic Collimation to Make an Intense Helium Beam*. Ph.D. thesis, Stony Brook University, 2004.

[66] S. Bergamini, B. i. t. Darquié, M. Jones, L. Jacubowiez, A. Browaeys, and P. Grangier, *Holographic Generation of Microtrap Arrays for Single Atoms by Use of a Programmable Phase Modulator*. J. Opt. Soc. Am. B **21**, 1889 (2004).

[67] D. P. Rhodes, D. M. Gherardi, J. Livesey, D. McGloin, H. Melville, T. Freegarde, and K. Dholakia, *Atom Guiding along High Order Laguerre-*

Gaussian Light Beams Formed by Spatial Light Modulation. J. Mod. Opt. **53**, 547 (2006).